To the Graduate Council:

I am submitting herewith a dissertation written by Yang Ren Sun entitled "*Flux Creep Studies in $YBa_2Cu_3O_{7-\delta}$ Superconductors.*" I have examined the final copy of this dissertation for form and content and recommend that it be accepted in partial fulfillment of the requirements for the degree of Doctor of Philosophy, with a major in Physics.

James R. Thompson

James R. Thompson, Major Professor

We have read this dissertation

and recommend its acceptance:

D. K. Christen

Gerald D. Mahan

Edwards

Marianne Breinig

Accepted for the Council:

Lawrence

Associate Vice Chancellor

and Dean of The Graduate School

FLUX CREEP STUDIES IN $Y_1Ba_2Cu_3O_{7-\delta}$ SUPERCONDUCTORS

A Dissertation

Presented for the

Doctor of Philosophy

Degree

The University of Tennessee, Knoxville

YANG REN SUN

May 1992

To

my parents, the source of my life

ACKNOWLEDGEMENTS

I greatly thank my thesis adviser, Professor Dr. James R. Thompson. For four years, he has been teaching me the art and science of performing research, helping me become familiar with apparatus, telling experiences of solving problems in various conditions that he gained through his research, and making corrections to my scientific papers in English with exceptional patience. He is the person from whom I learned how generous and helpful are the American people.

I appreciate very much the constant help and advice from Dr. D. K. Christen and colleagues in his research group: H. R. Kerchner, J. O. Thompson for their useful discussions and comments; J. G. Ossandon for teaching me to use the VSM; and Y. J. Chen for his assistance. I have been really happy working in such a creative and collaborative environment. I also thank F. Holtzberg and A. Goyal for providing the samples; L. Civale and A. D. Marwick for the light and heavy ion irradiations of samples.

My appreciation also goes to Professor Dr. Gerald Mahan. It was under his encouragement that I applied for doctorate studies in Physics in the University of Tennessee, Knoxville.

ABSTRACT

Magnetic relaxation studies were performed on a proton irradiated high J_c $YBa_2Cu_3O_{7-\delta}$ single crystal and a melt-texture-growth $YBa_2Cu_3O_{7-\delta}$ sample. Significant deviation from the logarithmic time decay predicted by conventional Anderson-Kim theory was observed for a wide range of temperature and magnetic field. The flux creep data, with durations up to 3.5×10^5 s, could be analyzed using several recent models with comparable accuracies. The difficulty in distinguishing between these models is due to the fact that the time window of observations, which usually covers ~2 or 3 decades, is too short for magnetic relaxation studies.

To complement these studies in the direct time domain, the effects of field-sweep rate $K = \partial H/\partial t$ on magnetization hysteresis loops M(H) and on flux-creep M(t) were investigated both theoretically and experimentally. We find the basic relation between M and K is, to first order, the following: $M = \text{const} - [dM/d\ln(t)]\ln(K) - [Kt_{eff}/10]$, where $dM/d\ln(t) = ac/30$ is the flux-creep rate in a cylindrical sample of radius a, and t_{eff} is an effective attempt time for vortex hopping. The largest possible M, which corresponds to the critical current density J_{c0} in the absence of thermal activation, develops when at high sweep rate $K \geq K_{max} = ac/[(1+a\alpha)t_{eff}]$ with $\alpha = \partial J/\partial H$. Such studies provided a way to measure t_{eff}, whose magnitude has been rather controversial; furthermore, the analysis revealed the time origin of flux creep, $t^* = ac/K(1 + a\alpha)$,

which is essential in studying the initial stages of relaxation. The theory agrees well with experiments yielding $t_{eff} \sim 0.2$ s for the melt-textured-growth sample.

By combining conventional flux creep experiments with measurements of magnetization versus magnetic field sweep rate, we are able to detect the decay of magnetization in both its middle and very early stages, thereby expanding the observational time window up to 5 ~ 6 decades. Among four models tested, only the Vortex-Glass/Collective-Pinning theory gives a consistent description of both stages.

TABLE OF CONTENTS

LIST OF FIGURES

Chapter I

INTRODUCTION

In 1986, J. G. Bednorz and K. A. Muller[1] first synthesized $(La\text{-}Ba)_2CuO_4$ and demonstrated it to be superconducting with a transition temperature T_c above 30 K. The news, like a big explosion, quickly spread throughout the world. The discovery stimulated many scientists to search for materials with even higher transition temperatures. Shortly after, a series of cupric-oxide materials, including $Y_1Ba_2Cu_3O_{7-\delta}$,[2] $Bi_2Ca_2Sr_1Cu_2O_8$[3] and $Tl_2Ca_2Ba_2Cu_3O_{10}$[4] were discovered, all with transition temperatures above 77 K. The dream to have superconductors that work at the temperature of liquid nitrogen, an inexpensive and simple refrigerant, seemed to come true.

Soon, however, further studies revealed a special magnetic property of these cupric-oxide materials: giant flux creep in the mixed state[5,6,7,8,9], a state that develops in the presence of magnetic fields above a modest level. This brought a serious question: do these innovative materials have real potential for technological applications?

To explain what flux creep is and why it is so important to the superconducting materials, we introduce here some basic magnetic properties of superconductors. All

superconductors can be divided into two categories, called type I and type II, according to their response to magnetic fields. Consider first type I superconductors, in which there is a single critical magnetic field $H_c(T)$. For fields below H_c, there is a superconducting phase in which no flux penetrates into the material except very near the surface. This is the Meissner phase with flux density $B=0$. Above H_c, the superconducting properties are destroyed and the material becomes normal. The field H_c is also denoted as the thermodynamic critical field, because at H_c the magnetic energy per volume $H_c^2/8\pi$ is equal to the condensation energy per unit volume of the superconductor. The condensation energy is the difference in free energy of the material between its normal (non-superconducting) state and superconducting state. At T_c, the two are equal and so $H_c \to 0$ as $T \to T_c$. For type II superconductors, there are two additional critical fields: the lower critical field H_{c1} and the upper critical field H_{c2}. The Meissner phase only exists below H_{c1}. When the field is greater than H_{c1}, quantized flux lines start to penetrate into the material, but there are still superconducting electron pairs and microscopically distributed superconducting regions. Hence, this state is usually referred to as the "mixed state". The superconducting pairs do not disappear until the field reaches the value of H_{c2}. All known high temperature superconductors (HTSC) are type II materials with lower critical field H_{c1} the order of $\sim 10^2$ Gauss = 0.01 Tesla and upper critical field H_{c2} the order of $\sim 10^6$ G $= 10^2$ T (at zero temperature). Compared with their low temperature counterparts that have $H_{c2} \approx$ 1-10 T, the HTSC materials have a mixed state region that occupies a much larger area in the

H-T phase diagram. Figure 1 shows a schematic phase diagram for a high temperature superconductor.

In the mixed state, magnetic flux penetrate into the material in the form of quantized lines called vortices. The vorticity refers to the circulation of supercurrents around the axis of the flux line. A vortex looks like a filament with a core of small diameter $\sim\xi$, where ξ is the coherence length between a pair of electrons. Within the core, the density of superconducting electrons n_s decreases, as shown in Figure 2, and becomes zero at the center. The local magnetic field is not confined to the core; while it is a maximum at the center of the filament, it extends radially outward a distance λ called the London penetration length. Annular currents with density J encircle the filament and screen out the field for $r \geq \lambda$. A single filament can take on only discrete values of flux $\Phi=n\Phi_0$, where Φ_0 is the flux quantum $\Phi_0=ch/2e=2.07\text{x}10^{-7}$ G cm^2. In order to minimize the energy, each vortex carries one quantum of flux, i.e., $n=1$. If the material is ideally homogenous, vortices form a triangular lattice (an Abrikosov Lattice) so as to minimize the repulsive vortex-vortex interaction energy. Both H_{c1} and H_{c2} relate to the penetration depth λ and the coherence length ξ, the two most important length scale in superconductors, with $H_{c1} = [\Phi_0/(4\pi\lambda^2)]\ln(\lambda/\xi)$ and $H_{c2} = \Phi_0/(2\pi\xi^2)$. The physical meaning is that at H_{c1}, the vortex lattice constant $(\Phi_0/B)^{1/2} \approx \lambda$; thus each vortex is almost isolated. On the other hand, the vortex cores at H_{c2} almost touch each other: hence there is no superconducting region anywhere.

Figure 1

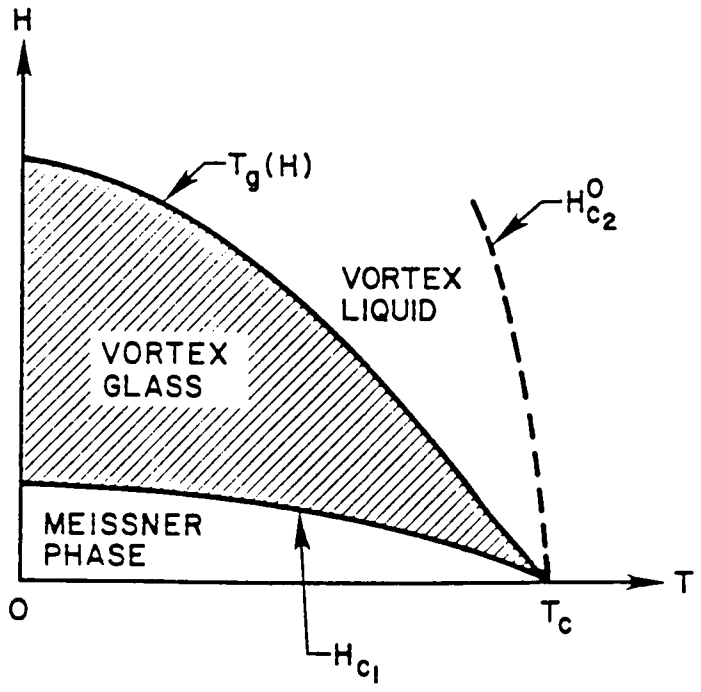

Schematic phase diagram for a bulk high temperature superconductor such as $Y_1Ba_2Cu_3O_7$.

Figure 2

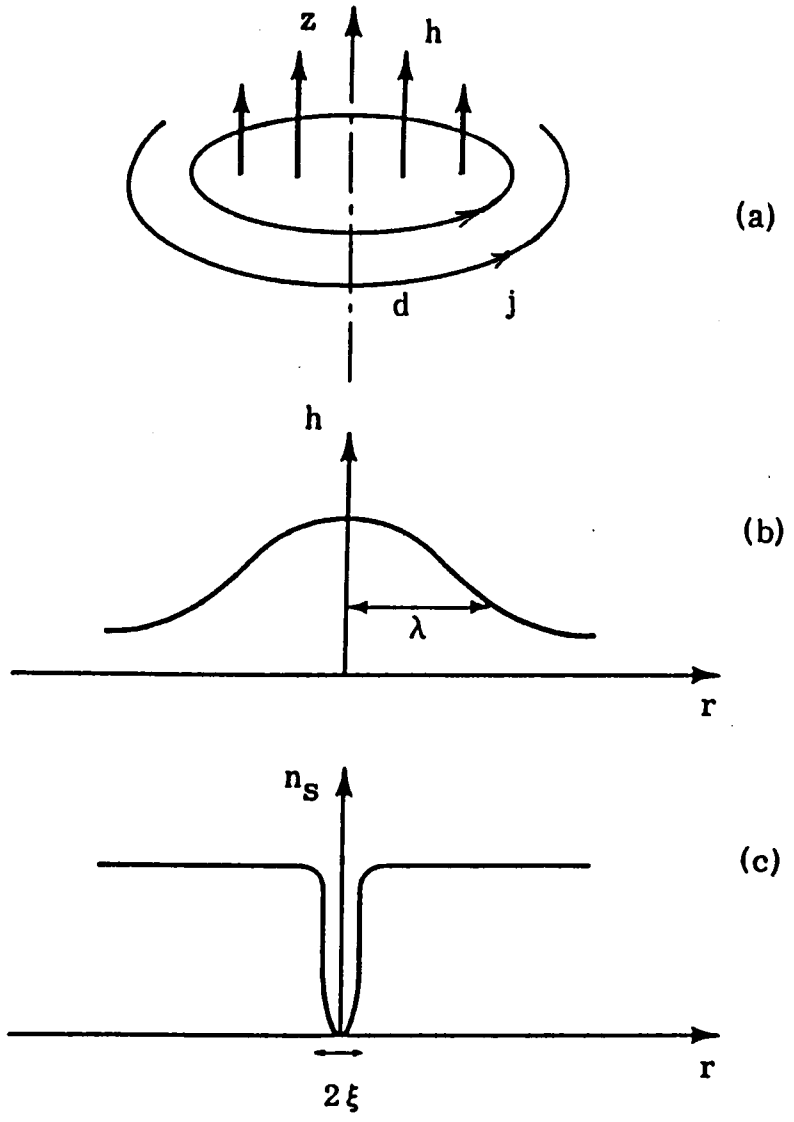

Structure of one vortex line in a type II superconductor, (a) Annular currents encircle the core. (b) The magnetic field is maximum near the center and decreases with distance r due to screening. (c) The density of superconducting electrons is reduced in the core region.

Let us now consider a superconductor in the mixed state, which carries some external or induced current. In this case, the vortices are subjected to a stress due to the Lorentz driving force $\sim \boldsymbol{J} \times \boldsymbol{B}$. If there are no pinning forces on the vortices to balance the Lorentz force, the vortices will move. This dissipates energy, since the core of the vortex is nonsuperconducting. Fortunately, there are almost always some defects or disordered regions in real materials that can pin the vortices. Though the precise nature of the interaction between various defects and vortices is still not clear, the qualitative effect is that a vortex can reduce the loss of condensation energy of the normal (non-superconducting) core by sitting on a defect that is nonsuperconducting anyway. Stronger pinning means that the material can transport higher current density. A material parameter, the critical current density J_c, generally symbolizes the maximum current density. When the Lorentz driving force density reaches the value of J_cB, the maximum pinning force and the Lorentz force balance; the net barrier to vortex motion disappears, and vortices begin to flow. For a smaller driving force, vortices can jump from one barrier to another via thermal activation. A voltage drop measured along the current direction is proportional to Bv with v being the speed of flux motion. This means that the resistance of the material is no longer zero. Experimentally we can detect this finite dissipation by observing the decay of the induced shielding currents, which is proportional to the magnetic moment of the sample. This decay of magnetic moment is called magnetic relaxation. In low temperature superconductors, the relaxation is usually very small; for instance, the magnetization may decay by a few percent in ten years. In

contrast, the magnetization in HTSC may decay by a few tens of percent in only a few seconds. This means that the supercurrent in the mixed state is only quasi-persistent. It appears that dissipation could be always present, rendering the materials virtually useless for many, if not most, technical applications.

Tremendous work has been done to understand this peculiar phenomenon. Soon, it was concluded that this giant flux creep is due to the high operating temperature combined with the low effective pinning (or activation) energy in HTSC's. According to the following discussion of the classical Anderson-Kim (A-K) theory,[10,11] the magnitude of the pinning energy (the depth of the potential well) is proportional to the condensation energy in a correlation volume, $(H_c^2/8\pi)(\pi\xi_{ab}^2 L)$, where ξ_{ab} is the coherence length along the a-b (Cu-O_2) plane, L is the correlation length along the c direction (see Figure 3 for the layered structure of the $Y_1Ba_2Cu_3O_7$ superconductor), and H_c is the critical field. Now, ξ is much shorter (a few Å) in HTSC's than in the low temperature counterparts (a few hundreds of Å); consequently, it seems that a small pinning energy and giant magnetic relaxation must be an intrinsic feature of HTSC. On the other hand, it was found[12,13] that in a subcritical state with $J \ll J_c$, the creep rate (movement) of vortices and vortex bundles is greatly reduced. Meanwhile, both Vortex-Glass (VG) and Collective Pinning (CP) theory[14,15] asserted that there is a transition in the mixed state from a vortex liquid phase with negligible pinning into a vortex glass phase, which is driven by random pinning forces from impurities (Figure 1). In the glass phase, the correlation length L (and thus the volume) of a vortex bundle increases with

Figure 3

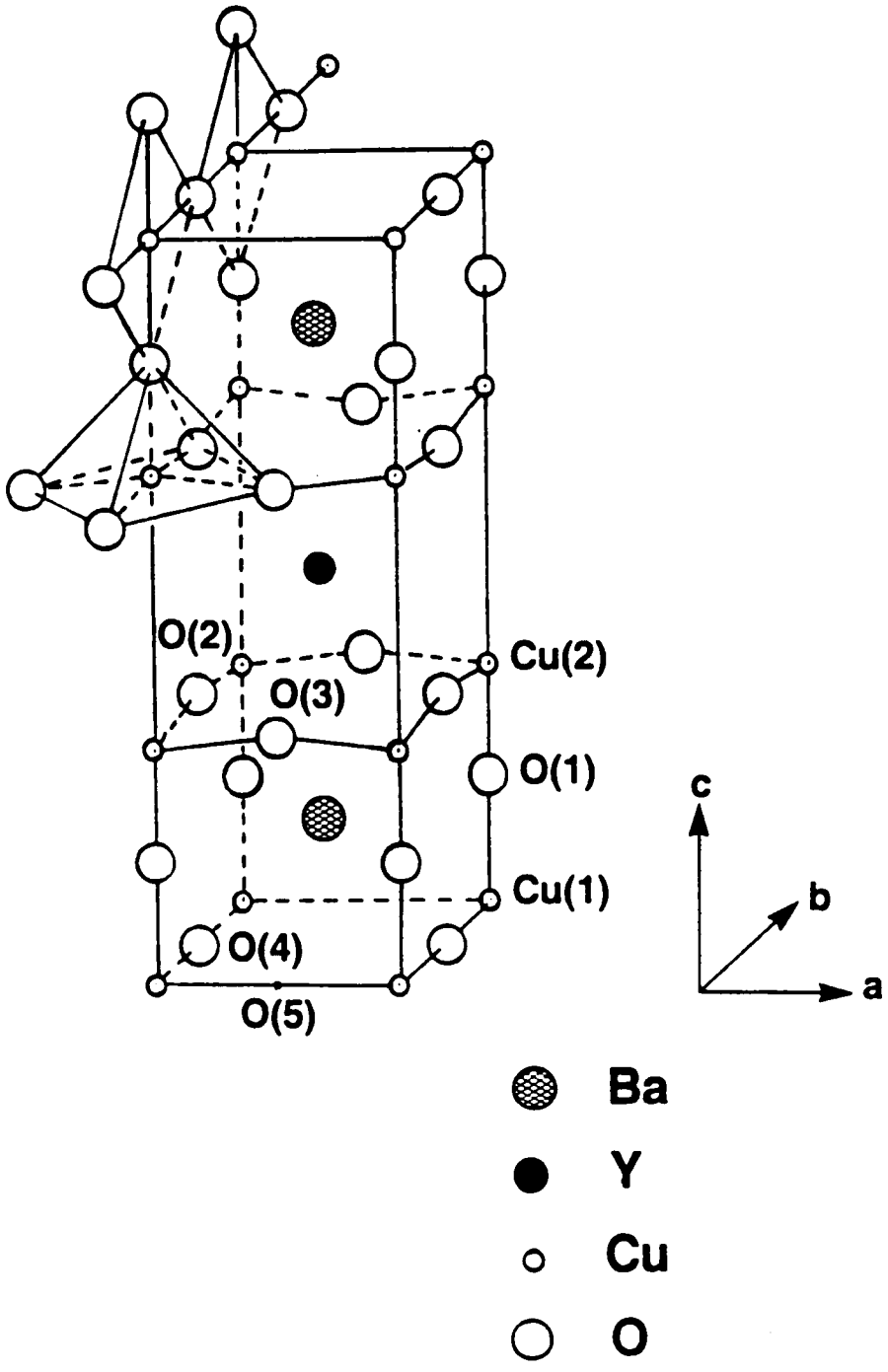

Structure of a $Y_1Ba_2Cu_3O_7$ unit cell.

decreasing current density j as $L \propto j^{-1/\theta}$; also the pinning energy $U \propto L^{\psi}$ of a bundle increases with L, where θ and ψ are two positive scaling exponents. By combining these two relations, one has that $U(j) \propto j^{-\mu}$ with $\mu = \psi/\theta$. Therefore, the fundamental feature of the glass phase is the existence of barriers that diverge for at vanishing driving force: this feature quenches of the motion of the vortices. In other words, the linear resistivity becomes zero in the glass state as $J \to 0$, giving a "true" superconductor.

In addition to VG/CP theory, there are some other competing models[16,17,18,19] of flux creep in HTSC's, which in particular contain different dependencies of the activation energy on current density J.[20] So far, experimental evidence has not clearly favored any particular model. The difficulty is this: the magnetic relaxation, to first order, is a logarithmic function of time with $M(t) \propto J(t) \sim \ln(t)$. On the other hand, the experimental observation window is usually about 2 decades of time, which is too short to distinguish between the fine differences of various models. In transport measurements, the situation is similar, since with $J \ll J_c$, the resistance is so small that an ultra-high resolution voltmeter is required to measure the current-voltage characteristics.

As giant flux creep directly affects the possibility of achieving high critical currents, which are essential for widespread applications, a complete experimental study of this issue is much desired and important. We have investigated this unique phenomenon of giant magnetic relaxation in HTSC and find strong support for VG/CP

theory. Noting that the production of columnar defects by heavy-ion irradiation[21] greatly increased the critical current density (with H = 1 Tesla, J_c reached 1.2×10^7 A/cm^2 at 5 K and 4×10^5 A/cm^2 at 77 K, respectively) and expanded the glass phase region in the H-T phase diagram, we believe that producing strong pinning and developing high J_c in HTSC materials is possible.

The experiments were performed mainly on two samples of $Y_1Ba_2Cu_3O_{7-\delta}$, one of the most important materials in the family of HTSC's. Figure 3 shows its structure. It is a layered structure with O(2), O(3) and Cu(2) ions forming two planes (the a-b planes) separated by Y atoms. The c-axis is perpendicular to the a-b plane. It is found that the superconducting electron pairs lie mainly in the Cu-O planes; therefore the critical current density J_c in the a-b plane is larger than along the c direction, which makes the material anisotropic. The other families of HTSC's, such as $Bi_2Ca_2Sr_1Cu_2O_8$ and $Tl_2Ca_2Ba_2Cu_3O_{10}$, are also layered materials with much stronger anisotropy. Hence their J_c along the c-axis is very small. The other interesting phenomenon is that, if currents flow in the a-b plane (e.g., along the b-axis) with magnetic fields applied perpendicularly, the J_c is much larger for fields along the a-axis than along the c-axis. This clearly shows that the a-b planes can pin vortices intrinsically. In all our experiments, fields are applied parallel to the c-axis with induced currents flowing in the a-b planes.

One of the samples is a proton-irradiated single crystal. The irradiation induced defects increased J_c by ~ 10 at 5 K and $\sim 10^2$ at 77 K, relative to the same crystal prior to irradiation. The second is a melt-textured-growth sample. The experimental results, composed of four parts, are contained in chapter IV. First, we report on the observation of a non-logarithmic time decay in the magnetic relaxation. In measurements of flux creep lasting up to 3.5×10^5 s (~ 4 days), we found that the data cannot be explained using conventional Anderson-Kim[10,11] theory. However, the results can be analyzed using several recent models, including Vortex-Glass[14] and Collective-Pinning theory,[15] a power law model,[16] a model by Griessen[19], and a double logarithmic expression,[22] all with similar quality. In the second part, the effects of field sweep rate on magnetization hysteresis loops and on flux-creep studies are discussed, both theoretically and experimentally. The analysis, which agrees well with experiments, can be used to investigate the early stages of flux creep and to determine the time origin in the flux creep measurements. In the third part, we combine conventional flux creep experiments with an analysis of magnetization versus field sweep rate to detect the time decay of magnetization in both its intermediate and early stages; this expands the observation window up to $5 \sim 6$ decades of effective time. Among the four models tested, only VG/CP theory consistently describes both stages. In the final part, the separate temperature and field dependencies of the activation energy U(T, H, J) are examined experimentally. For fixed current density J, peaks in U were observed with respect to both temperature and magnetic field. The magnitude of U agrees well with values reported from resistivity studies on high-J_c epitaxial films.

To provide a good understanding of the results, Chapter II gives a brief description of the main experimental aspects, including sample preparation, the structure of the SQUID magnetometer, and techniques used in the measurements. Chapter III gives the theoretical background required for an analysis of experimental data. Finally, a short summary is presented in Chapter V.

Chapter II

EXPERIMENTAL ASPECTS

II.1 Sample Preparation

Two $Y_1Ba_2Cu_3O_{7-\delta}$ samples were primarily used in flux creep experiments. One was a proton irradiated high J_c single crystal with mass of 98-μg obtained from F. Holtzberg of the IBM Thomas J. Watson Research Center. The other was a melt-textured-growth sample with mass of 0.0747g from A. Goyal of the Metal and Ceramics Division, Oak Ridge National Laboratory. In the rest of this work, they are designated sample 1 and sample 2, respectively.

For growth of the IBM crystal[23], pellets of correct compositions were produced from CuO (Johnson-Matthey) and presynthesized 123 ($Y_1Ba_2Cu_3O_7$) and $BaCuO_2$. A pellet of 2 ~ 5 g was placed in a Au crucible supported on a Au sheet. The charge was heated to 970°C at 200°C/h in air, held at that temperature for 1.5 h and then cooled to 400°C at 5-50°C/h. In this condition, the liquid is mobile and clean crystals of 123 were found in the cavity between the support sheet and the crucible bottom. Crystals having clean, reflective surfaces were selected for annealing to maximize the oxygen content. The samples were put in flowing oxygen gas (1 atm) in Au sample cups. The

temperature was cycled to 600°C at 200°C/h and held at that temperature for 0.5 h to remove adsorbed gaseous species from the surface. The crystals were cooled to 420°C at 200°C/h, held there for 30 h to 10 days, and then cooled rapidly to room temperature.

The composition of the 123 crystals was determined by electron microprobe analysis. The Y:Ba:Cu atomic ratios were found to be 1:2:3 in each crystal within the accuracy of the measurement. The crystals were rectangular prisms and crystallographically twinned. The sample selected for our experiments has dimension of 1.15x0.226x0.045 mm^3, with the shortest dimension perpendicular to the highly conductive Cu-O sheets of the layered structure. The superconductive transition temperature T_c was 92.5 K initially, with transition width $\delta T_c < 0.5$ K. The T_c was measured in a commercial superconducting quantum interference device (SQUID) magnetometer from Quantum Design, Inc., with a small field (10 G) applied parallel to the c-axis. To create defects for pinning vortices, the sample was irradiated with 3-MeV protons to a fluence of $2x10^{16}$ ions/cm^2. After irradiation, the T_c measured similarly was 91 K. Figure 4 show the susceptibility $-4\pi\chi = -4\pi M/H$ versus temperature in zero field cooled (ZFC) and field cooled (FC) measurements before and after the irradiation, respectively.

In preparing the melt-textured 123 samples,[24] polycrystalline 123 was first prepared by using a conventional solid-state technique. Sintered polycrystalline 123 compacts were ground to -400 mesh size ($< 37\ \mu m$) for forming the composites. The

Figure 4

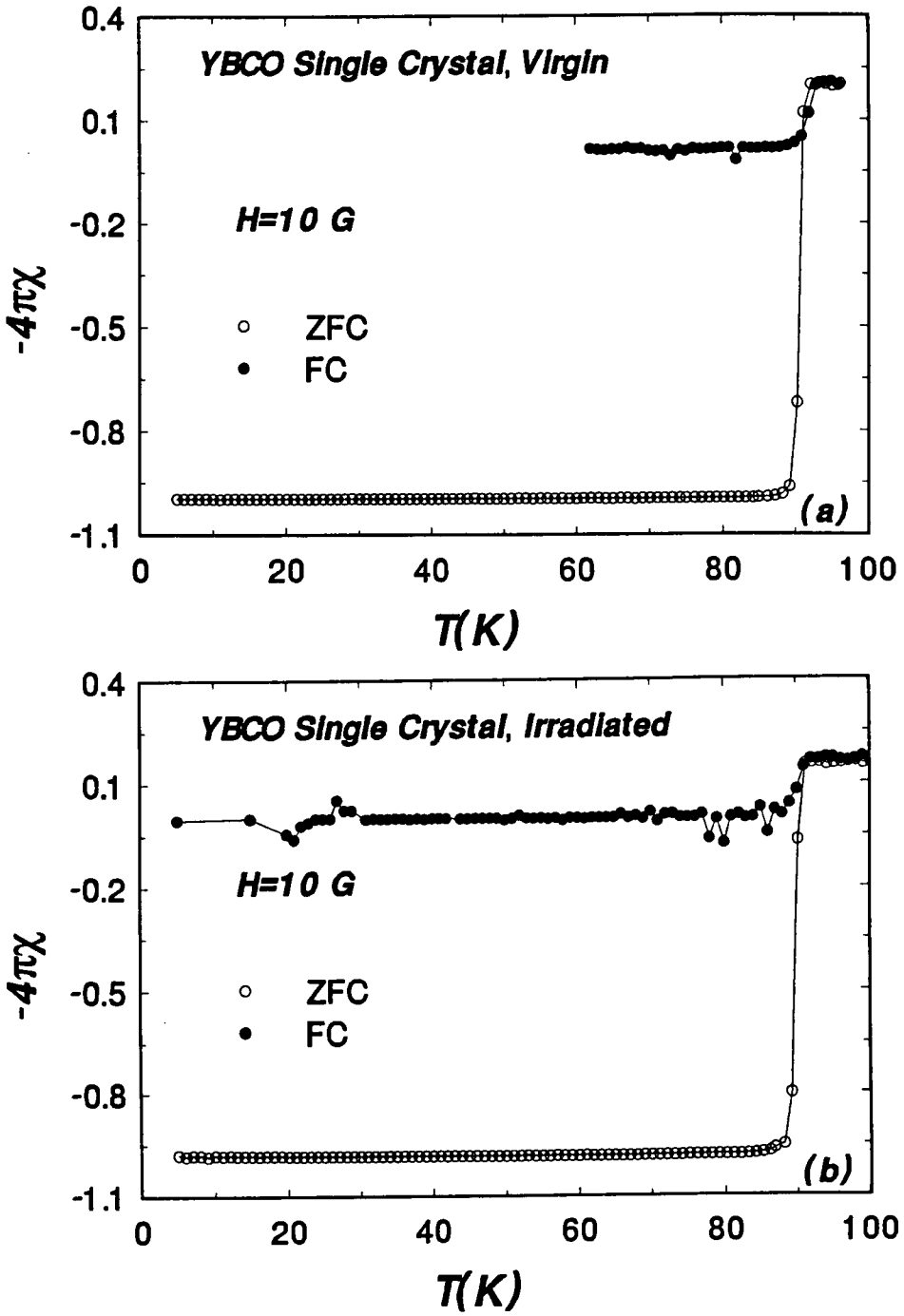

Susceptibility versus temperature of the YBCO single crystal: (a) before the irradiation; (b) after the irradiation.

powder was compacted into either 13 mm or 31 mm cylindrical discs, sintered for five hours at 900°C in air, and furnace cooled. These compacts were then melt-processed following a procedure outlined schematically in Figure 5. No externally applied thermal gradient was imposed on the sample during the entire cycle.

Figure 6 shows the microstructure of a single domain in a melt-textured sample. The domains in this sample were 5-6 mm long and 4-5 mm wide. Each domain is comprised of a stack of highly aligned platelets. The platelet widths lie in the range of 10-20 μm. These materials can be easily cleaved along any of the parallel boundaries seen in Figure 6. The X-ray diffraction pattern from a cleavage surface along one of theses boundaries is shown in Figure 7. The predominant c-axis orientation is apparent, indicating that the parallel boundaries seen in the optical micrograph of Figure 6 are nearly perfect traces of the (001) basal plane. The results from TEM (transmission electron microscopy) and CBED (convergent beam electron diffraction) have shown that there is virtually no orientation change between adjacent platelets within a given domain in well formed samples.[25,26] Examination of many well separated platelets indicates that the platelets comprising a given domain are portion of a common single crystal. The sample selected for our studies has mass of 0.00747 g. The approximate dimensions were 0.21x0.30x0.20 cm^3. The T_c, measured in a similar way as for the crystal sample 1, was 90 K.

Figure 5

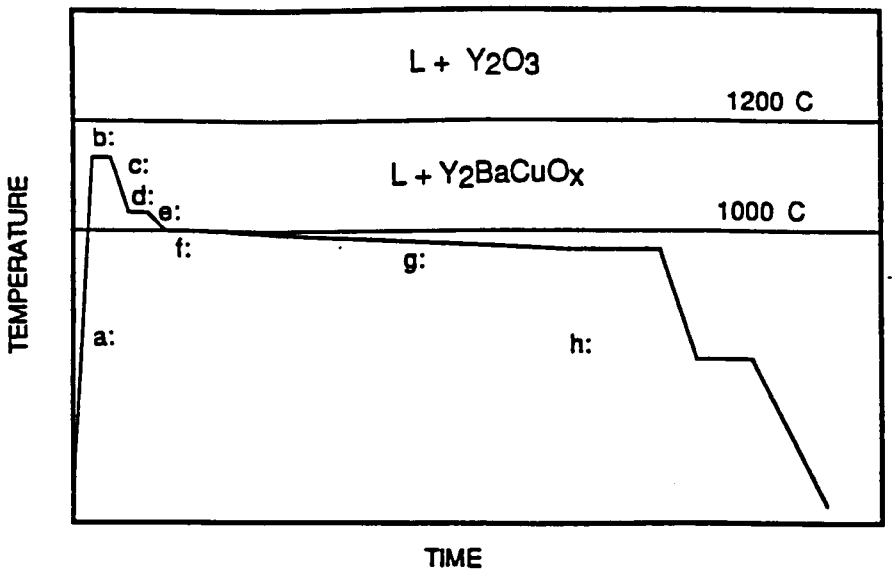

a: heat at 1000 ° C/hr to 1030-60 ° C.
b: hold for 15-20 mins.
c: cool at 1000 ° C/hr to 1005 ° C.
d: hold at 1005 ° C for 15-20 mins.
e: cool at 1-2 ° C/hr to 1000 ° C.
f: hold at 1000 ° C for 1 hr.
g: cool at 1-2 ° C/hr to 950 ° C.
h: Oxygenation cycle.

Schematic of a typical heat treatment schedule used to form the aligned materials such as sample 2 (*A. Goyal et al*, Physica C **182**, 203 (1990)).

Figure 6

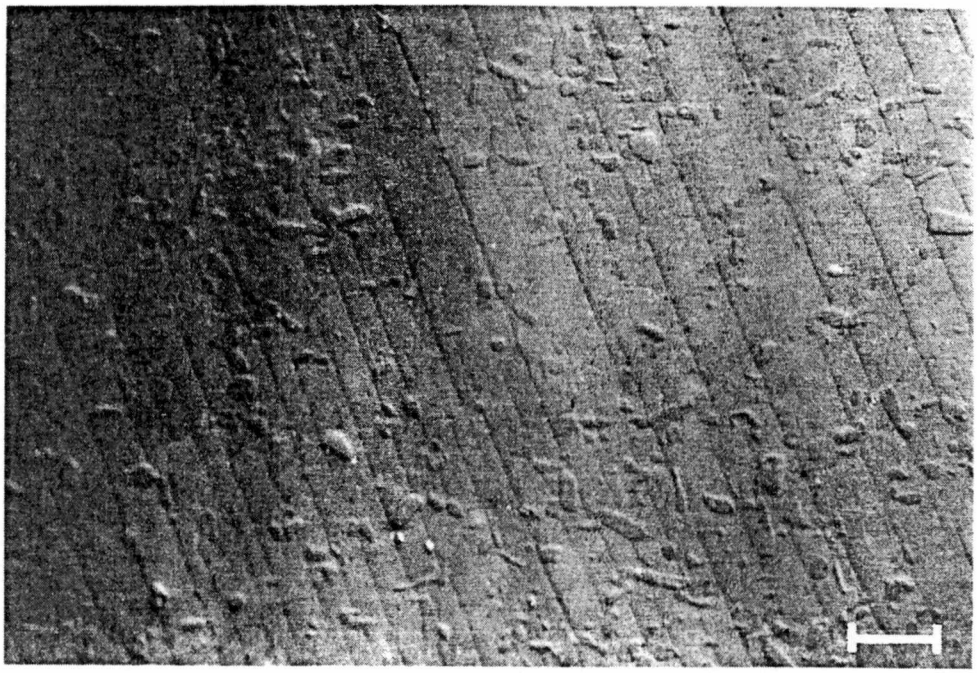

Normaski light micrograph of an aligned $YBa_2Cu_3O_{7-\delta}$ melt-textured sample, showing the orientation. The bar represents 25 μm (from the same source as for Figure 5).

Figure 7

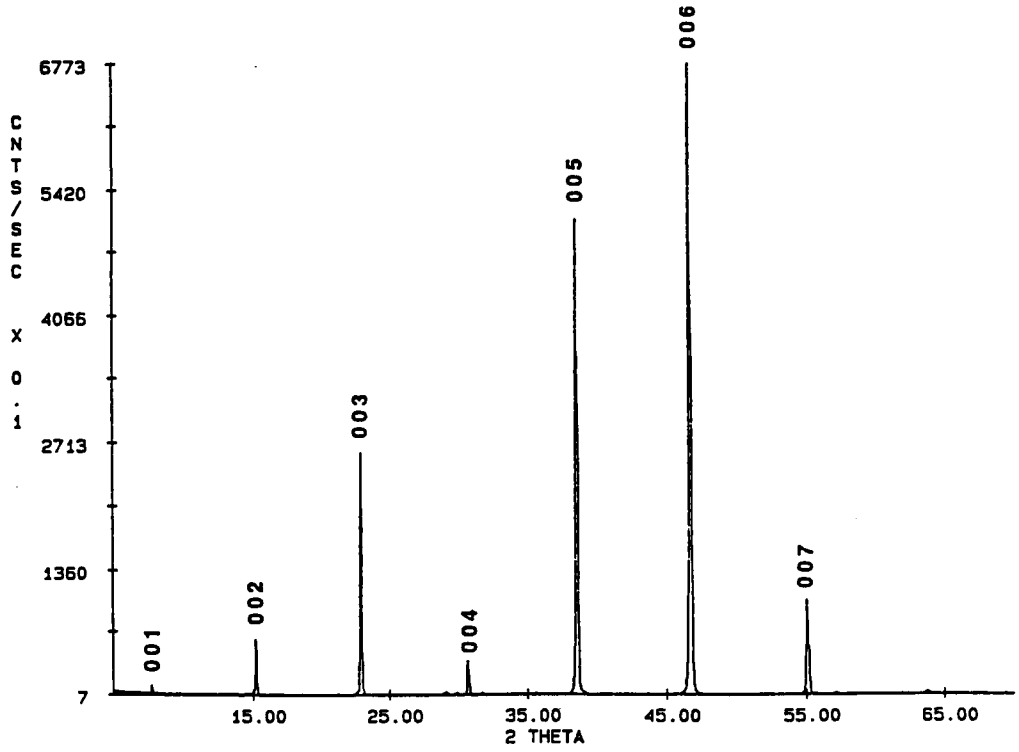

X-ray diffraction pattern of the cleavage surface for the melt-textured sample, showing the nearly perfect c-axis orientation (from the same source as for Figure 5).

II.2 Apparatus for Characterization of the Samples

The magnetic characterization of samples was performed primarily in (1) a commercial SQUID magnetometer (Quantum Design Inc.) and (2) a laboratory constructed Vibrating Sample Magnetometer (VSM). Both instruments are able to measure the magnetic moment of a small sample in various conditions but with differing resolution and other capabilities. A brief introduction to the structure of the SQUID magnetometer is presented in this section. The technical characteristics of both instruments are described in detail elsewhere.[27,28]

The Magnetic Properties Measurement System (MPMS) is a SQUID based-magnetometer fabricated by Quantum Design Inc. A short explanation of the working principle of a SQUID detector, the key part of the instrument, can be found in Appendix A. This sophisticated instrument is designed for studying magnetic properties in fields ranging from -5.4 T to +5.4 T (or from -7 T to +7 T for the MPMSR2) over the temperature range from 1.8 K to 300 K with high stability (<0.01 K at 4.2 K and <0.05 K at 300 K, respectively). The apparatus has high differential sensitivity, $\sim 10^{-8}$ emu in a 2 T field, and a capability to measure magnetic moment up to ± 300 emu. The field is relatively uniform (10^{-4} over ± 3 cm from the center of the pick-up coils). When changing field, it approaches the target field monotonically with no overshooting, which is extremely important for magnetically hysteretic materials, such as high T_c

superconductors. These features make the SQUID magnetometer a powerful tool for studying the magnetic properties of small HTSC samples.

The hardware of the SQUID magnetometer includes a HP computer plus two major cabinets (Figure 8): the MPMS dewar and probe assembly and the control system in the control console. These two cabinets integrate four major physical components:

(1) The electronic control console, which includes the 1822 MPMS Controller, the 1802 R/G Bridge, the MPMS gas control system, the superconducting magnet power supply, the sample transport controller, and a vacuum pump; (2) the MPMS cryogenic probe, which contains the Temperature Control Module (TCM) and the SQUID detection system; (3) the sample transport mechanism mounted on the top of the TCM and sample rod assemblies; (4) and the liquid helium dewar.

When the hardware is configured for magnetic measurements, it integrates seven functional systems under the MPMS Control Software. (1) The HP computer with installed MPMS operating software allows one to communicate with two subsystem controllers, the 1822 MPMS Controller and the 1802 R/G Bridge, via an IEEE interface and GPIB bus. The computer also provides automatic data acquisition and programming for measurements. (2) The TCM supports an actively regulated precision thermal environment for the sample space. (3) The superconducting magnet system provides a reversible field operation from -5.5 T to +5.5 T. (4) The SQUID detector, incorporating Model 2000 SQUID amplifier control electronics, senses signals coupled

Figure 8

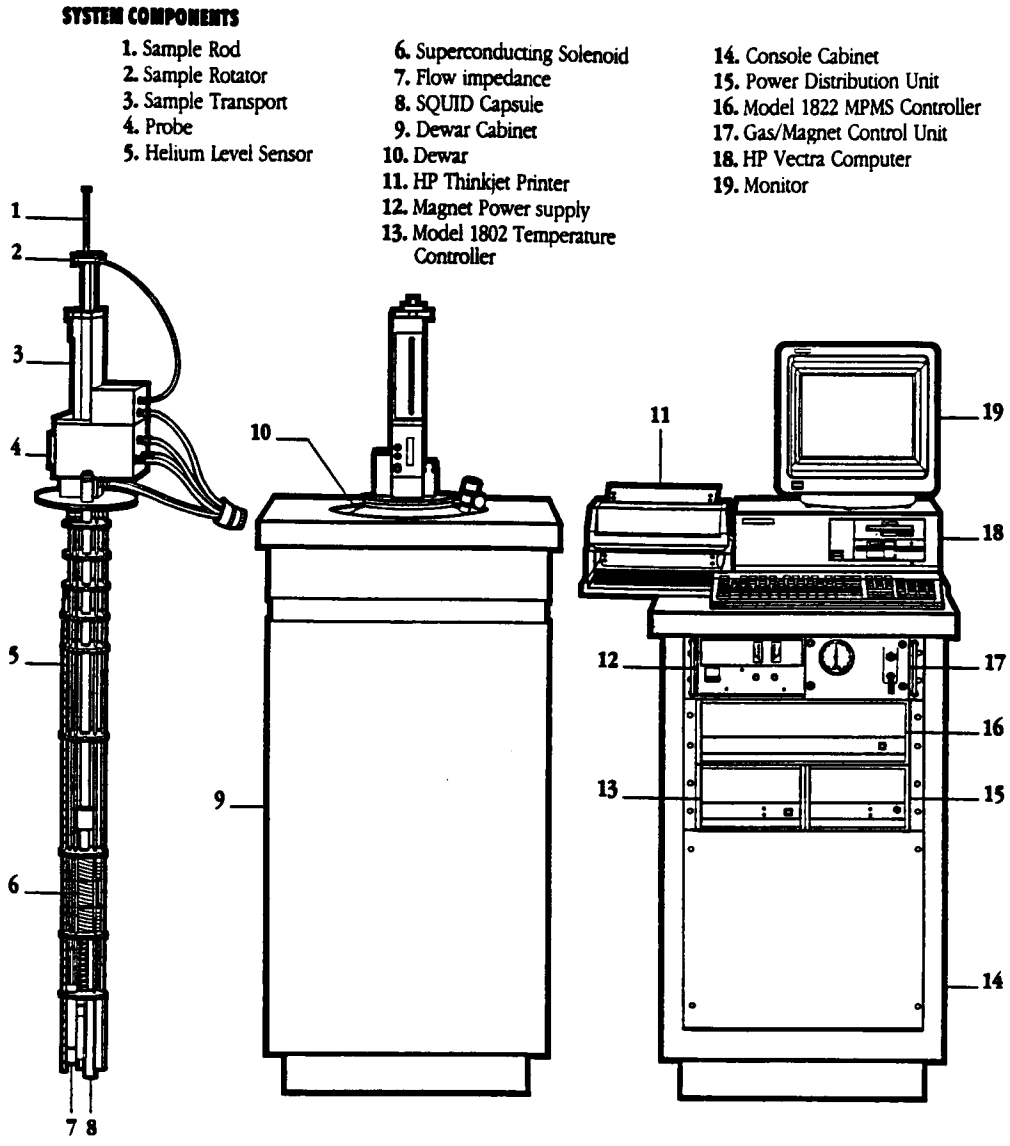

System components of the SQUID Magnetometer (QUANTUM DESIGN, Inc.).

from superconducting pick-up coil loops (see the discussions in the previous section). (5) The liquid helium system, with 56 liter capacity dewar and helium level meter probe, supports refrigeration for the superconducting magnet, SQUID detecting system and for operation down to 1.9 K. (6) The gas handling system controls the gas flow for temperature regulation, flushing and cleaning procedures. (7) The sample handling device, via a microstepping controller, performs automatic sample measurements and position calibration at resolution of $3x10^{-3}$ cm.

The overall schematic diagram of the SQUID magnetometer is shown in Figure 9. Here we discuss only the MPMS temperature control system, the magnetic field control system, and the SQUID detector, which are most relevant to understanding and explaining of the data. The details of the other systems can be found in reference.[27]

The MPMS Temperature Control System The sample chamber and the temperature control system is shown in Figure 10. The system uses two thermometers to cover the entire temperature range from 1.9 K to 400 K. A germanium resistance thermometer is used from 1.9 K to 40 K and a platinum resistance thermometer is used above 40 K. These two thermometers are installed at the bottom of the sample chamber and assigned to two thermometer inputs in the 1802 R/G Bridge, the central component in the temperature control system. There are two heaters controlled by the 1802 R/G Bridge. The gas heater, located at the bottom of the sample tube, is connected to the Driver #1 output of the 1802. The other one is a chamber heater, sharing output Driver

Figure 9

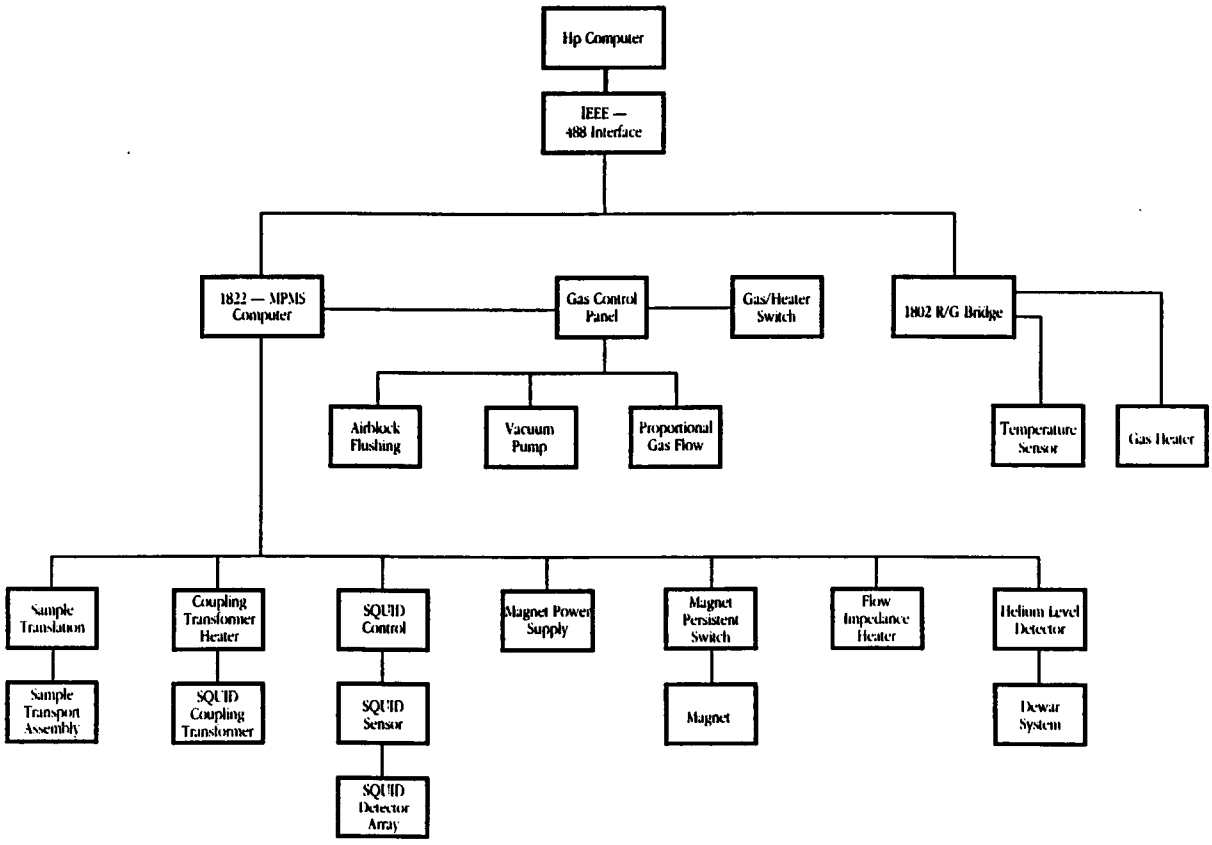

The MPMS functional control diagram.

Figure 10

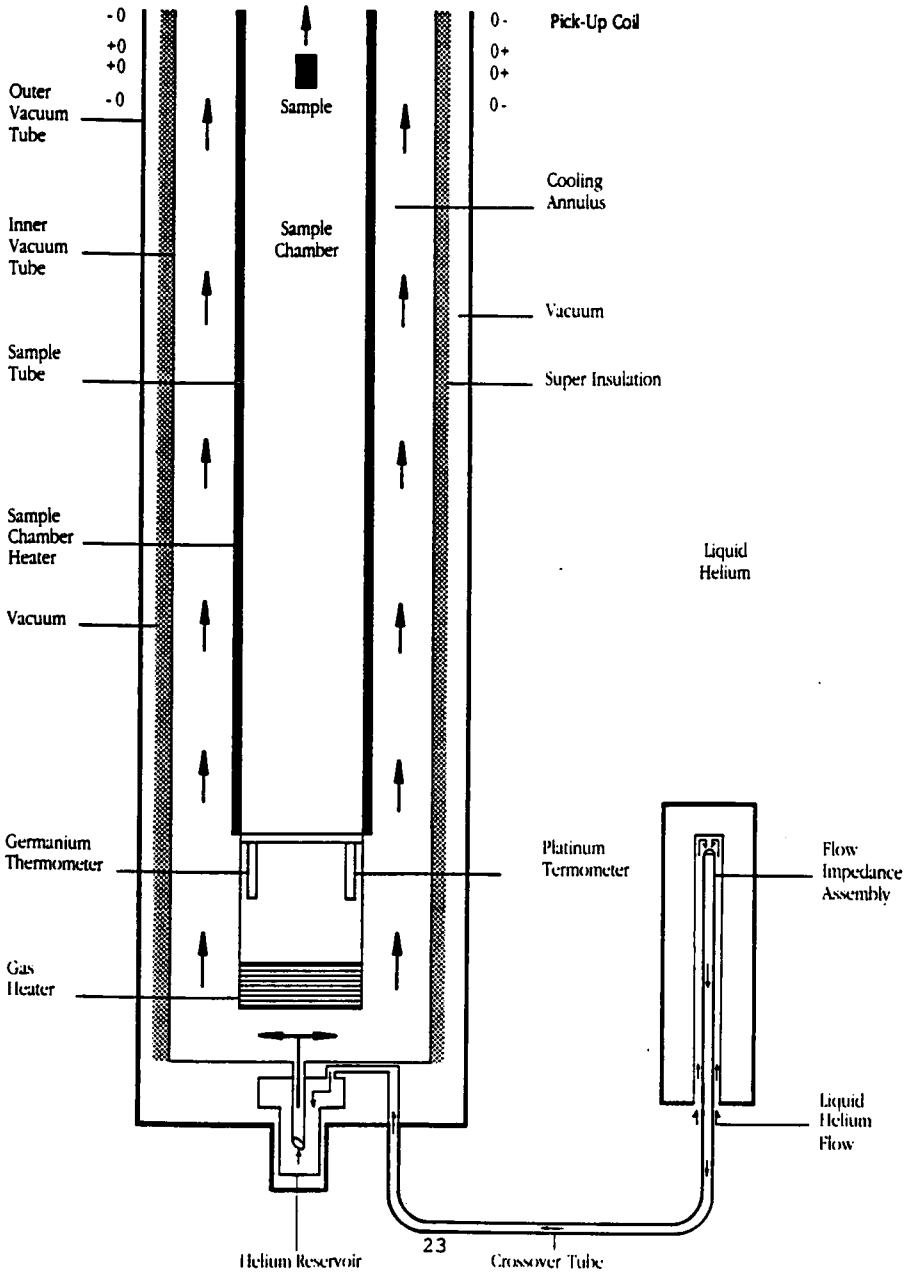

The MPMS temperature control module.

#2 with a proportional valve as a flow regulator; the Driver switches between them by the 1822 MPMS Controller.

The chamber can be heated by applying power to either the chamber heater surrounding the chamber, or to the gas heater located the bottom of the chamber. The cooling mechanism is provided by drawing cold gas into the annulus, the space around the sample chamber, from the helium bath. To maintain thermal uniformity, copper wires are placed along the chamber longitudinally. A few millimeters pressure of helium gas in the chamber provides thermal contact with the sample.

Two fundamentally different control mechanisms are used in the MPMS. The normal one works for all temperatures above 4.4 K, while the other provides lower temperatures. Consider first the former case ($T > 4.4$ K), and suppose that one desires some higher temperature. Normally the system uses a high-power mode via the chamber heater with heating rate about 10 K/minute (at room temperature). The heat is of high spatial uniformity to avoid thermal gradients in the system. When the temperature nears the target temperature, the system switches to a low-power control mode by turning on the gas heaters. This gas heater is also used to maintain thermal stability by warming the incoming helium gas to the same temperature as the sample chamber. Good control of temperature can be obtained by means of the small heat capacity and the low flow rate of helium gas. Cooling rates can be as high as $20 \sim 30$ K per minute at room

temperature, in which case cold helium gas is drawn into the annulus at rates exceeding five liters of helium gas STP per minute (STP: standard temperature and pressure).

However, there is a problem in this high speed cooling mode: a large thermal gradient is generated in the sample chamber as the bottom of the chamber cools much faster. The MPMS temperature control system has been designed to minimize this problem, but the technique helping to reduce the thermal gradients causes an undershoot of the target temperature. Temperature control during a warmup is much better and the overshoot is much smaller, therefore it is recommended that data be collected while the temperature is increasing. In case the undershoot causes some problem, one can choose an "Undercool Off" mode, in which the system uses a low power cooling mode and the temperature undershoot is minimized, typically to 1 K, but it takes much longer time.

Temperature Control Below 4.4 Kelvin There is a fundamental change in the operation of thermal control at temperatures below the boiling temperature of liquid helium, 4.4 K (this temperature is slightly above the normal temperature of 4.2 K, due to the slight overpressure on the He bath). To achieve temperatures below this point, liquid is filled into the lower part of the annulus. When the liquid level gets to the appropriate level, the liquid input is cut off and the temperature is controlled by setting the pressure over the liquid. The temperature regulation is then essentially performed by adjusting the pressure at the pump. During the measurements, the helium level in the annulus slowly falls due to evaporation of the liquid. One charge of liquid can last for

a period ranging from 45 minutes to a few hours, depending on the temperature being held and the heat load introduced to the system by the sample. When the liquid helium is exhausted, it is sensed by the control unit and the sequence of refilling the annulus with fresh liquid is initiated. The refill operation requires about 25 minutes.

In working below this crossover temperature, one should be aware that setting the sequence of temperatures in decreasing order will greatly increase the operating time of the reservoir between refills. The reason for this is that it requires a substantial fraction of the liquid in the reservoir to cool down from 4.4 K to 1.9 K. However, if the measurements start from the crossover temperature, a significant fraction of the initial helium charge will be used as the system successively lowers the temperature, hence the amount of liquid which must eventually be cooled to 1.9 K is much less.

MPMS Magnetic Field Control The magnet control system is shown in Figure 11. The field is provided and sustained by charging or trapping a certain amount of current in the superconducting magnet. The sequence of changing the field when one updates a new magnetic field through HP computer is as follows:

1. Turn on the power supply and a heater. The heat is used for warming the SQUID flux transformer that prevents large standing currents from being trapped in the SQUID sensing circuit as a result of the field change.

2. Set the current switching relays for the correct polarity and set the power output to match the current presently circulating in the magnet. It is important for the

Figure 11

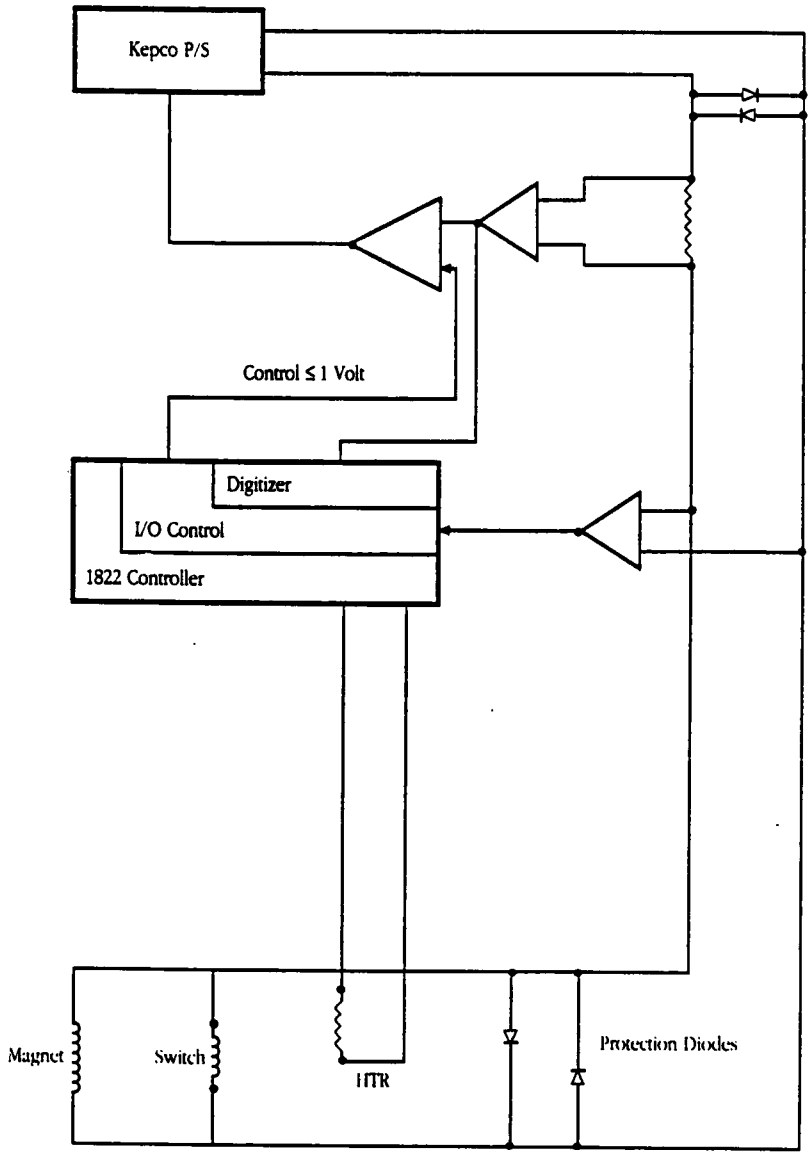

The MPMS magnet controls.

control system to "remember" the current previously stored in the magnet so the correct current from the power supply can be preset before energizing the persistent switch. Otherwise, if the power supply is set wrongly, the voltage across the switch will exceed the trigger voltage of the protective diodes, and current will flow through the diodes. When this happens, the current stored in the magnet will be dissipated in the diodes as the magnet is rapidly discharged.

3. Turn on the persistent switch heater and wait a few seconds to insure that the switch has been driven normal.

4. Change the current to the desired value. When the current approaches the intended current, there are two ways to reach it. One, called the "Oscillating Mode", allows the current to pass the target value at first, and then oscillate the current back and forth around the target value with a decreasing amplitude of oscillation. The other, the "No Overshoot" mode, permits the current to reach the target value only monotonically.

5. To see if the correct value of current is reached, the 1822 Controller reads the voltage across a reference resistor in series with the magnet power supply to insure that the desired current has been set. If the proper current is not flowing, it is adjusted to within acceptable limits, which are 1 gauss and 0.1 gauss in the low and high resolution mode, respectively.

6. When the final value of current has been reached with persistent mode operation, the switch heater is turn off and the system then waits a few seconds for the persistent switch to become superconducting. After that, the current is set to zero, and

the power supply is turn off. Meanwhile the polarity relays are reset to shunt the persistent switch. For the hysteresis mode, the current is maintained at the final value.

To choose the "oscillating mode" or "no overshoot mode" correctly is important. The magnetic field gradually relaxes as the flux lines in the magnet slowly creep through the superconducting windings in the persistent mode, which happens immediately after changing the field. Although the SQUID pickup coils are balanced to reject signals from any changes of the magnet, to a level of ~ 0.1 percent, the relaxation in the magnet still produces a substantial drift in the SQUID detector output due to its extreme sensitivity. The oscillating mode is able to reduces this field relaxation in the magnet greatly, hence minimizes the drift in the SQUID output. However, for hysteretic materials, the oscillating mode cannot be used. Thus it is very important not to let the sample be exposed to these field oscillations. In this case, the signal from field drift appears as a linear background, which is subtracted in the calculation of the magnetic moment.

The SQUID detector system The schematic SQUID sensing loops are shown in Figure 12, which comprises a set of pickup coils, a superconducting transformer and a RF SQUID sensor with its control electronics (Model 2000 SQUID Amplifier).

The SQUID pickup coils are a highly balanced second-derivative coil set with a total length of ~ 3 centimeters. The loops are designed to reject the uniform field from the superconducting magnet to a precision of approximately 0.1 percent, making the

Figure 12

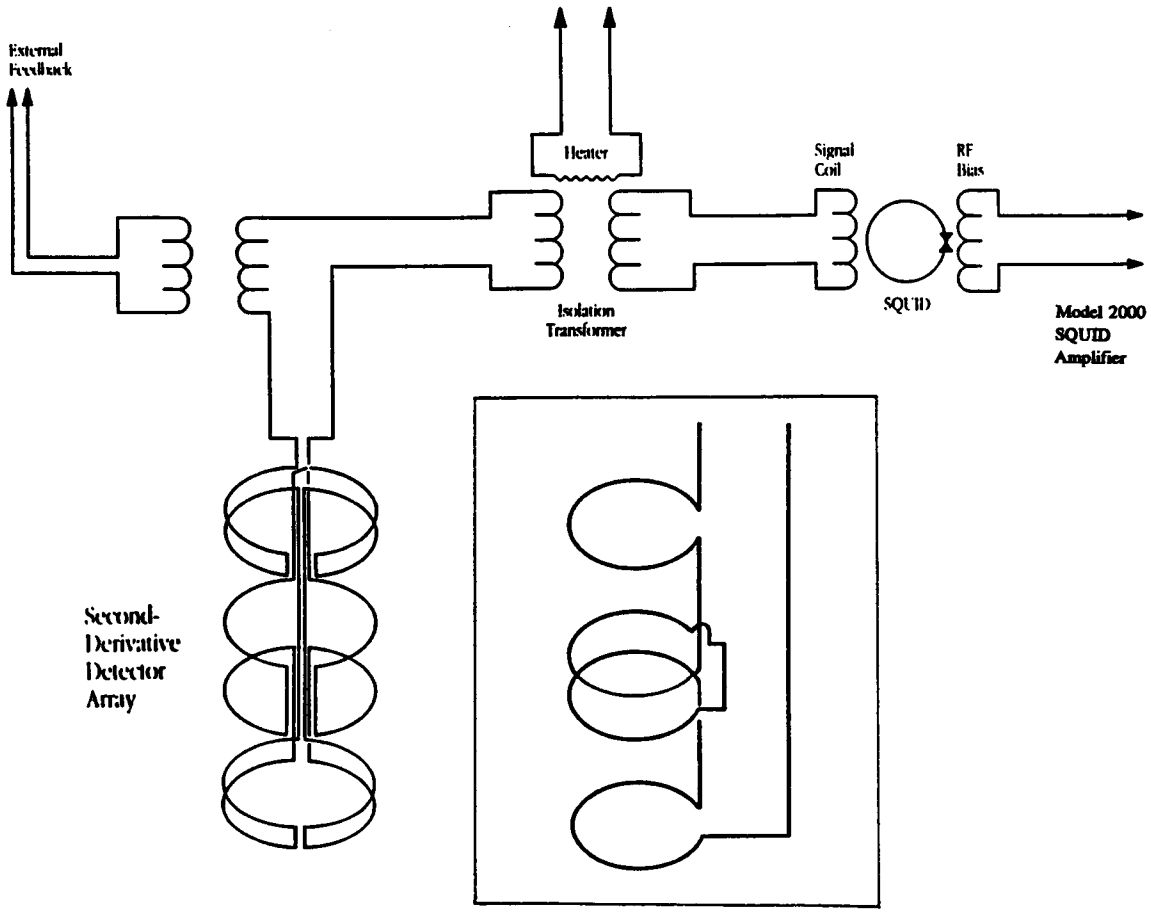

The MPMS transverse SQUID system; inset: the detector array for longitudinal system.

detector relatively insensitive to drifts in the magnet following changes of the field. The instrument can measure either the component of magnetic moment that is aligned with the field (longitudinal moment) or perpendicular to the magnetic field. The applied field is vertical. The longitudinal system uses a vertically aligned set of coils, wound in a horizontal plane, to measure the longitudinal moment, the pickup loop for measuring a transverse moment is wound orthogonal to the longitudinal pickup in an array (see the inset of Figure 12). Here we use only the longitudinal capability.

Signals detected in the pickup loops are coupled into the SQUID sensor through a superconducting transformer of -3 dB rolloff frequency about 20 kHz. The small heater winding, installed as part of the transformer, is to drive the transformer normal so that all persistent currents in the SQUID input circuit can be eliminated. The heater is turned on during all magnet charging, and at the beginning of each sample measurement (but not between individual scans of a measurement). The signals from the sensor are coupled to the Model 2000 VHF SQUID Amplifier for further processing.

II.3 Measurement of Transition Temperature

Measurements of transition temperature are performed using the SQUID magnetometer. The sample is first cooled to 5 K at zero field (ZFC). After the temperature is stabilized, a magnetic field of a few Gauss is applied with field parallel

to the c-axis of the sample. A shielding current is induced so as to cancel this applied field. The net magnetic inductance B(r) is zero inside the sample with $d > \lambda$, where d is the distance between r and the nearest surface, and λ is the London penetration depth. The magnetization M, which is defined as the average of microscopic M(r) over the sample, then is $-H/4\pi$.

With increasing temperature, $\lambda(T)$ increases, so that the field penetrates more of the sample and the magnetic moment decreases. At the transition temperature T_c, the signal vanishes. Hence, by plotting the moment versus temperature, T_c can be determined.

Without removing the applied field, the sample is cooling down slowly. The signal should reappear at T_c due to flux expulsion via the Meissner Effect. However, often with field cooling (FC), the measured moment is only a fraction of that in ZFC. Inhomogeneities and defects in the sample pin the flux lines. Nevertheless, the T_c determined in both cases should be identical if cooling is slow enough.

To illustrate this, Figure 13 plots the magnetic susceptibility versus temperature of sample 2, with a field of 10 G applied along c direction. The calculated demagnetization factor is $D \approx 0.34$. Both ZFC and FC signals disappear at $T_c = 91$ K.

Figure 13

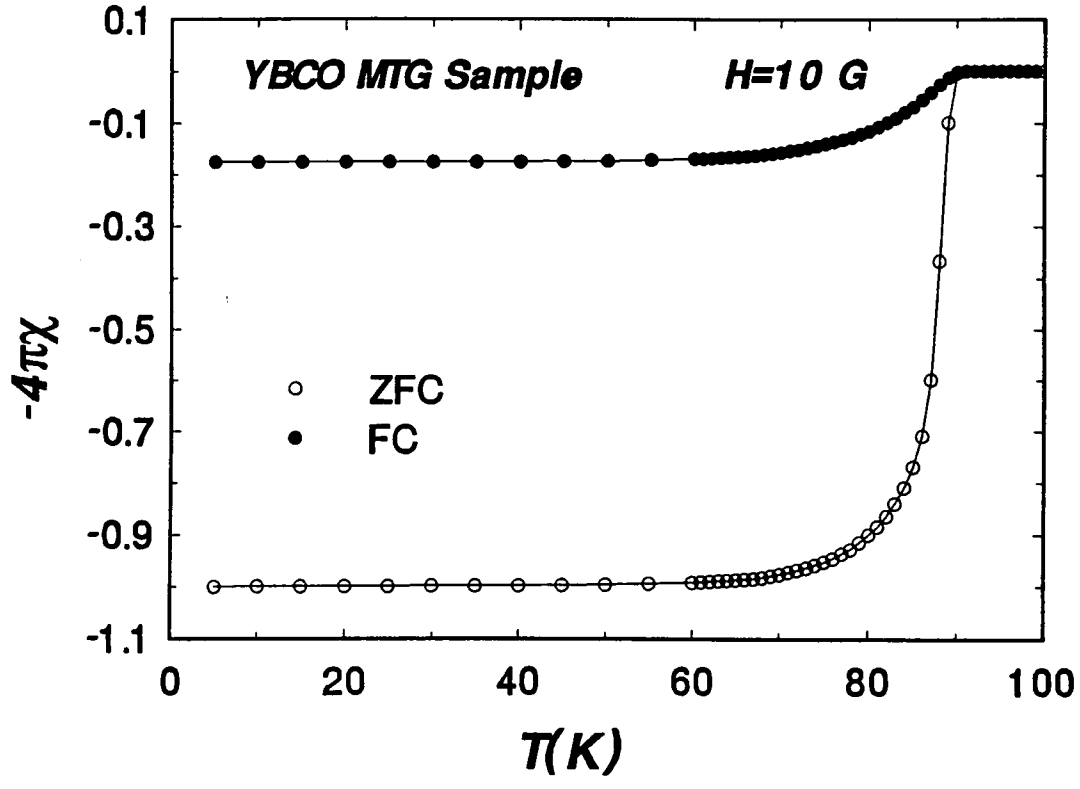

The magnetic susceptibility $4\pi\chi$ versus temperature T for the melt-textured $Y_1Ba_2Cu_3O_{7-\delta}$ sample.

There are a few things worth mentioning to make successful T_c measurements in the SQUID magnetometer: (1) Zero field cannot be acquired by just reducing the current from the magnet power supply to zero. After operation at high field, typically a residual field of 3 ~ 5 G remains in the superconducting solenoid. The technique for reducing this remnant field is to "reset" the magnet. In this option, the magnet first charges to 3.5 Tesla or more, then heat is applied to quench the magnet (for MPMSR2 with a 7 Tesla magnet, as used for later studies, it is not required to apply high field; instead, the whole magnet is heated to above the transition temperature of superconducting wires.) Then remnant fields below 2 G can be achieved. (2) The temperature changes step by step with the step size specified by the programmer. At each step, the measurement is made as the temperature is stabilized. To raise the temperature monotonically, the steps should be small, otherwise the system may overshoot the target temperature. (3) The demagnetization factor D is determined by the sample's geometrical shape. In some cases, thin films for instance, D could be very close to 1. The actual field profile in such a case is rather complicated and the field may well surpass H_{c1}. In such cases, the applied field should be as small as possible, provided that one can still get a sensible signal.

II.4 Measurement of Flux Creep

In performing flux creep measurements, the sample is cooled in zero field to the target temperature. Usually it is maintained there for a half hour after the temperature

is stabilized, and then the field is applied with H parallel to c-axis. If the critical current is large, as in the case for sample 1, or the effective radius of the sample is large, we cycle the field around the hysteresis loop by first applying -5 T and then increasing the field to the desired value, e.g. +2T, which helps the field to penetrate to the center of the sample; see the discussion in Chapter III on the critical state model. It is important that the field approaches the target value monotonically with no overshooting. When field reaches the desired value, measurement of the magnetic moment is started as a function of time. In general, the measurements continue for about 4-5 hours. In some cases, the measurements were prolonged up to $\sim 10^6$ s (four days). When one measurement cycle is finished, the temperature is warmed above T_c to make the sample virgin again before the next measurement.

While most experiments were made on the SQUID magnetometer, a few short period measurements were conducted in the VSM. For each machine there are some advantages and disadvantages. For the SQUID magnetometer, when the charging current reaches its final value, the heater of the persistent switch is turned off, which allows the supercurrent to flow in the solenoid with zero current from the power supply. This is called "persistent mode" operation, which provides very accurate and stable field. Along with good capacity of the liquid helium dewar and efficiency of thermal insulation, the measurements need not be interrupted for refilling the liquid helium, which makes it possible to perform flux creep experiments up to ~ 5 days duration. However, there are disadvantages in using the SQUID magnetometer. As we will show in the fourth

chapter, knowledge of the procedure for charging the magnet is important in the analysis of the flux creep data. If the field sweeps at a constant rate, it greatly reduces the difficulty in interpreting the early stage of magnetic relaxation. Unfortunately, charging of the magnet in the SQUID magnetometer is complicated. Figure 14 plots the charging current versus time. The procedure can be described in four stages: (1) The magnet is charged in almost constant rate of ~ 500 G/s, except at the beginning where the rate is higher. (2) When the current is close to the desired value, 1 T in this case, charging stops and the 1822 MPMS Controller reads the voltage across a reference resistor in series with the magnet power supply to check how far it should continue to charge; this procedure usually iterates two or three times to ensure that the target current has been set. (3) After the final value of current has been reached, the heater of the persistent switch is turn off and, after a few seconds, it changes to the persistent mode. (4) Then the power supply current is set to zero; the scan of the sample then starts in about 15 s and takes about 17 s to finish the measurement.

Because of these features, it is difficult to define the time origin for magnetic relaxation. Furthermore, the time for the first data point is blurred as the scan itself takes about 17 s. Hence, with the SQUID magnetometer, we are not able to probe the magnetic relaxation in the first ~ 100 s, which is important for high T_c superconductors with giant flux creep at the early stage. In experiments, the reliable data begin about 120 s after the field reaches the target value.

Figure 14

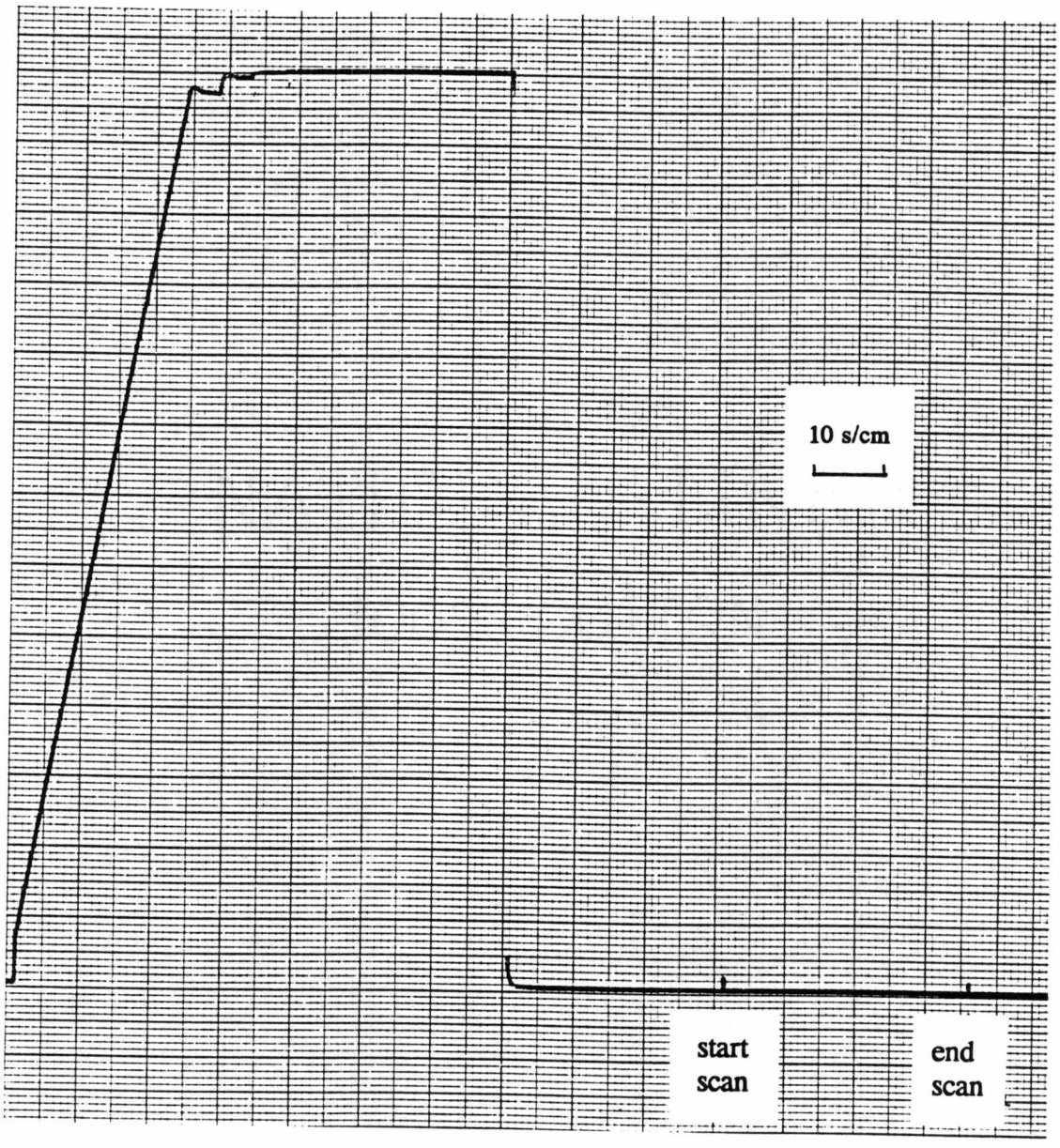

Magnet charging and sample scanning procedure in the SQUID magnetometer.

In the VSM, on the other hand, the magnetic field sweeps at a constant rate, which can be accurately controlled. The sample vibrates at 33 Hertz, generating an AC voltage in the pick-up coils, which is amplified and detected by a lock-in amplifier. The detected signal goes to a scanner and the data are collected by a computer; this process starts ~ 0.5 s after field reaches the desired value. Unlike the SQUID magnetometer, however, the VSM has no persistent mode. In addition, the liquid helium in the dewar supplies only a few hours of measurement and can not be refilled without stopping the measurement. Therefore, for flux creep measurements, the VSM is usable for only a short period of time.

A good way of studying magnetic relaxation is to combine experiments made by both the SQUID magnetometer and the VSM. We have done this somewhat differently, by using the VSM to measure the magnetization versus field sweep rate, which also provides information regarding flux creep in its early stage. A detailed discussion is presented in the last section of this chapter.

II.5 Measurement of Critical Current Density

The original meaning of critical current density is the highest current density the material can carry without dissipation of energy. However, at nonzero temperature, there is always dissipation, due to thermally activated flux motion. In practice, one

could measure the voltage drop across the superconducting sample. The conventional criterion for critical current density employed in transport measurement is 10^{-6} V/cm.

Measuring hysteresis loops M(H) provides an alternative way to find the critical current density. Indeed, the method provides a contactless way to measure this important property in samples with arbitrary shapes or small volumes for which it is impossible to employ transport measurements. In contrast to the measurement of transition temperature where the applied field must be quite small ($H < H_{c1}$), determining the critical current density requires that the field is large enough ($H >> H_{c1}$) to penetrate to the center of the sample. The theoretical basis of this method is the Bean model,[29] which provides the following relation:

$$J_c(H, T) = (\text{const.})\, M_{irr}(H, T)/R_{eff}$$

where M_{irr} is the irreversible magnetization, R_{eff} is an appropriate transverse dimension of the sample and the const. depends on the units of length, current density, and magnetization. If units of cm, A/cm^2, and Gauss are used for length, J and M, respectively, a cylindrical sample with radius of R_{eff} has the proportionality const. = 30; with a sphere, on the other hand, its value is 34. For a rectangular sample with transverse dimensions of L_1 and L_2 ($L_1 < L_2$), we use the "sandpile" formula:

$$J_c(H, T) = 40\, M_{irr}(H, T)/[L_1(1-L_1/3L_2)]$$

The hysteresis loop can be measured using either the SQUID magnetometer or the VSM. In the SQUID magnetometer, with a ZFC sample at fixed temperature, the applied field sweeps first from zero to +5.5 T, then sweeps back to -5.5 T, and again to +5.5 T. In this experiment, we use a "hysteresis mode," in which the persistent switch stays "open" and the magnet uses only external current. When field reaches the target value, charging stops and the stepping motor moves the sample up and down, performing a quick measurement scan ($\sim$5 s), and then charging continues toward the next target value. The results provide data of M versus H at those points set by the programmer. Contrarily, measurements made in the VSM gives continuous data for M(H).

In the VSM, we see that once the field reaches the target value and stabilizes, the signal diminishes immediately due to flux creep. Typically, the field sweep might be interrupted by a pause of 10-20 seconds. Values of J_c obtained in this way are called "*static*" values; in comparison, the values obtained during the field sweep are called "*dynamic*" values. In the SQUID magnetometer, it is easy to have *static* J_c, but not the *dynamic* case as the measurement itself takes about 5 s. A related phenomenon is that the signal increases with increasing field sweep rate. In fact, at lower sweep rate, it takes more time for the field to reach the target value. This means that the shielding current has more time to relax, which results in smaller moments. The question arises: what conditions are "standard" and how can the results be compared with those from transport studies.

Actually, the different values of J_c obtained with various conditions are equivalent to employing different effective field criteria in transport measurements.[30] The internal electric field E is proportional to $\partial <B>/\partial t \propto \partial M/\partial t$, where $<B>$ is the average of magnetic inductance. For the "*dynamic*" values with field sweep rate at 100 G/s, it corresponds to the E of $\sim 10^{-9} \sim 10^{-10}$ V/cm in the crystal. For the "*static*" case E can be much lower, depending on how long the pause is. Though the criterion for J_c used in the hysteresis loop measurements is not as clear as it in transport measurements, it seems that J_{c0}, the critical current density without thermal activation, differs from the observed J_c (with sweep rate at 100 G/s performed on the VSM) about a factor of 1.5 or less. Magnetic hysteresis loop measurements are a powerful and convenient method to determine the critical current density of high T_c superconductors.

II.6 Measurement of Magnetization Versus Field Sweep Rate

To understand the dependence of magnetization on the field sweep rate, we made magnetic hysteresis loop measurements with various field sweep rate at several fixed temperatures on the VSM.

The melt-textured-growth YBCO sample was chosen for this experiment as it has relatively larger mass that would contribute a bigger signal and improve the signal-to-noise ratio. The sweep rate ranged from about 4 G/s to 1000 G/s. At a low sweep rate,

it may take hours to finish a complete hysteresis loop, for instance ~7 hours for sweep field to 5 T and back to zero at sweep rate of 4 G/s. To use time and liquid helium efficiently, we chose a specific window of field, from 2.8 T to 3.4 T for example, for measurements at different field sweep rates. Outside this window, we sweep the field faster. Speaking more concretely, we swept the field at 500 G/s from zero to 2.8 T, then paused ~20 s to eliminate the influence of this fast rate, and after that swept the field at a specific rate up to 3.4 T, and finally swept back to zero field with the same high rate of 500 G/s.

Even with this technique, a complete experiment at a fixed temperature with over 15 curves at different sweep rates may take 6 hours. The temperature stabilization is of crucial importance for the success of the experiment. Any modest temperature fluctuations, e.g. 0.1 K, could strongly affect the relatively size of the signal. The major effect on temperature stabilization is the continuous decrease of liquid helium in the dewar, especially when the helium level lower than the capillary valve that supplies cooling gas in the jacket space of the sample tube. We solved this problem by continuously transferring liquid helium into the dewar during the measurements so as to keep the level constant. The temperature was much more stable with fluctuations of 0.02 K at T=27 K. This procedure greatly reduced the scatter in the measurements made at different sweep rates.

Chapter III

THEORETICAL BACKGROUND

The dynamics of vortices in the mixed state of high T_c superconductors is a very complicated issue. The motion of vortices is governed by the interactions among vortices themselves and between vortices and random defects which arise from the inhomogeneity of the material, grain boundaries, oxygen deficiencies or radiation induced defects. These interactions are *nonlocal*, which cause vortex behavior to be a highly correlated phenomena lying at the frontier of condensed matter physics and undergoing extensive study. In this chapter, we introduce some theoretical concepts related to the interpretation of our experimental results. The complete treatment of the instability of the vortex lattice and the various pinning theories can be found in references.[14,31,32,33,34]

III.1 Bean Critical State Model

In 1962, Bean[29] introduced the concept of the "critical current density" in the mixed state of type II superconductors. The theory successfully interpreted the magnetic hysteresis loops observed in superconductors when the applied field exceeded H_{c1}. Since then, the model has been widely adopted in analysis of magnetic properties, especially

in obtaining the critical current density for many small samples with arbitrarily shapes for which standard transport measurements are difficult or impossible.

The essential idea of the Bean model is that a material can carry a limited, macroscopic superconducting current density $J_c(T, H)$. Furthermore, when the material experiences any electromotive force, however small, this full current will be induced to flow locally. According to this picture, three states of current flow are possible when a magnetic field is applied: (1) for $H \leq H_{c1}$, there is no current flow if we neglect the surface current, (2) for $H_{c1} \leq H \leq H^*$, the sample is partially penetrated by the field with the field gradient $\partial h(r)/\partial r = J_c$ (Ampere's law), and (3) for $H \geq H^*$, the sample is fully penetrated by the field. The value of H^* for a cylindrical sample of radius of a, assuming that the critical current density is independent of the field, is the following:

$$H^* = 4\pi a J_c/10 \qquad (1)$$

where, practical units of Gauss, amperes/cm^2, and cm are employed. If the field is then reduced somewhat, the surface feels an emf oppositely directed to the one generated by the increasing field. Thus, the currents near the surface reverse. The configuration of local fields is shown in Figure 15. Consequently, the volume average of the magnetic induction B and the magnetization can be calculated by definition:

Figure 15

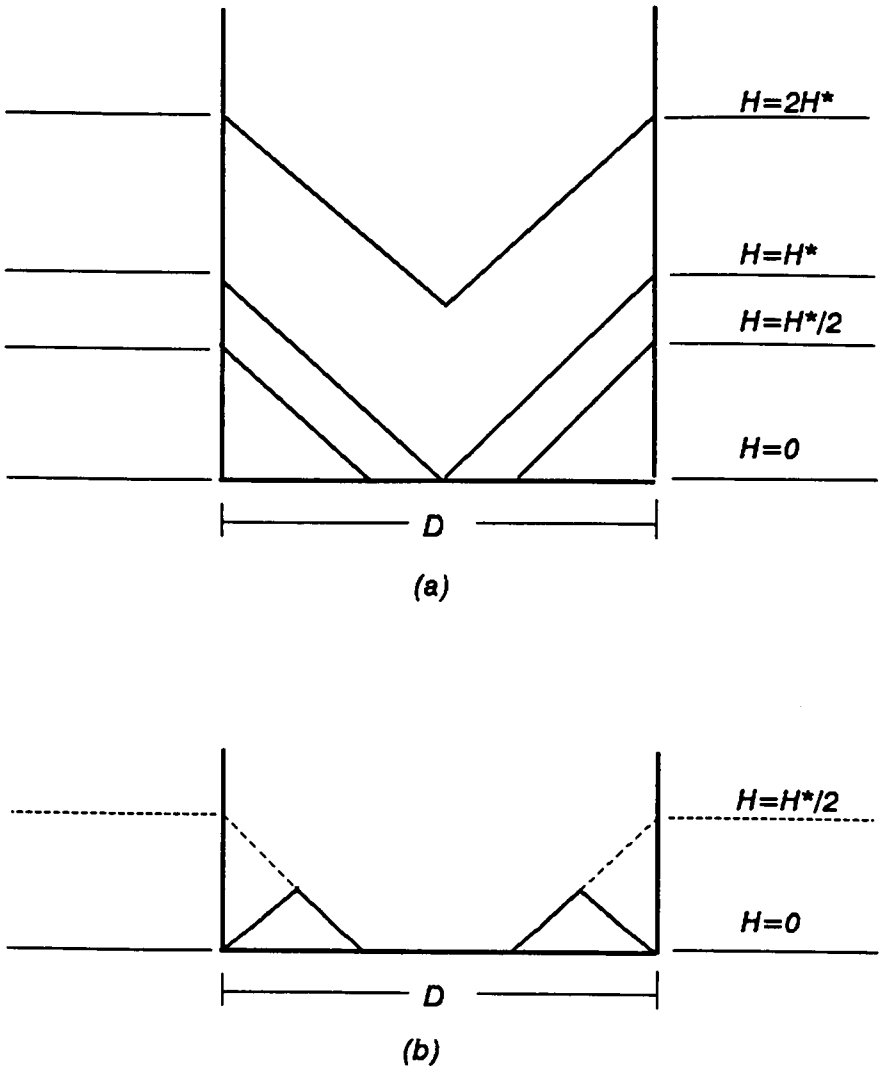

A plot of the local field in a slab after fields are applied parallel to the surface of the sample (after Bean, Phys. Rev. Lett. **8**, 250 (1962)): (a) fields applied with stepping up, (b) a field H*/2 has been removed.

$$B = \frac{1}{V}\int h(r)dv \qquad (2)$$

$$M = (B - H)/4\pi$$

According to this model, a cylindrical sample of radius of a experiencing an increasing field has the following magnetization M:

$$\begin{aligned} M &= -(H - H^2/H^* + H^3/3H^*)/4\pi \\ &= -[H - 10H^2/(4\pi aJ_c) + 100H^3/3(4\pi aJ_c)^2]/4\pi \qquad (H \le H^*) \\ M &= -H^*/12\pi \\ &= -aJ_c/30 \qquad (H \ge H^*) \end{aligned} \qquad (3)$$

Hence, the Bean model provides a simple relation between the critical current density and the magnetization.

In the above discussion, the critical current density is assumed to be independent of field. The generalization to a field dependent J_c and associated local field profile are schematically shown in Figure 16 a and 16 b, respectively. As shown in the plots, if an increment of field δH is applied, the curve is displaced inward by an amount $\delta r = 10\delta H/4\pi J_c(H_a)$, where H_a is the field at the surface. In this case, the amount of flux entering the sample is proportional to H and δr: $\delta\Phi = H\delta r = 10H\delta H/4\pi J_c$

Finally, we should note that the assumption of an infinitely sharp front on the curve of current density against distance is never completely valid. There is always an exponentially decreasing tail to the curve. It is similar to the London penetration depth

Figure 16

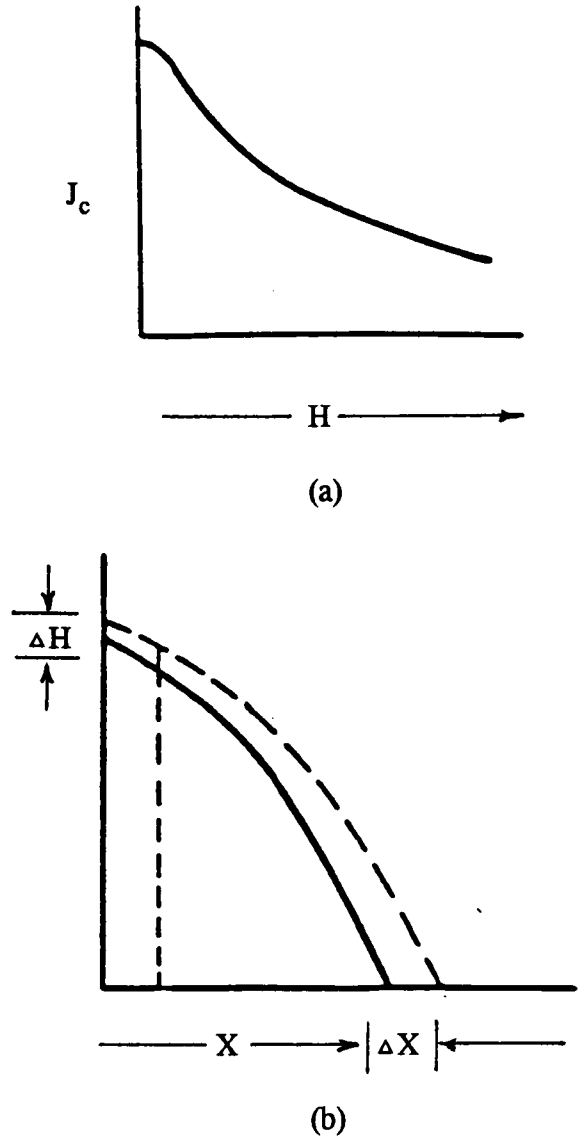

Effect of a field dependent critical current density: (a) an arbitrary, schematic dependence on field, and (b) the internal field profile under this condition.

in which the field decreases from H_{c1} to zero. This feature can be neglected if H* is much larger than the H_{c1} as usually is the case for high T_c superconductors. The more important point is that the model does not consider thermal activation of vortices. For low T_c superconductors, this is not a serious problem since the flux creep is relatively slight. However, the giant magnetic relaxation in high T_c superconductors greatly influences the observed hysteresis loops. A discussion can be found in the work of Schnack et al.[35]

III.2 Anderson-Kim Flux Creep Theory

As discussed in the previous section, a type II superconductor can carry supercurrents with current density J_c. Application (or removal) of a magnetic field induces such currents, in which case they circulate within the material. In the critical state, the field lines are stationary. Since the flux lines experience a Lorentz force $\boldsymbol{J_c \times B}$, there must be in the critical state other forces upon the flux lines that balance this driving force. While the precise nature of this pinning is still subjected to much study, it is well recognized that the pinning is due to the interaction between vortices and inhomogeneities in the material. The pinning leads to an internal gradient of the flux density which starts from the edge and is directed towards the inside of the material. Kim et al[11] indicated that the Bean critical state model may be interpreted using the following relation:

$$\alpha(T,\ B) = J_c(B + B_0) \tag{4}$$

where α(T, B) is a structure-sensitive function of temperature and field marking the pinning strength of the material and B_0 is a constant. The vortex pinning barrier in the most extreme inhomogeneous case would be

$$\Delta F_{max} = (F_n - F_s)d^3 = (H_c^2/8\pi)d^3 \tag{5}$$

where H_c is the critical field, d is the dimension of a flux bundle, F_n and F_s are the free energy of the normal and superconducting state, respectively. Actually, in any reasonable case, the pinning effect will be much smaller. P. W. Anderson[10] introduced an arbitrary structure-sensitive parameter p to represent the average fractional amount of pinning:

$$U_0 = p\Delta F_{max} = p(H_c^2/8\pi)d^3 \tag{6}$$

Then the total free energy the bundle must overcome for jumping to another barrier is

$$U = U_0 - JBld^3 \tag{7}$$

where l is the dimension of a pinning well. Now, the probability for jumping parallel to the force direction is much larger than that for the reverse direction, if the Lorentz force is large as in the critical state. In such cases, if we neglect the reverse jumps, the rate that bundles hop over the barrier is

$$\nu = \nu_0 \exp(-U/k_B T) \tag{8}$$

where $\nu_0 \sim 10^{10}$/s is an appropriate attempt frequency. For a hollow cylindrical sample of radius a and thickness w having an interior field H' and outer field H (H > H'), the

equation determining the creep rate then is the following:

$$\frac{1}{H^*}\frac{\partial(H-H')}{\partial t}=\frac{2d\nu_0}{ca}\exp(-\frac{U_0-JBd^3}{k_BT}) \tag{9}$$

where c is a parameter giving the number of pinning barriers. From this theory, we have several important conclusions:

(1) It is obviously predicted that there is no precise "critical state," since thermally assisted flux creep takes place at any finite temperature. However, one may define the critical state as that at which the rate falls below a practically observable limit. If we use ν_{cri} to represent this critical rate, we have

$$(JB)_c=\frac{pH_c^2d}{8\pi}-(\frac{k_BT}{d^2})\ln(\frac{\nu_{cri}2d\nu_0}{ac}) \tag{10}$$

Comparing this to Kim's formula gives

$$\alpha=\frac{pH_c^2}{8\pi d}-\frac{k_BT}{d^4}\ln(2\nu_{cri}d\frac{\nu_0}{ac}) \tag{11}$$

(2) Considering that a bundle cannot contain less than one flux quantum Φ_0, then B in the above formula can be written as $B + B_0$, where $B_0=\Phi_0/d^2$. If the bundle is considered to be $\sim 10^{-5}$ cm, then $B_0 \sim 2000$ G, which is very close to Kim's values.

(3) From Eq. (9), the time dependence of current density can be derived. Assuming the current density is uniformly flowing around the sample, thus $J=dB/dr=(H-H')/w$. Defining $J_0=k_BT/lBd^3$, then Eq. (9) becomes

$$\frac{1}{H^*}\frac{\partial J}{\partial t} = \frac{2dv_0}{caw}\exp(-\frac{U_0}{k_BT} + \frac{J}{J_0}) \qquad (12)$$

Using the initial condition that at t=0, $J=J_{c0} \equiv U_0/H^*d$ and introducing a time scale $\tau \propto \exp(U_0/k_BT)$, then Eq. (12) gives

$$J(t) = J_{c0}[1 - \frac{k_BT}{U_0}\ln(1 + \frac{t}{\tau})] \qquad (13)$$

This characteristic logarithmic time dependence was verified by experiments of Kim *et al.*[11] on a NbZr thin walled hollow cylinder and has since been observed in many conventional low T_c superconductors. The concept of thermally activated motion of fluxoids is now widely accepted.

Beasley *et al*[20] (BLW) extended and reformulated the Anderson-Kim (A-K) theory. In the later treatment, flux motion was written in terms of a nonlinear diffusion equation, in analogy with the equation for mass transport. The flux-flow density **D**, the amount of flux that crosses a line perpendicular to B and ∇B per unit length and time, is written as

$$D = -\frac{\nabla B}{|\nabla B|} Blv_0\exp(-\frac{U(B,|\nabla B|)}{k_BT}) \qquad (14)$$

where l is the average distance by which a flux bundle moves in a thermally activated jump. Conservation of flux leads to the flux creep equation:

$$\frac{\partial B}{\partial t} = \nabla[\frac{\nabla B}{|\nabla B|} Bl\nu_0 \exp(-\frac{U(B,|\nabla B|)}{k_B T})] \tag{15}$$

For a cylindrical sample, the equation becomes

$$\frac{\partial B}{\partial t} = -\frac{1}{r}\frac{\partial}{\partial r}(rD) \tag{16}$$

where D is the radial component of **D**. The total flux Φ entering the specimen, the experimentally observable quantity, is obtained from the relation:

$$\frac{\partial \Phi}{\partial t} = -2\pi\rho D(\rho,t) \tag{17}$$

where ρ is the specimen radius. This equation, as we see in the next chapter, provides a way to probe the activation energy via flux creep measurements.

The strategy for obtaining B(t), or M(t), is first to calculate D. The equation for finding D are:

$$\frac{\partial D}{\partial t} = \frac{\partial D}{\partial B}\frac{1}{r}\frac{\partial(rD)}{\partial r} \pm \frac{\partial D}{\partial|\nabla B|}\frac{\partial}{\partial r}(\frac{1}{r}\frac{\partial(rD)}{\partial r}) \tag{18}$$

where

$$\frac{\partial D}{\partial B} = \frac{D}{k_B T}[\frac{\partial U}{\partial B} - k_B T\frac{\partial(\ln(B\nu_0 l)}{\partial B}] \tag{19}$$

and

$$\frac{\partial D}{\partial|\nabla B|} = \frac{D}{k_B T}\left[\frac{\partial U}{\partial|\nabla B|} - k_B T \frac{\partial(\ln(B\nu_0 l)}{\partial|\nabla B|}\right] \tag{20}$$

The $\pm$ signs in Eq. (18) refer to positive and negative ∇B (increasing and decreasing field), respectively. The analysis of this set of equations shows that the relative changes of $U - k_B T \ln(B\nu_0 l)$ in time are roughly a factor of $k_B T/U$ smaller than the relative changes in D, and therefore negligible compared to changes of D itself. This is the case for the conventional low T_c superconductors, whose $k_B T/U$ is rather small. Thus $\partial D/\partial B$ and $\partial D/\partial|\nabla B|$ have negligible time dependence and can be evaluated at some time t_1 after the critical state is established; the total derivative of $U - k_B T \ln(B\nu_0 l)$ with respect to r is approximately zero. The Eq. (18) can be rewritten as

$$\frac{\partial D}{\partial t} = \pm \frac{D}{k_B T}\left(\frac{\partial U}{\partial|\nabla B|}\right)_{t_1}\left[\frac{\partial}{\partial r}\left(\frac{1}{r}\frac{\partial(rD)}{\partial r} - \frac{\partial(rD)}{r\partial r}\left(\frac{\partial \ln|\nabla B|}{\partial r}\right)_{t_1}\right)\right] \tag{21}$$

The results from this equation are the following

(1) Assuming $D(r, t) = T(t)R(r)$, the equation is separated into a time-dependent part and position-dependent part. For T(t), we have

$$\frac{\partial T(t)}{\partial t} = \pm T^2(t) \tag{22}$$

with solution

$$T(t) = \mp 1/t \tag{23}$$

The inverse dependence of D on time leads to the logarithmic relation: $\Phi \propto \ln(t/\tau)$, as found in A-K theory. However, this result is clearly based on the assumption that the

time dependencies of $\partial D/\partial B$ and $\partial D/\partial|\nabla B|$ are small, so that the two functions can be replaced by their values calculated at some time t_1. In low T_c superconductors, both B and ∇B change very slowly in time, making this simplification acceptable. For high T_c superconductors, on the other hand, the time dependence of these quantities are not negligible, which introduces some new phenomena in these novel materials.

(2) The equation for R(r) is much more complicated and the solution is not analytical. The important thing is that the value of R at the boundary ρ is related to the logarithmic creep rate, which is experimentally measurable:

$$d\phi/dln(t) = \pm 2\pi\rho R(\rho) \tag{24}$$

If $|\nabla B|_{t1}$ and $(\partial U/\partial|\nabla B|)_{t1}$ are expanded in powers of (ρ-r) and only the first powers of (ρ-r) are adopted, it is found that

$$\left(\frac{d\phi}{dln(t)}\right)^{\pm} = \pm\frac{1}{3}\pi k_B T\rho^3(\partial U/\partial|\nabla B|)^{-1}_{t1,\rho}(1\pm\delta) \tag{25}$$

where $\pm$ signs refer to positive and negative $\partial B/\partial r$. The factor δ is a function of U, B, and $\partial U/\nabla B$, with each evaluated at the surface and at a fixed time t_1 in the critical state. This factor takes into account the effects of increasing or decreasing the applied field. It can be eliminated by using the average of the creep rates for increasing and decreasing fields: $(d\Phi/dt)_{ave} = [(d\Phi/dt)\uparrow + (d\Phi/dt)\downarrow]/2$. Thus, Eq. (25) indicates that the analysis of flux creep measurements can yield the interesting quantity $(\partial U/\partial|\nabla B|)_{t1}$, the implicit dependence of pinning energy on current density.

A few comments on the BLW theory are worth mentioning again: (1) The characteristic logarithmic time dependence of magnetic relaxation predicted by A-K theory is preserved in the more general solution but with a restriction. As shown above, this result depends on kT/U being small, so that one can neglect the time dependencies of the quantities $\partial U/\partial B$, $\partial U/\partial|\nabla B|$, and the quantity in the bracket of Eq. (20). One must be cautions in extending the theory to HTSC, where kT/U can be much larger. (2) The dependence of the activation energy, $U_0 - fVX$, on a bundle of vortices with f representing the Lorentz driving force, on the current density should be nonlinear. Figure 17 schematically illustrates this dependence at a fixed field. The shaded area illustrates the critical state region. According to Eq. (7), it is clear that the activation energy U_0 corresponds to the intersect of the tangent to the curve in the critical state region.

III.3 Vortex Glass Theory

At a time when many scientists expressed doubt as to the potential of HTSC for applications because of the giant flux creep, Fisher[14] proposed that in bulk disordered system (but not thin films), there exists a sharp equilibrium phase boundary separating the flux flow phase (at high temperatures and fields) from the flux creep phase at low T and $H \geq H_{c1}$ (see Figure 1). According to the theory, the low T phase, referred to as a vortex glass phase, is a true superconducting state at low current density. The

Figure 17

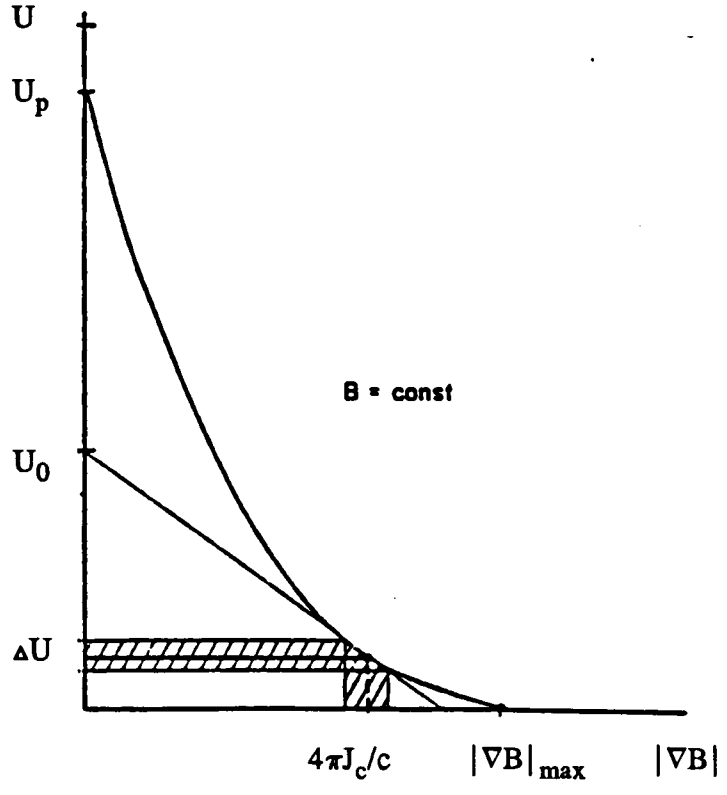

Schematic representation of the effective pinning potential U as a function of J for a constant field (after Beasley et al., Phys. Rev. **181**, 682 (1969)). The shaded area illustrates the critical state region.

theoretical formulation assumes the presence of random disorder at some level.

The theory indicates that in the mixed state, the Hamiltonian $H = H_0+H_1+H_p$ for the system of vortices can be represented in terms of 2D bosons with

$$H_0 = \int d^2r[\frac{-T^2}{2\epsilon_1}\Phi^+(r)\nabla^2\Phi(r) + \frac{1}{4\pi}(H_{c1} - H)B(r)],$$

$$H_1 = \frac{1}{2}(8\pi^2\lambda^2)^{-1}\int d^2r d^2r' B(r)K_0[\frac{r-r'}{\lambda}]B(r'), \qquad (26)$$

$$H_p = \int d^2 V_p(r,z)B(r)$$

where $\Phi(r)$ is a boson field operator, $B(r) \equiv \phi_0\Phi^+(r)\Phi(r)$ (ϕ_0=hc/2e) is proportional to the vortex line density, the modified Bessel function $K_0(x)$ gives the interaction between vortex lines, $\epsilon_1 = H_{c1}\phi_0/4\pi$ is the vortex line tension, and $V_p(r,z)$ is a random pinning potential. Gaussian disorder, uncorrelated in space and "time" with mean zero and variance Δ, is assumed for V_p. After replacing and employing a path integral representation of the partition function $Z=TrT_z[\exp(-T^{-1}\int dz H(z))]$, where T_z is an "imaginary time" order product, an ensemble average over V_p can be performed, yielding an effective replicated boson Hamiltonian[14,36]

$$H_n = \sum_{\alpha=1}^{n}[H_{0,\alpha} + H_{1,\alpha}] - \frac{\Delta}{T}\int dr \sum_{\alpha,\beta} B_\alpha(r)B_\beta(r) \qquad (27)$$

with α, β=replica indices. The equation describes an n boson system with *attractive* interreplica interaction. In the dilute limit, bosons in different replicas should bind together to form an n-molecule bound state which would undergo an n-boson

condensation at T→0. This indicates a disorder-dominated vortex-glass instability. It is proved that even at the n→0 limit the instability survives with $\partial\Delta/\partial n = 2(1-T/T_g)\Delta$. Thus for $T > T_g$, the pinning disorder scales to zero at long length scales and a vortex-liquid phase is obtained; for $T < T_g$, however, Δ grows with n, which drives the system into a new, disorder-dominated phase called the vortex glass state.

The vortex-glass phase is characterized by a nonzero Edwards-Anderson order parameter, although there is no conventional off-diagonal long-ranged order. The nonzero Edwards-Anderson order parameter is:

$$q_{EA} = \frac{1}{V}\int dx\, |\langle \psi(x)\rangle^2|$$

where ψ is a gauge-invariant order parameter.

In the 3D case, with a vortex-loop of size L, the jumping volume scales as a positive power (≤ 1) of L, giving an activation energy $U \sim (1/J)^{\mu}$ with a universal exponent $\mu \leq 1$. Hence, a nonlinear voltage response is predicted:

$$V \sim \exp[-(J_c/J)^{\mu}] \qquad (29)$$

Thus, $\rho \sim \exp(-(J_c/j)^{\mu})$ becomes zero at low J. Then in magnetic relaxation where $(\partial M/\partial t \sim V)$, the theory predicts $\delta M(t) \sim (\ln t)^{-1/\mu}$, which can be tested in magnetic relaxation experiments.

Chapter IV

EXPERIMENTAL RESULTS AND ANALYSIS

In this chapter, we report the main results of our studies on two YBCO samples. The chapter is composed of four sections. In the first section, long term flux creep experiments are discussed, showing that the decay of supercurrents in HTSC is non-logarithmic. The second section reports on the influence of field sweep rate on measurements of magnetic hysteresis loops. In the third section, we combine long-term flux creep experiments and magnetic hysteresis loop measurements with varying field sweep rate. It expands greatly the time window for observing magnetic relaxation, which allows us to effectively test flux creep models in the recent literature. In the last section, the temperature and the field dependence of the activation energy is presented based on an analysis of flux creep measurements.

IV.1 Non-Logarithmic Magnetic Relaxation in $Y_1Ba_2Cu_3O_{7-\delta}$ Superconductors

Among the most fascinating and widely studied features of high temperature superconductors are their magnetic properties, both "static" and time-dependent. In

the vortex state, a rapid relaxation of the irreversible magnetization is generally observed [6,7,37], with many researchers reporting[38,39,40,41] a logarithmic time decay of magnetization M, $M(t) \sim \ln(t)$. In recent studies, however, we have found significant departures from a precisely logarithmic dependence, under conditions that rule out any explanation based on an approach to the equilibrium magnetization. The current study was performed using a well characterized single crystal of $Y_1Ba_2Cu_3O_7$ (sample 1, see II.1) irradiated with protons to create many defects and develop a high critical current density J_c. The use of a single crystal with $H \| c$-axis eliminated questions of crystalline anisotropy that arise with polycrystalline samples. Our results are well described by an "interpolation formula" from vortex glass theory[14], which has recently provided an explanation[42] for the widely observed plateau in the flux creep rate d[ln(M)]/d[ln(t)] as a function of temperature T. As such, the vortex glass model of HTSC's is supported by the present results, although other questions arise. An alternate description of comparable accuracy is provided by suitably generalized, conventional flux creep theory.

The magnetization M(t) was observed on the SQUID magnetometer for times up to $3.5\ 10^5$ s (~4 days) for a broad range of temperatures. To illustrate, Figure 18 shows M as a function of ln(t), for H 1 T at T = 30 K. It is apparent that for a sufficiently short observation interval, the dependence appears logarithmic in time. However, the slope dM/d[ln(t)] decreases significantly with time as M and J_c decrease, from 58 G in the first hour of measurement to 41 G after ~2-3 10^5 s. The important features are that the curvature begins very early, continues throughout the entire

Figure 18

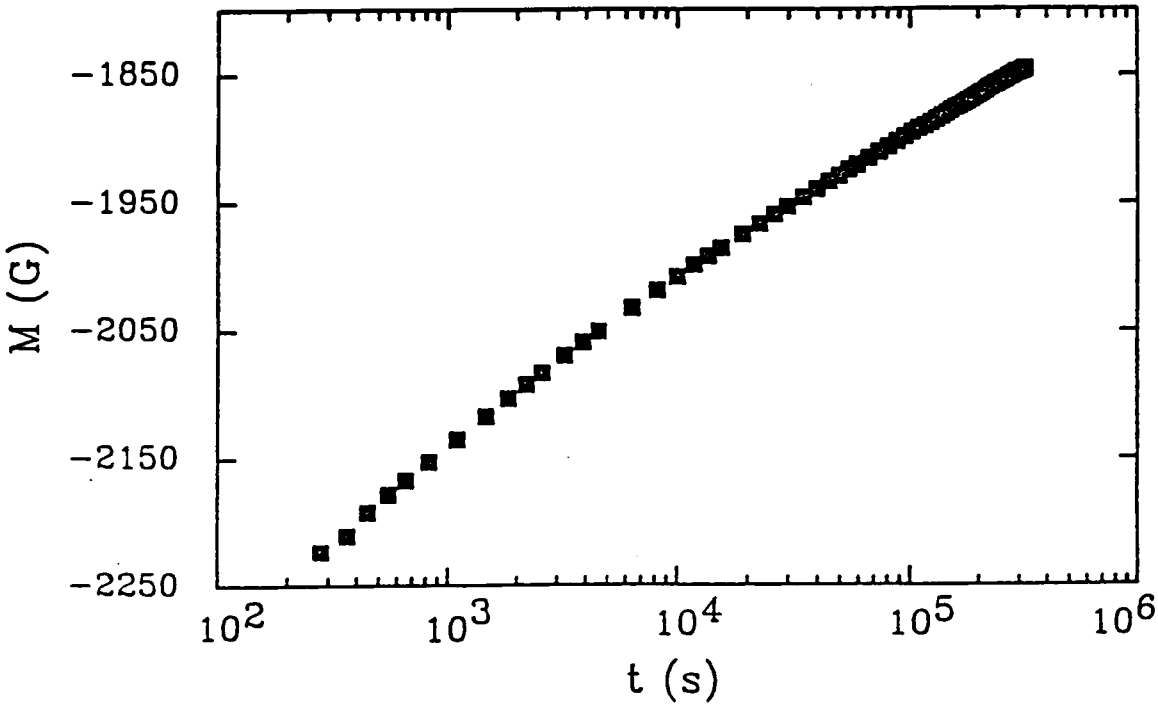

Semilogarithmic plot of Magnetization M(G) vs. time t(sec) for single crystal $Y_1Ba_2Cu_3O_{7-\delta}$ at T = 30 K with applied field H ‖ c and H=10 kOe. Curvature is apparent everywhere.

measurement, and occurs at all temperatures investigated. This study complements the work of Xu *et* al[43], who pointed out the experimental complication of nonlinearities at higher temperatures and brought renewed attention to the question of how the effective pinning potential depends on current density. The nonlogarithmic time dependence of M(t) is more apparent in our study, however, where the observation times were up to 20 times longer.

According to the standard Anderson-Kim theory,[10,11] the evolution of magnetization can be described by the equation: $dM/dt \propto e^{-U_0/kT} \sinh(J/J')$. Here U_0 is the height of the pinning energy barrier and J′, which has dimensions of current density, is a function of temperature T and magnetic field **B**. The solutions of this equation are:

$$M(t) = \begin{cases} M_0 + (kT/U_0)\ln(t/t_0) & J > J' \text{ or } t < t^* \\ M_{eq} + M' e^{-t/t^*} & J < J' \text{ or } t > t^* \end{cases} \qquad (30)$$

where conventionally $t_0 \sim 10^{-10}$ - 10^{-12} s. In our experiments, the largest relative change of M is less than 25% (at T = 60K). Since $M \propto J$, the relative change in J/J′ of no more than 25% indicates that the observation time is too short to observe the magnetic relaxation cross over from a logarithmic form to an exponential form in the phase space of this experiment. It is interesting, however, that a fit to the exponential form Eq. 30 gives the impression of a good fit. This is illustrated in Figure 19, a plot of $\ln(M/M_0 - 1)$ vs t. The problem with this analysis is that it yields unphysical values for the equilibrium magnetization M_{eq}. For example, such an analysis gives the values

Figure 19

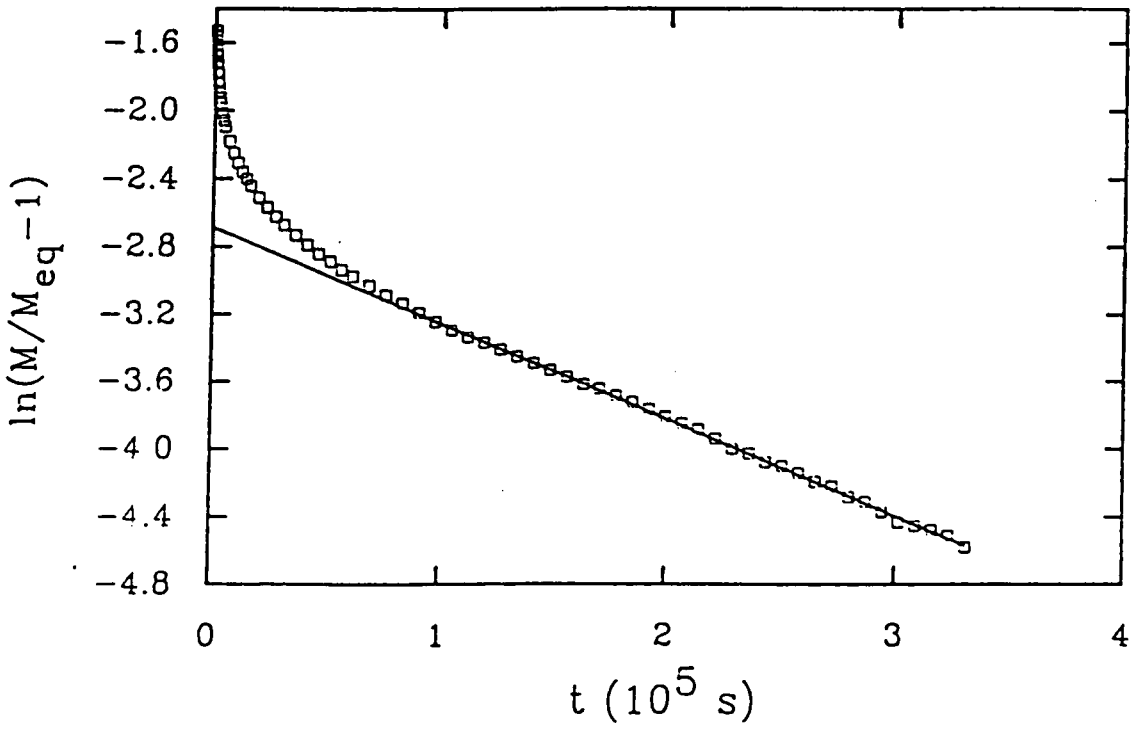

Exponential decay: a plot of $\ln(M/M_{eq}-1)$ vs t. The deduced equilibrium magnetization $M_{eq} \approx -1800$ G is unphysically large.

M_{eq} = -1800 G and -500 G at 30 K and 60 K, respectively. In contrast, hysteresis measurements of M show that M_{eq} ranges from a few tens of Gauss at 30 K to a few Gauss at 60 K, much smaller than the irreversible magnetization. The true equilibrium magnetization is orders of magnitude smaller than the fitted values and it is evident that some other mechanism is operative in these studies. Alternative forms[44] for the time dependence of M, including a "stretched exponential" $\sim\exp[-(t/\tau)^{\alpha}]$ and power law $\sim t^{\beta}$, also gave unsatisfactory results.

A more tenable explanation is the vortex glass model of Fisher,[14] who argued that the single barrier height assumed by A-K theory is not appropriate in these high T_c materials. Instead, the current decay obeys an "interpolation" formula

$$M(t) = M_0/[1 + (\mu kT/U_0)\ln(t/t_{eff})]^{1/\mu} \qquad (31)$$

where $\mu \leq 1$ is a temperature-independent exponent, M_0 corresponds to J_{c0}, the critical current density without thermal activation, and t_{eff} is a macroscopic, effective time scale for vortex bundles to jump.

Our experimental data are described very well by Eq. (31), which we write as an inverse power relation

$$M(t)^{-\mu} = M_0^{-\mu} + C(T)\ln(t) \qquad (32)$$

where μ, M_0, and C(T) are treated as fitting parameters. An example is shown in Figure 20, a plot of $M^{-\mu}$ at 30 K as a function of ln(t). From least squares fits to this

expression, we obtain for μ (H = 1 T) at temperatures of 7, 10, 20, 30, 40, 50, 60, and 70 K, the values 0.7, 1.1, 1.5, 1.9, 1.65, 1.4, 1.1, and 0.57, respectively, with uncertainties of ± 0.15. These values are plotted vs. T in the inset of Figure 20. Most of these results lie within the theoretical bound $\mu \leq 1$, with a grouping of points near $\mu = 1$. However, some μ values exceed this bound, e.g. at 30 K where the signal-to-noise was extremely good. In addition, μ appears to decrease almost linearly with temperature above 30 K and trend toward zero close to T_c. Within the vortex glass framework, we have no explanation for either the temperature dependence of μ or for the values >1.

In an alternate formalism based on collective pinning, Feigel'man et al.[15,45] obtain similar expressions for M(t) where the exponent μ depends on **B**, J, and T. In a weak field, low temperature limit for the 3D case, they obtain $\mu = 0.15$. For intermediate fields where collective creep is dominated by small flux bundles (size $<<$ λ_L), then $\mu = 3/2$. This is its maximum value and μ can be expected to decrease at higher fields and temperatures, with the exact values depending on the dimensionality and relative scale of the system. Qualitatively, this is very similar to the dependence shown in the inset to Figure 20. Furthermore, the maximum at 30 K is near the theoretical value of 3/2. Additional studies are underway to delineate more fully the temperature and especially magnetic field dependence of the non-logarithmic relaxation. Preliminary results indicate that μ increases as H increases, passes through a maximum, and decreases at still higher fields. This behavior is very similar to that predicted

Figure 20

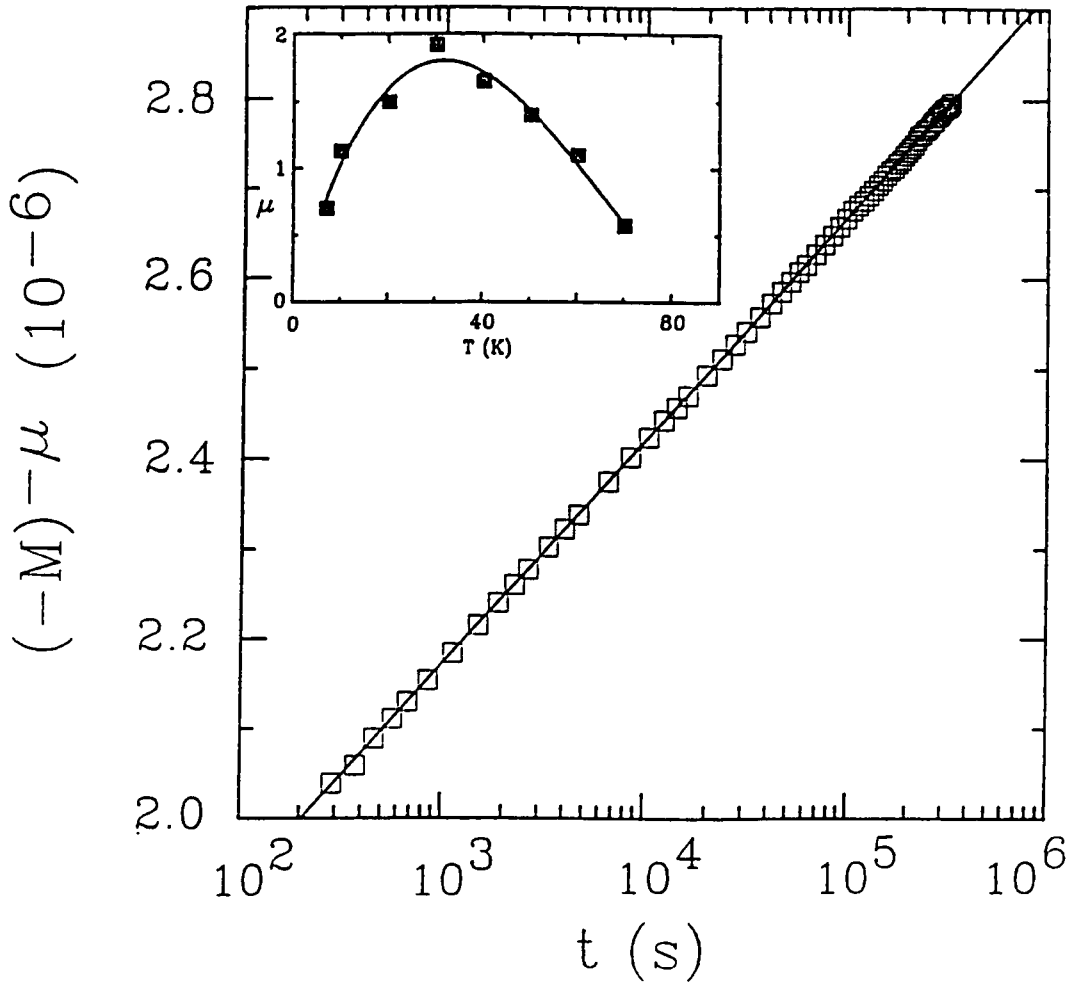

Interpolation-formular analysis: semilogarithmic plot of $[-M(t)]^{-\mu}$ vs t, with μ as a fitting parameter. Inset: exponent vs T, for H $\|$ c axis and H=1 T.

theoretically.[15,45]

Another perspective on the non-logarithmic time dependence of magnetization can be obtained from the refined A-K theory by Beasley *et al.* (BLW).[20] From Equation $\partial\phi/\partial t = -2\pi\rho D(\rho,t)$, we have (see discussion in III.2),

$$\frac{\partial M}{\partial t} = D(\rho,t)/2\pi\rho \tag{33}$$

where the flux-flow density D is expressed in Eq. (14). The activation energy in D is $U = U_0 - |f|vx$, where f is the Lorentz driving force; and x is the pinning length. If the driving force is large, as in our case, the expression for U is correct; otherwise, the hopping may become two-dimensional.

As discussed in III.2, conventional superconductors have $k_BT << U_0$. Thus, the change of $|\nabla B|$ ($|\nabla B| \propto j$) is so small during the magnetic relaxation measurement that it is a good approximation to neglect the time-dependence of $\partial U/\partial|\nabla B|$ and $\partial \ln|\nabla B|/\partial r$ in **D**. In that limit, the solution yields $\mathbf{D} \propto 1/t$, which leads to a logarithmic evolution of the magnetic relaxation. But, in HTSC materials, the shielding current changes quickly in the first few hours. Hence, the time-dependence of J is not negligible. We should expect to see a nonlogarithmic decay of magnetization, which can provide information concerning U_0 as a function of J.

We have found an empirical "double logarithmic" relation which describes the data very well:

$$M(t) = M_0 + a(T)\ln[1 + \ln(t/t_{eff})] \tag{34}$$

where M_0, a(T), and t_{eff} are fitting parameters. Figure 21 shows the resulting fit of this expression to the experimental data. In general, the "goodness-of-fit" R^2 exceeds 0.99996 in the linear regressions, and these R^2 values are nearly identical to those obtained when fitting the interpolation formula, Eq. (32). If we assume that the deviation from logarithmic decay is due totally to dependence of U_0 on J, we can get the functional form of U rather straightforwardly from Eqs. (14), (33) and (34) as follows:

$$U/kT = [\ln(Bd\nu_0/2\pi\rho) + \ln(t_{eff}) - \ln(a) + J_0/J_s] + \exp(-(J-J_0)/J_s - J/J_s \tag{35}$$

Here $J_s = a/\wedge$ ($\wedge$ = R/30) is a factor which relates M and J by $M = -\wedge J$, with J in units of (A/cm^2) and M in Gauss. Assuming $M_0 \approx \wedge J_0$ and considering that $U(J_0) \sim 0$, we have $-\ln(t_{eff}) = 1 + \ln(Bd\nu_0/2\pi R) - \ln(a)$. Then, we have

$$U/kT = -1 + [J_{c0} - J)/J_s] + \exp[-(J - J_{c0})/J_s] \tag{36}$$

Over the entire temperature of 7-70 K, we find that the ratio J_{c0}/J_s is 4-5 and almost constant.

Previous work has sought to determine the current density dependence of U_0. For example, Eq. ? differs from the result of Zeldov *et* al,[16] who deduced from transport measurements that $U(T,B,J) = U_J(T,B)\ln(J_{c0}/J)$. However, our experiments show when J is near to J_{c0}, U is exponentially dependent on J. Using the value of M_0 extrapolated

Figure 21

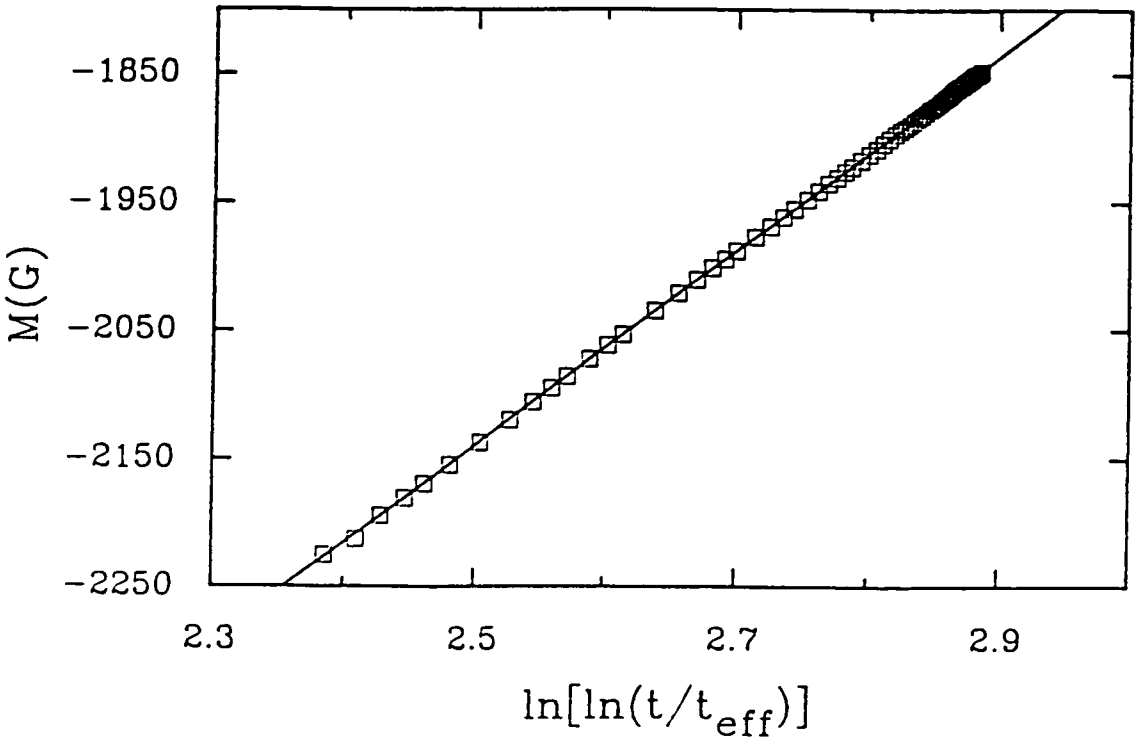

M vs $\ln[(\ln(t/t_{eff})]$, where t_{eff} is an adjustable parameter. Solid line shows a regression to Eq. (34) of text.

from Eq. (34), J_{c0} should be near 2.3 x 10^7 A/cm^2 at T = 30 K. In the present study, measurements were made with the sample reasonably close to the critical state, due to its magnetic field history; on the other hand, the relative current density J was typically much smaller in the transport study.[13] This difference in experimental regimes may account for the different experimental dependencies deduced for U(J).

The precise nature of the relaxation mechanism remains unclear. Since the long-term flux creep data are described very well by either Eq. (32) or (34), we are unable to conclude at this point whether the vortex glass model or the BLW theory is more appropriate. One may further test these models by checking their applicability to other non-equilibrium properties, such as the scaling behavior of the flux pinning[46] for instance. However, we address this issue by combining long-term flux creep experiments with studies of the influence of field sweep rate on magnetization curves. These are discussed in next two sections.

IV.2 Effects of Field-Sweep Rate on the Magnetization of Melt-Textured $YBa_2Cu_3O_{7-\delta}$

Though tremendous work has been done to understand the peculiar phenomenon of giant flux creep;[47,48] many aspects of the experiments and interpretation remain highly controversial.[47] Recent discussions on the time scale t_{eff}, for instance, attract

special attention. Here t_{eff} is an effective attempt time for a vortex bundle to jump over a potential barrier; it acts as a scaling quantity in the standard A-K[10,11] expression for Thermally Assisted Flux Creep (TAFC):

$$J(t) = J_{c0}[1 - \frac{k_B T}{U_0} \ln(\frac{t}{t_{eff}} + 1)] \tag{37}$$

In previous work, t_{eff} was considered a microscopic time scale of order 10^{-10} s.[10,49] Recent studies argue that t_{eff} is a macroscopic quantity related to the flux flow resistivity and sample geometry.[45] On the other hand, to our knowledge, most experimental efforts to obtain values for t_{eff} still have not been successful. In part, the difficulty lies in the fact that, if $t >> t_{eff}$ which the condition usually met in flux creep measurements, then the above equation reduces to the form

$$J(t) = J'_{c0} - C\ln(t) \tag{38}$$

where $C = J_{c0} kT/U_0$ and $J_{c0} = J_{c0} - C\ln(t_{eff})$. Since the accessible quantities in experiments are C and J'_{c0}, then J_{c0}, U_0, and t_{eff} cannot be separated. To clearly measure values for J_{c0}, U_0 and t_{eff}, we need to investigate the initial stage of magnetic relaxation, which poses another difficulty: how can one define the time origin of flux creep? In this work, we propose a way to determine these quantities by studying the effects of field sweep rate on the magnetization.

The influence of the field sweep rate on magnetization curves has been studied by several authors.[50,51] Pust *et al.*[50] first observed in measurements of hysteresis loops M(H) that M increased with field sweep rate. They attributed this phenomenon to

a competition between field sweep rate and magnetic relaxation and found that M increased with sweep speed as $M \sim Cln(K)$, where $K=\partial H/\partial t$. The same result was found by Griessen,[19] who first indicated a method to calculate the time origin for magnetic relaxation from a subcritical state. Very recently, in investigating the initial stages of flux creep in HTSC materials, Gurevich *et al.*[51] obtained the same relation between M and $ln(K)$ by more strict theoretical considerations. In addition, they concluded that the value of t_{eff} may depend on the initial experimental conditions and found that with a low sweep rate, e.g. $5x10^{-6}$ T/s, then t_{eff} may be as large as $5x10^{3}$ s. However, in the present paper, we consider t_{eff} to be independent of sweep rate and report an alternative way of studying the competition between sweep rate and relaxation in measurements of magnetic hysteresis loops $M(H)$ and flux creep $M(t)$. The theory is based on Bean critical state model[28] and the TAFC model. To first order, our results reproduce the $M \sim ln(K)$ relation, but additionally provide a way to determine t_{eff}. Furthermore, the time origin in flux creep measurements is well defined in this model. The largest possible magnetization, produced for rates $K \geq K_{max}$, provides information on J_{c0}. Experiments on a melt-textured-growth sample of $Y_1Ba_2Cu_3O_{7-\delta}$ agreed well with the model.

IV.2.1 Theoretical Model

Consider a type II superconductor subjected to the magnetic field that increases with time. According to the Bean model, for $H>H_{c1}$, the lower critical field, an

induced current density J_c flows around the sample perimeter such as to exclude the external field. Meanwhile, magnetic relaxation occurs due to the Lorentz driving force and thermally activated flux motion, thereby reducing the induced current. In this scenario, the field configuration changes instantly to follow the rising field. Figure 22 shows schematically the evolution of the local flux density *h(r,t)* in a cylindrical sample with radius *a*. Here we neglect the influence of H_{c1} and any variation of critical current density with local field in the sample, since the sample radius is small. Considering first a case in which the applied field *H(t)* is small, then Figure 22 (a) shows the corresponding *h(r)*. Its slope is proportional to the current density according to $\nabla \times h = J$. Let us suppose that the field is applied step by step at times t_0, t_1, ··· with time intervals $\Delta t \sim t_{eff}$ and with equal field steps ΔH. It is easy to see that for a small field, the field distribution corresponds almost exclusively to the current density J_{c0}; in other words, the influence of current decay is not so important. Figure 22 (b) graphically defines a field *H'*; for applied fields $H > H'$, the internal gradient is non-linear, since part of the internal field corresponds to now decayed current density that was induced at earlier times. Using Figure 22 (a) and 22 (b), we find for *H'*

$$H/J(t) = H'(t + \Delta t)/J_{c0} \tag{39}$$

or

$$H' = J_{c0}(\partial H/\partial t)/(\partial J/\partial t) \tag{40}$$

We can estimate the magnitude of *H'*. Using the A-K time dependence, we have $\partial J/\partial t = J_{c0}(k_B T/U_0)(1/t_{eff}) \sim C/t_{eff}$; then assuming typical values $J_{c0}/C \sim 20$,

Figure 22

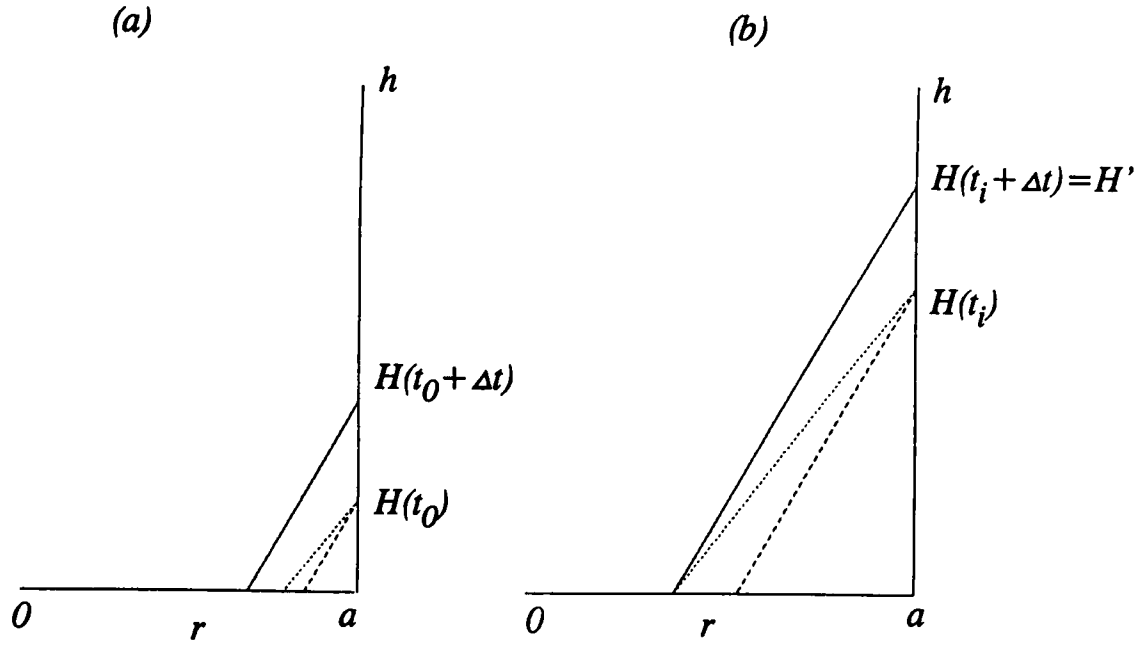

Field configurations. (a) For small field, the slope, $\partial H/\partial r$, corresponds to the critical current density J_c. The solid line represents the internal field $h(r,t_0+\Delta t)$ induced by the external field H applied at $t=t_0+\Delta t$; the dashed line is $h(r,t_0)$ induced by H applied at $t=t_0$. The dotted line describes the relaxation of $h(r,t_0)$ that would occur at $t_0+\Delta t$, if the field were kept at constant value of $H(t_0)$. (b) When H is stepped to value of $H'=J_{c0}(\partial H/\partial t)/(\partial J/\partial t)$ at $t=t_i+\Delta t$, the corresponding solid line of $h(r,t_i+\Delta t)$ just meets the dotted line of the relaxed field originally induced at t_i.

$\partial H/\partial t \sim 100$G/s, and $t_{eff} \sim 10^{-2}$ s, we obtain $H' \sim 20$ G. This is comparable to H_{c1}. Thus, generally speaking, H' is relatively small. For $H > H'$, the magnetic moment observed at time t can be calculated using Figure 23 to be the following (per unit length along the cylindrical axis):

$$\begin{aligned} m(t) &= \frac{1}{2}\int r \times J d^3 r \\ &= \pi\left[\int_{r_1}^{r_2} J(t,t_1) r^2 dr + \int_{r_2}^{r_3} J(t,t_2) r^2 dr + \cdots + \int_{r_n}^{r_{n+1}} J(t,t_n) r^2 dr + \cdots\right] \\ &= \frac{\pi}{3}\sum_{i=1} \left[J(t,t_i)(r_{i+1}^3 - r_i^3) + J(t,t_H)(a^3 - r_H^3)\right] \end{aligned} \tag{41}$$

Here $J(t,t')$ is defined as the current density induced at time $t' \leq t$ and observed at an arbitrary time t. The time t_H is the time at which the field reaches its "final" value. In a swept field experiment to measure magnetization loops, it is the time at which m(H) is measured and so $t = t_H$; in a magnetic relaxation study, t_H is the time at which the application of H is completed, so we have $t \geq t_H$. Transforming to a situation in which the field continuously changes, we replace the summation by an integration:

$$m(t) = \frac{\pi}{3}\int_0^{t_H} J(t,t') \frac{\partial}{\partial t'} r^3(t,t') dt' \tag{42}$$

with

$$r(t,t_H) \equiv a$$

The quantity $r(t,t')$ is given by the relation (see inset of Figure 23):

Figure 23

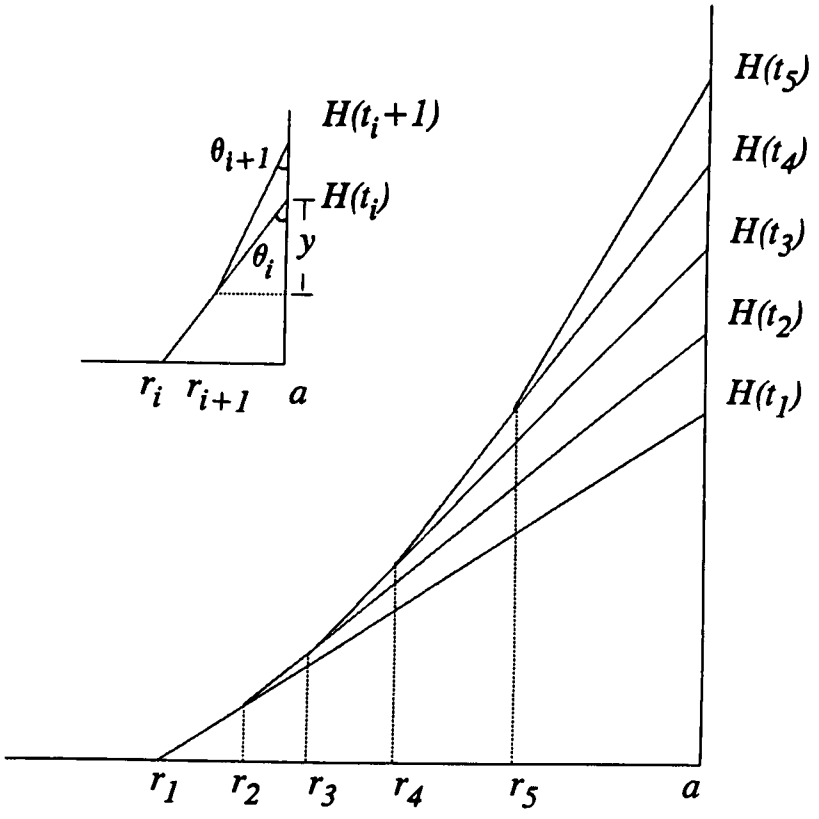

The distribution of $h(r,t_5)$ induced by external field H applied step by step at t_1, t_2, ···,t_5 with equal step size ΔH and equal interval $\Delta t=t_{i+1}-t_i$. r_i represents the radius at which the fields originally induced at t_i and t_{i+1} have the same value at time t_5. Inset: The construction used to calculate r_i.

$$\begin{cases} \dfrac{a-r_{i+1}}{y} = \tan\theta_i \\ \dfrac{a-r_{i+1}}{y+\delta H} = \tan\theta_{i+1} \end{cases} \tag{43}$$

Noting $cot\theta = -J(t,t')$, we obtain that

$$r(t,t') = (a + \frac{\partial H/\partial t'}{\partial J(tt')/\partial t'}) S(a + \frac{\partial H/\partial t'}{\partial J(t,t')/\partial t'}) \tag{44}$$

where the step function $S(x)$ avoids a negative r. In practice, the correct procedure is first to find t^*, the last time at which $r(t,t^*)=0$. The integration in Eq. (42) then starts from t^*. Eqs. (42) and (44) form the basis for our model. We use these expressions to determine the moment m in cases when (1) the field is swept continuously and (2) when the field is latched at a fixed value for a magnetic relaxation (flux creep) experiment.

A. Field changing with constant sweep rate.

First we consider the case where H rises at a constant rate K. This is the usual situation in measurements performed in a Vibrating Sample Magnetometer (VSM). We assume that the field has already penetrated to the center of the sample. Using Eq. (42), the magnetic moment is given by Eq. (45):

$$m(t) = \frac{\pi}{3}[J(t,t)a^3 - \int_{t^*}^{t} r^3(t,t')\frac{\partial}{\partial t'}J(t,t')dt'] \\ = \frac{\pi a^3}{3}[J(t,t^*) - \frac{3K}{a}(t-t^*) - \frac{3K^2}{a^2}\int_{t^*}^{t}(\partial J/\partial t')^{-1}dt' - \frac{K^3}{a^3}\int_{t^*}^{t}(\partial J/\partial t')^{-2}dt'] \quad (45)$$

In order to make an explicit calculation, we need to know $J(t,t')$. Several different models for the relaxation of currents in HTSC materials have been proposed;[14,45,52] for now, we use the straightforward A-K relation. This not only simplifies the calculations but it also is the asymptotic form of the other models, when $t-t^*$ is close to t_{eff}, which is the time domain of interest here. From Eq. (37), we have for $J(t,t')$

$$J(t,t') = -[J_{c0} - C\ln(\frac{t-t'}{t_{eff}}+1)] \quad (46)$$

and its derivative

$$\frac{\partial J}{\partial t'} = \frac{-C}{t-t'+t_{eff}} + \alpha K \quad (47)$$

Here $K=\partial H/\partial t'$ is the field sweep rate and $\alpha=\partial J/\partial H$. We will neglect the t' dependence of α (α is an implicit function of t' through H) for simplification. Substituting Eq. (47) into Eq. (44), we find for t^*, the root of $r(t,t^*)=0$:

$$t-t^* = \frac{aC/K}{1+a\alpha} - t_{eff} \quad (48)$$

Substituting this expression for $(t-t^*)$ into Eq. (45) and retaining the first two (largest) terms, we obtain the following result for $m(t)$:

$$m(t) = \frac{\pi a^3}{3}\left(constant - ClnK + \frac{3t_{eff}}{a}K + \cdots\right) \tag{49}$$

where the constant term is

$$constant = -J_{c0} + Cln\frac{aC}{t_{eff}(1+a\alpha)} - \frac{3C}{1+a\alpha} \tag{50}$$

From Eq. (49) we see that the magnitude of m increases with lnK to first order, which agrees with the earlier work.[50,19,51]. There is, however, an additional term that is proportional to K. Measuring the coefficient of this linear term, $3t_{eff}/a$, provides a means of determining the important quantity t_{eff}. Since the relaxation rate C is of order $10^{-2}J_{c0}$, and t_{eff}, whose magnitude is rather controversial, may be quite small, the effect from this term may be observed only for high sweep rates K. As a generality, note that this model does not necessarily assume that $\partial J/\partial H = 0$.[50]

Another important feature is related to the time t^*. In particular, the model provides relation Eq. (49) only if K is less than a certain value, K_{max}, which is the solution of Eq. (48) when $t\text{-}t^* = 0$:

$$K_{max} = \frac{aC}{(1+a\alpha)t_{eff}} \tag{51}$$

The physical explanation is when $K > K_{max}$, the relaxation of shielding current is relatively slow compared with the redistribution of internal field produced by the changing external field. Then the field gradient is just J_{c0}, which gives the largest

moment. Eq. (51) shows that this condition can be met most easily if the radius a is small.

B. Time origin in flux creep measurements

In flux creep measurements, a sample is first cooled to a certain temperature in zero field (ZFC), then the field is applied at a constant sweep rate so that it approaches a target value, either from lower or from higher fields. The measurements commence after H stops at the desired value at time t_H. The same calculations apply in this case, except that now we have $t \geq t_H$. This gives:

$$\begin{aligned} m(t) &= \frac{\pi a^3}{3}[J(t,t^*) - \frac{3K}{a}(t_H - t^*) + \cdots] \\ &= \frac{\pi a^3}{3}[-\tilde{J}_{c0} + C\ln(\frac{t-t^*}{t_{eff}} + 1) + \cdots] \end{aligned} \tag{52}$$

where

$$\tilde{J}_{c0} = J_{c0} + \frac{3K}{a}(t_H - t^*) \tag{53}$$

Therefore the time origin in flux creep measurements is not t_H but rather t^*. According to Eq. (48), we have:

$$\Delta t = t_H - t^* = \frac{aC/K}{1 + a\alpha} - (t - t_H) - t_{eff} \tag{54}$$

For example: Immediately after application of the external field when $t = t_H$, we have $\Delta t \sim 10$ s, assuming that $a \sim 0.1$ cm, $K \sim 100$ G/s, $\alpha \sim 100\, AG^{-1}cm^{-2}$, and $C \sim 10^5\, Acm^{-2}$.

This is not a short time, and so significant magnetic relaxation takes place without being observed. Alternatively, we see from Eq. (54) that $\Delta t=0$ when $t-t_H \approx aC/K(1+a\alpha)$. So if we neglect relaxation from t_H to $t=\Delta t$, then t_H behaves as a true time origin. This agrees with the approach of Griessen[19] and A. Gurevich *et al*[51]. Actually both of them independently derived expressions similar to Eq. (48). However, Gurevich defined Δt as t_{eff} and interpreted it as the time interval needed to begin steady magnetic relaxation, following the abrupt change of external field at $t=t_H$. As showed clearly in the above discussion, our view of Δt is that, with any finite field sweep rate, flux creep starts before the field reaches the desired value. This means the flux creep measurements generally start from subcritical state unless the field sweep rate is higher than K_{max}. This interpretation is the same as that of Griessen.[19]

To facilitate comparison with experimental results, it is worth rewriting Eq. (49) in practical units (cm, Gauss and A/cm^2). Then the factor $(1+a\alpha)$ in the above equations is changed to $(0.79+a\alpha)$, where the numerical factor 0.79 is just $(4\pi/c)^{-1}$ with c corresponding to 10 in practical units. For the magnetization M, we have

$$M(t) = \frac{a \cdot constant}{30} - \frac{a \cdot C}{30} lnK + \frac{t_{eff}}{10} K + \cdots \qquad (55)$$

Recalling the Bean formula $M=aJ_c/30$ shows that the coefficient of $ln(K)$ is just the flux creep rate $dM/dln(t)$ in magnetic relaxation measurements.

IV.2.2 Experiments

A melt-textured-growth sample of $YBa_2Cu_3O_7$ with mass of 0.0747 g and approximate dimensions 0.21x0.30x0.20 cm3 (sample 2, see II.1) was used in the experiments. The larger mass of this sample gives relatively larger signals improving the signal-to-noise ratio. Prior measurements of the DC magnetization were made using a commercial SQUID magnetometer (Quantum Design MPMS). For example, an analysis with the Bean model yielded J_c values at H=1 Tesla of $2.5x10^5$ A/cm^2 and $3.4x10^4$ A/cm^2 for T=25 K and 60 K, respectively. Experiments to test the effects of field sweep rate on magnetization were performed in a laboratory-constructed VSM. Hysteresis loops M(H) with various sweep rates were recorded at temperatures of 27, 28, and 60 K in fields up to H=3.4, 5.0 and 3.7 T, respectively. Figure 24, a plot of magnetic moment *m(H)* at 60 K, illustrates the impact of field sweep rate. Measurements at progressively slower rates, shown as the set of line segments in the range 2.9-3.5 T, yielded ever smaller values for the magnetic moment *m*. To examine the explicit rate dependence, we consider magnetization M versus rate K at fixed temperature and fixed field. Figure 25 (a) presents the results at T=28 K, H=4.8 T; similar results at 60 K, 3.2 T are shown in Figure 26 (a). In these two experiments, the sweep rate ranged from 20 G/s to 250 G/s. Figure 27 shows additional results at 27 K in a field of 3.2 T. In this case, we were able to employ an expanded interval of 5 G/s to 800 G/s. These three cases are denoted as M(K; T=28K), M(K; T=60K) and M(K; T=27K) respectively.

Figure 24

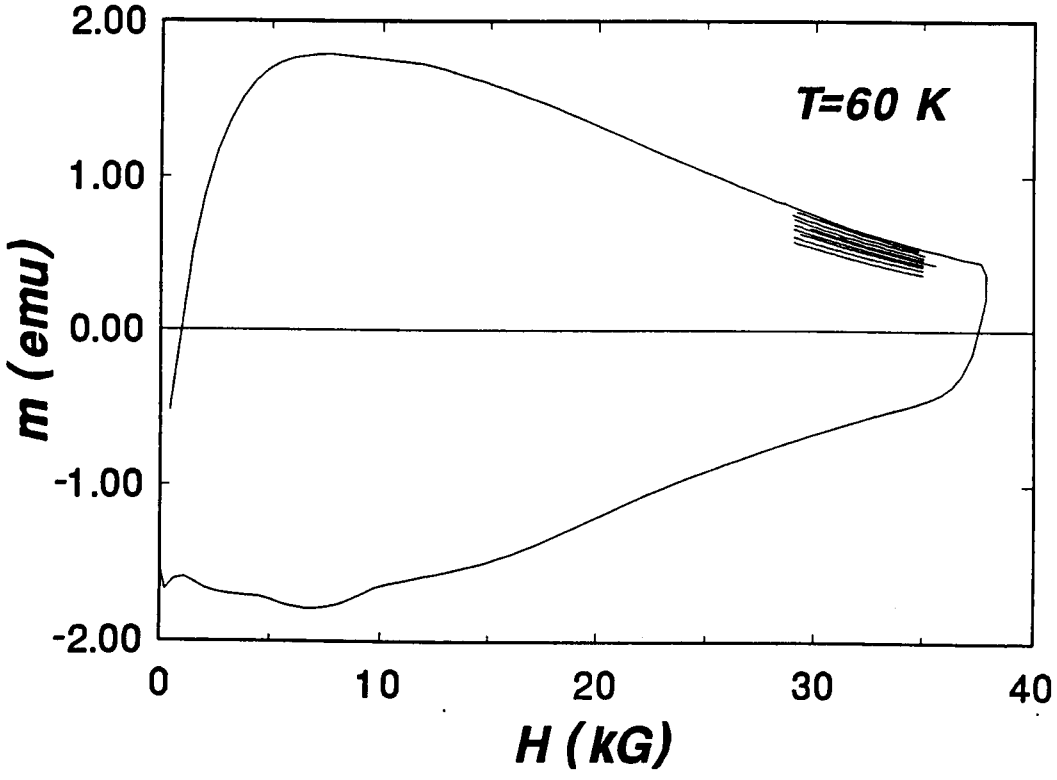

At T=60 K, the magnetic moment m versus field H for different field sweep rates K. The complete loop was measured at the highest rate, K=250 G/s. Measurements at other rates, 200 G/s, 170 G/s, 128 G/s, 96 G/s, 75 G/s, 53 G/s, 42 G/s, 31 G/s, and 21 G/s, are shown for fields in the range from 2.9 to 3.5 T.

Figure 25

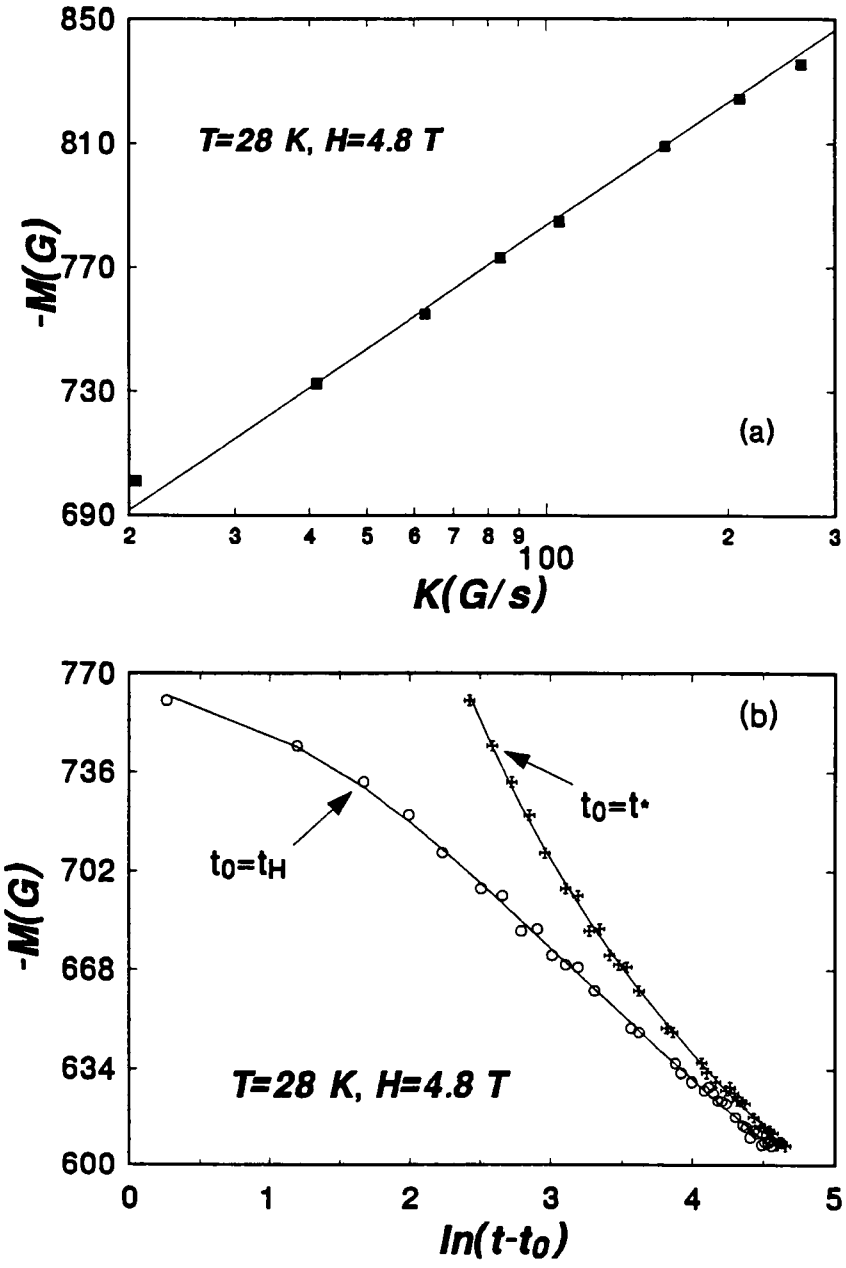

(a) Magnetization M, (expressed in units of [emu/cm^3]=[G-cm^3]/cm^3=G), versus sweep field rate K, for T=28 K and H=4.8 T. (b) time dependent M versus $ln(t\text{-}t_o)$ with time origin t_o defined as either t_H or t^*, where the units of time are seconds.

Figure 26

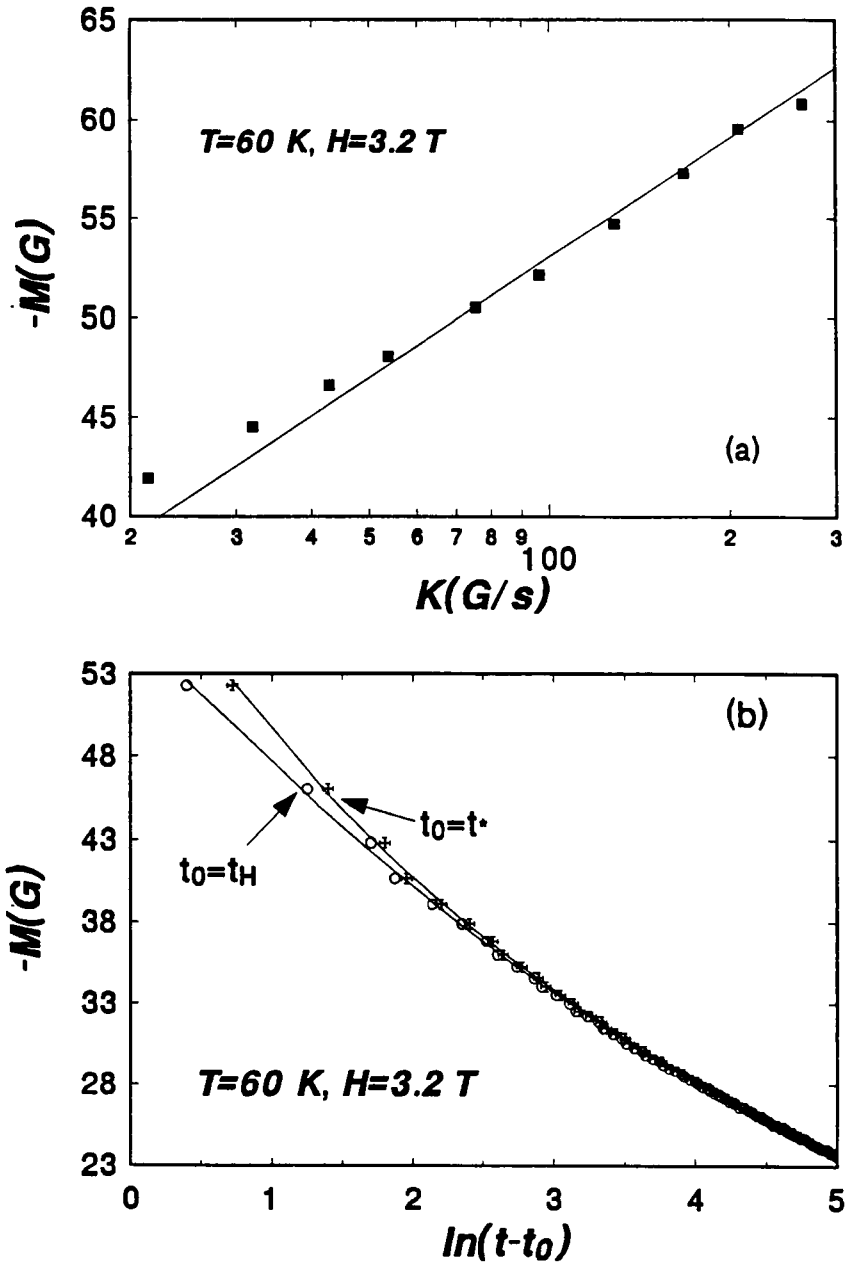

The same quantities as those in Figure 25, but with T=60 K and H=3.2 T.

Figure 27

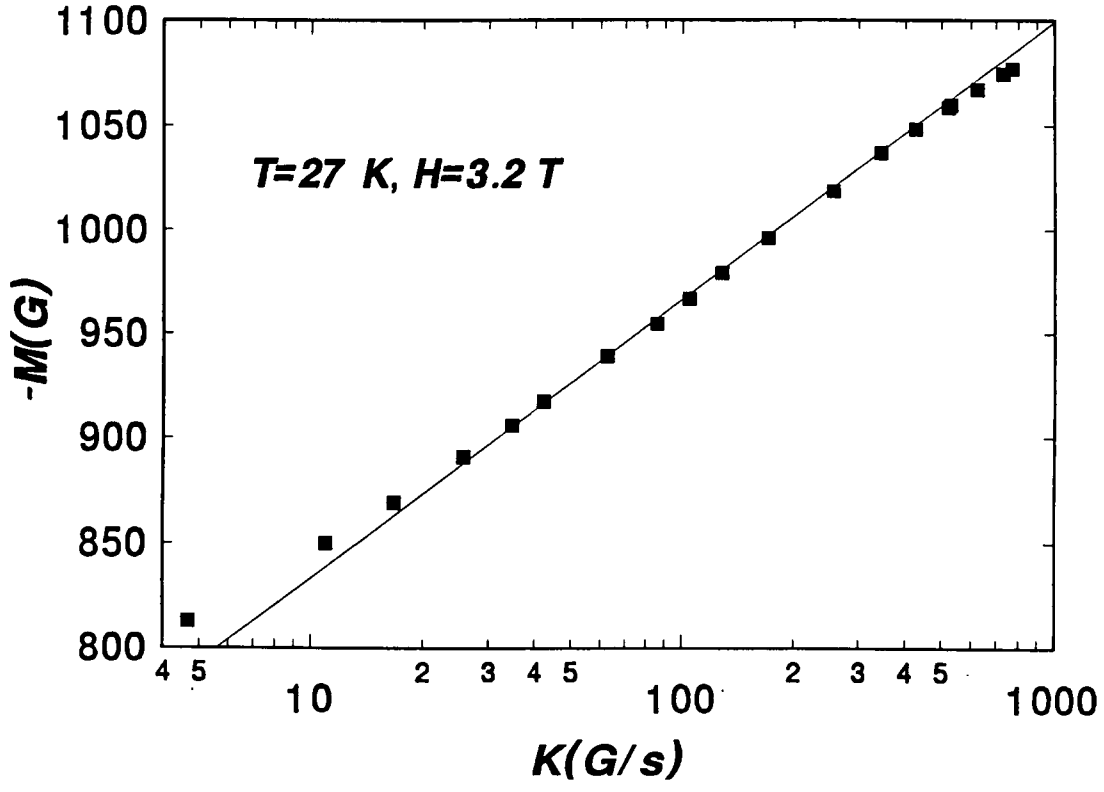

Magnetization M versus sweep rate K at T=27 K and H=3.2 T. Note particularly the departure from linearity at very high sweep rates.

To compare the quantities *dM/dln(K)* and *dM/dln(t)* experimentally, short magnetic relaxation measurements were made at the same temperatures and fields (28 K, 4.8 T and 60 K, 3.2 T), using the VSM. These time dependent measurements of M(t) are shown in Figure 25 (b) and Figure 26 (b), and are denoted as M(t; T=28K) and M(t; T=60K). The magnetic field was applied at rates of 150 G/s and 260 G/s, respectively.

In all the sweep rate studies, an approximately logarithmic dependence of M on the rate K was observed, as given by Eq. (49). Careful examination of Figure 25 (a), Figure 26 (a) and Figure 27 reveals, however, slight deviations from a strictly logarithmic relation at both high K and low K sweep rates. In the low K region, the departure from linearity (on the semilogarithmic plot) comes from the fact that the A-K expression, Eq. (37), is only approximately correct for high-T_c superconductors, as we discussed in the previous section. With still slower sweep rates, the deviation would be even more severe. The central interest in this work, however, in the high K region: Here the decreasing slope of the curves is a consequence of the linear term in K in Eq. (55). We can assess the importance of the correction term by considering the ratio of its size relative to the logarithmic term, $3Kt_{eff}/(aCln(K))$. Assuming that t_{eff} is ~ 0.1 s, $aC/30 \sim 60$ and that $K=150$ G/s, the ratio is about 10^{-3} for M(K; T=28K). Under these conditions, the effect of the linear K term is rather small. For M(K; T=60K), however, the ratio may be $\sim 10^{-2}$, due to the smaller value of $aC/30$. Even larger ratios might develop, if t_{eff} increased at higher temperatures (see discussion in IV. 4). Unfortunately, long-term fluctuations in sample temperature were larger in this case ($\Delta T \sim 0.2$ K for

M(K; T=60K), compared with ~0.05 K for M(K; T=28K)). Consequently, it was difficult to analyze the linear correction very accurately. By compensating for the temperature variations, we found that t_{eff} was the order of 10^{-1} s for both cases.

In order to obtain more accurate and reliable results for t_{eff}, some experimental modifications were made to improve the temperature stability, as we discussed in II.6. Furthermore, the magnet power supply was replaced with a unit (Lake Shore Superconducting Magnet Power Supply model 612) providing higher charging voltages (up to 30 V) and higher output power (up to 10^3 VA). Sweep rates from ~5 G/s to 800 G/s were obtained. These measurements yielded much smoother and higher resolution data, as seen in Figure 27. Consequently the flattening in both the high K and low K regions is much more evident. Analysis of the data at high sweep rates yielded the value $t_{eff} = 0.24 \pm 0.03$ s. This result agrees with predictions in the literature[45] and with our early results.[53]

Next we consider effects associated with the time origin in a flux creep experiment. Since the magnetic relaxation is a non-linear function of t, the proper definition of the time origin is essential for studying the initial stages of magnetic relaxation. This is clearly demonstrated in Figure 25 (b) and Figure 26 (b), where M is plotted versus $ln(t-t_o)$, using either t_H and t^* as the time origin t_o. The figures show time dependent magnetization results M(t; T=28K) and M(t; T=60K), respectively. Comparison of Figure 25 (b) and Figure 26 (b) indicates that t_H is *not* the correct time

origin, since the two curves appear quite different while one should expect more uniformity in the results. The origin of this difference can be explained as follows: At high temperature, the magnetic relaxation rate is smaller, which causes $t_H - t^*$ to be small. In other words, the field application resembles more closely a step function. According to Eq. (54), the time offset ($t_H - t^*$) is only ~ 0.56 s for M(t; T=60K); in contrast, it is ~ 10 s for M(t; T=28K). Therefore at 28 K, much relaxation had already taken place when the measurements commenced; by comparison, the measurements of M(t) at 60 K effectively commenced much earlier, allowing us to see the giant magnetic relaxation at short times. If instead we use calculated values of t^* for the time origin t_o, then both the relaxation curves at 28 and 60 K have similar functional dependencies *M(t)*. The results are described very well by the theoretical power law "interpolation formula"[14] $M = M_{c0}/[1+(\mu k_B T/U)\ln(t/t_{eff}+1)]^{1/\mu}$ as well as our empirical double-logarithmic formula: $M = M_0 + C' \ln[\ln(t/t_{eff}+1)]$. These expressions have been shown to provide a precise description of *M(t)* in long-term magnetic relaxation studies discussed in the previous section.

Incorporating t^* as the time origin, we can then compare values of *dM/dln(K)* and *dM/dln(t)*. The relationship between these quantities was treated theoretically[50] in 1989, but there have been no experimental studies of this feature, to our knowledge. For a meaningful comparison, we must choose an appropriate time window to obtain an average value of *dM/dln(t)*, since *M* is not a precisely linear function of *ln(t)*. The appropriate time t for evaluating the logarithmic time derivative is given by Eq. (48),

which depends on the rates of flux creep and field sweep. Measured from t_H, the appropriate average is taken after 80 s for M(t; T=28K) and after 7 s for M(t; T=60K). The resulting values of *dM/dln(t)* are 66 G and 9.1 G, respectively. These results compare very favorably with the respective average slopes *dM/dln(K)*, which are 62 G and 7.9 G. The respective values differ by $\sim 3\%$ and $\sim 13\%$. The larger discrepancy in the latter case may be due in part to the limited time resolution (~ 1.5 s) in the time dependent study. Overall, we judge the agreement to be quite acceptable.

To conclude this section, the effects of magnetic field sweep rate on magnetization measurements in high temperature superconductors have been studied, using the Bean critical state model and TAFC model. To first order, a logarithmic dependence of magnetization M on field sweep rate K is found, with a slope *dM/dln(K)* equals to the flux creep rate *dM/dln(t)*. A linear correction term to the *ln(K)* dependence allows the time scale t_{eff} to be determined experimentally at high sweep rates. At very low sweep rates, there are deviations from a strictly logarithmic K-dependence arising from inadequacies in the A-K model. Further work discussed in the next section analyzes this problem using more recent and realistic theoretical models for flux motion in high-T_c superconductors.

IV.3 Strong Evidence for Vortex−Glass/Collective Pinning Theory

In this section, we analyze the magnetization relaxation studies on the melt textured-growth sample of $Y_1Ba_2Cu_3O_{7-\delta}$ (sample 2) to test several theoretical models, by seeing which of them best describes the relaxation of supercurrents in this high-T_c superconductor.

Much work and intensive study have been devoted to studying the motion of magnetic vortex lines in HTSC, yielding several competing models for detailed description of magnetic relaxation, whose physical origin is the decay in time of induced "persistent" supercurrents. As mentioned previously, the vortex glass theory[14] predicts that random pinning forces from impurities induce a phase transition from a vortex fluid phase into a vortex glass phase, in which the vortices are frozen into some disordered pattern. In the vortex glass state, vortices are not movable (in the limit of zero current density, J→0); therefore there is a true resistance−free state at finite temperatures. Collective pinning theory[15,17,45] gives a similar picture; in particular, the two theories give the same power law form for the dependence of activation energy U on current density J. However, experimental evidence did not particularly favor these theories until Bishop *et al.*[54] recently reported direct measurements of I−V characteristics of thin YBaCuO films using a SQUID picovoltmeter system. With improved voltage sensitivities of 10^{-10} V, the experimental window was expanded considerably. Their

results strongly supported the vortex glass/collective pinning (VG/CP) model. On the other hand, the situation in direct flux creep studies of magnetization M(t) versus time is still far from clear. It seems that a variety of models[55,56,57] (also see VI.1) are able to fit to data with comparable efficiency. The reason for this confusing situation has become clear: the time window of observations is too short in most studies of flux creep. Over a short time scale, most models function as a first order correction to the conventional A−K model and are adequate for fitting the data.

Here we combine information from studies of (1) the effects of magnetic field sweep rate on magnetization in hysteresis loop measurements and (2) flux creep experiments to expand the measurement window up to six decades of effective time. This strict test shows that, among the various models tested, only VG/CP theory provides an excellent and consistent description of magnetic relaxation in this HTSC material.

IV.3.1 Principles

In flux creep measurements, the average magnetization M is recorded as a function of time t, which provides information on magnetic relaxation, i.e., the decay of induced, circulating supercurrents. As we saw in the last two sections, in typical flux creep studies, the data extend over only ~2 decades of time and commence with a starting point that is often ~100 s or longer after the time t_H at which the field reaches the desired value. This delay is due to the time required for a measurement by

commercial SQUID magnetometers. Generally, the subsequent decay of magnetization over this limited time window is only a few percent (tens of percent) of M_0 at low (high) temperatures, where M_0 is the largest magnetization observed. To expand the time window, one can either prolong the measurements or reduce the time interval between t_H and the first point of measurement. The former approach is difficult since the magnetic relaxation obeys a logarithmic relation to first order, with $M(t) \sim \ln(t)$. Therefore, during the following years, M and current density J may decay by only a small amount. Alternatively, more immediate measurements are possible with a Vibrating Sample Magnetometer (VSM) or Hall Effect device[56], for instance. However, there is another serious difficulty in studying the early stages of flux creep: how to define the time origin of magnetic relaxation? As we have discussed in the previous section, if the field sweep rate is finite, then magnetic decay commences before the field reaches its desired value. In other words, t_H is not the correct origin of time. It was shown (section IV.2) that shifting the time origin by a few seconds for flux creep M(t) data with $t > 100$ s affects the analysis only slightly; in contrast, the relation between M and t in the early stage is very sensitive to such a time shift. Consequently, a correct definition of the time origin is essential, but also difficult, for it depends on the specific flux creep model. Furthermore, it is inherently very difficult when analyzing only M vs. t data to determine separately all of the important quantities that occur in flux creep models. These include U_0, J_{c0}, and t_{eff}. However, as we discussed in IV.2, one can study the dependence of the magnetization M(H,T) on field sweep rate in hysteresis loop

measurements to investigate the magnetic decay in its very early stage. The main result is concluded in Eqs. (42) and (44). We rewrite them as the following:

$$m(t_H) = \frac{\pi}{3}\int_0^{t_H} J(t_H, t')\frac{\partial}{\partial t'} r^3(t_H, t')dt' \qquad (56)$$

with

$$r(t,t) \equiv a$$

where a is the radius of a cylindrical sample and $J(t, t')$ is the critical current density at time t that was induced at $t' \leq t$. The $r(t, t')$ is determined by the following:

$$r(t,t') = (a + \frac{\partial H/\partial t'}{\partial J(tt')/\partial t'})S(a + \frac{\partial H/\partial t'}{\partial J(t,t')/\partial t'}) \qquad (57)$$

where the step function $S(x)$ avoids a negative r. In practice, the integration starts from t^*, instead of 0, where t^* is the root of $r(t, t')=0$. Usually, the field H varies with constant sweep rate $K=\partial H/\partial t$. To use these expressions and actually perform a calculation, one requires explicit knowledge of $J(t, t')$, or $U(J)$. Here, we consider five different models for flux creep: (1) the traditional A−K model, which assumes a linear dependence for the pinning barrier on J, leading to a logarithmic relation with $M \sim ln(t)$. (2) the VG/CP model providing $U \propto J^{-1/\mu}$. (3) a Power−Law (PL) model[16] giving $M(t) \sim t^{\alpha}$ that is associated with a potential barrier having a logarithmic dependence on current. (4) Griessen's model,[19] which provides that $U \propto (1-J/J_{c0})^n$. (5) a Double Logarithmic (DL) model (see IV.1), which comes from an empirical formula $M(t) \propto ln[1+ln(t/t_{eff}+1)]$ used for fitting flux creep data. *By comparing experiments with calculations via Eqs. (56) and (57), one can probe the magnetic*

relaxation and find which model agrees best with data in a time interval $\Delta t = t_H - t^*$, *where* t^* *behaves as a real time origin.* For high sweep rate K at high T, Δt can be as short as $\sim t_{eff}$, where t_{eff} is the effective hopping time for a bundle of vortices. Then combining this information with an analysis of flux creep (FC) measurements M(t), we can expand the effective time window to be much longer and simultaneously avoid problems associated with defining the zero of time. If a given model is correct, then the parameters found from experiments on magnetization versus field sweep rate (MFSR) should be consistent with those from FC measurements. *To require consistent values for the experimental parameters for both experiments imposes a stringent test on the theoretical models.*

IV.3.2 Results and analysis.

Experiments were performed on the melt-textured-growth $Y_1Ba_2Cu_3O_{7-\delta}$ sample (sample 2). The FC measurements M(t) were made in the SQUID magnetometer while experiments of MFSR were performed in the VSM. To insure that both instruments have identical calibrations, a high quality, homogeneous Nb superconductor sphere was used as a standard magnetic moment. To maintain the same temperature for measurements in the two magnetometers, the VSM is equipped with a Si diode thermometer located about 0.5 cm above the sample with temperature obtained in H=0; the SQUID magnetometer was discussed previously. We expect the temperature difference to be

small (<0.5 K). Hence the absolute values of magnetization would be affected slightly by small temperature differences between instruments, but this should have little influence on parameters of the magnetic relaxation.

As we showed in IV.1, the magnetization M(t) in the long-term flux creep measurements followed a logarithmic time decay to lowest order. In fact, however, clear deviations from a ln(t) dependence were evident everywhere, particularly at high temperatures with high fields. For the MFSR measurements, we will use the measurements of T=27 K and H=3.2 T presented in IV.2, along with additional measurements at 49 K and 1.8 T. Similar results are observed in both cases: an approximately logarithmic dependence of M on sweep rate K was observed, as expected from the A−K model.[19,50,51] In analogy with the time dependent studies, corresponding deviations from a strictly logarithmic dependence on K are evident in both the low and high K regions. It is noteworthy that the flattening of the M(K) curve in the low K region (but not in the high K region) is consistent with recent calculations by Schnack *et al,*[35] who performed numerical and analytical calculations of the influence of flux creep on the shape and character of magnetic hysteresis loops M(H). The present analysis will show that for both the FC and MFSR experiments, all of the more recent models give a description that is decidedly superior to the A-K formulation. Individual results for the various models are discussed separately in the following. In analyzing the measurements, we relate $M \propto J$ using the Bean model, and note that M is negative in

sign for increasing field history. Also, the same notation of J_{c0}, t_{eff} and U_0/k_BT has been adapted in all models for quantities having similar meanings.

(1) VG/CP model.

Vortex glass-collective pinning theory provides a slightly modified "interpolation formula" (Eq. (31)) for the magnetic relaxation. We rewrite it here with explicit time origin t_0:

$$M(t) = \frac{-M_{c0}}{(1 + \frac{\mu k_B T}{U_0} \ln(\frac{t - t_0}{t_{eff}} + 1))^{1/\mu}} \tag{58}$$

From now on, we shorten this to just t for notational simplicity, but remember for MFSR experiments, t_0 is an important quantity. For $t >> t_{eff}$, the interpolation formula simplifies to the following:

$$M(t)^{-\mu} = M_0^{-\mu} + C(T)\ln(t) \tag{59}$$

with

$$(M')^{-\mu} = (M_{c0})^{-\mu} - C\ln(t_{eff})$$

$$C = (\mu k_B T / U_0) M_{c0}^{-\mu} \tag{61}$$

In fitting FC data to Eq. (59), we made the same type of analysis as that used for sample 1 in IV.1: the value of μ, a non−linear parameter, is adjusted to make plots of $M^{-\mu}$ vs. $ln(t)$ optimally linear. Values of $(M')^{-\mu}$ and C are then found from the intercept and the

slope of a linear regression line. To illustrate, Figure 28 shows an analysis of $M^{-\mu}$ *vs.* *ln(t)* that is precisely linear. The experiment was performed at T=27 K, H=3.2 T. So far, there are only two equations but three unknowns, meaning that we cannot separate M_{c0}, U_0 and t_{eff} at this point. On the other hand, numerical analysis of the MFSR measurements using Eqs. (56) and (57) allows us to freely vary μ, M_{c0}, t_{eff}, and U_0 to best fit the *M(K)* data. This provided the extremely good description shown in Figure 29 (a), where we used the measurements discussed in the previous section which refer to the same conditions, T=27 K, H=3.2 T. This time in the figure *M vs. K* was plotted on a semilog scale with the solid line represents the VG/CP theory. An extremely important feature of this analysis is that the parameters obtained in two independent experiments and analyses are nearly identical. The FC experiment gives for μ, M' and C the values 0.482, 0.03475, and 0.00115, compared with 0.483, 0.03475 and 0.00115 for the MFSR experiment, respectively. Eqs. (60) and (61), which relate M_{c0}, t_{eff}, $U_0 M'$, and C, have been used to get values for the same quantities in the two experiments. Clearly these results for different time domains are remarkably consistent. To facilitate comparisons, Table I lists parameter values for the FC and MFSR experiments, respectively, for all models under two different experimental conditions of temperature and field. In Figure 29 (b) is plotted the difference between calculated and experimental values of magnetization, δM, versus K, for each of the several models.

(2) PL model.

Figure 28

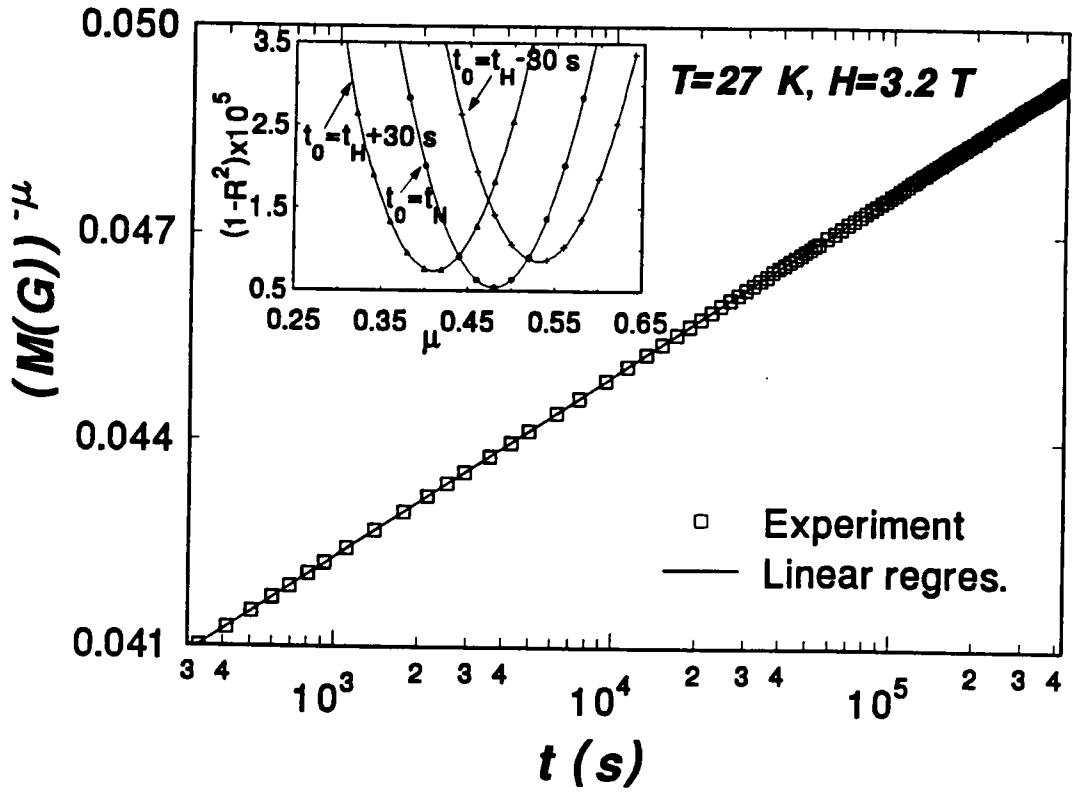

Analysis of flux creep study in $Y_1Ba_2Cu_3O_7$ at 27 K, H=3.2 T, using vortex glass/collective pinning (VG/CP) theory: time dependent $M(t)^{-\mu}$ versus log(t), with μ=0.482. Figure 30-Figure 32 show analyses of the same experimental data M(t), using various models. Inset shows optimization of nonlinear fit, by minimizing $(1-R^2)$, where R^2 is the goodness-of-fit. The three curves correspond to different definitions for t_0, the zero of the time base; see text.

Figure 29

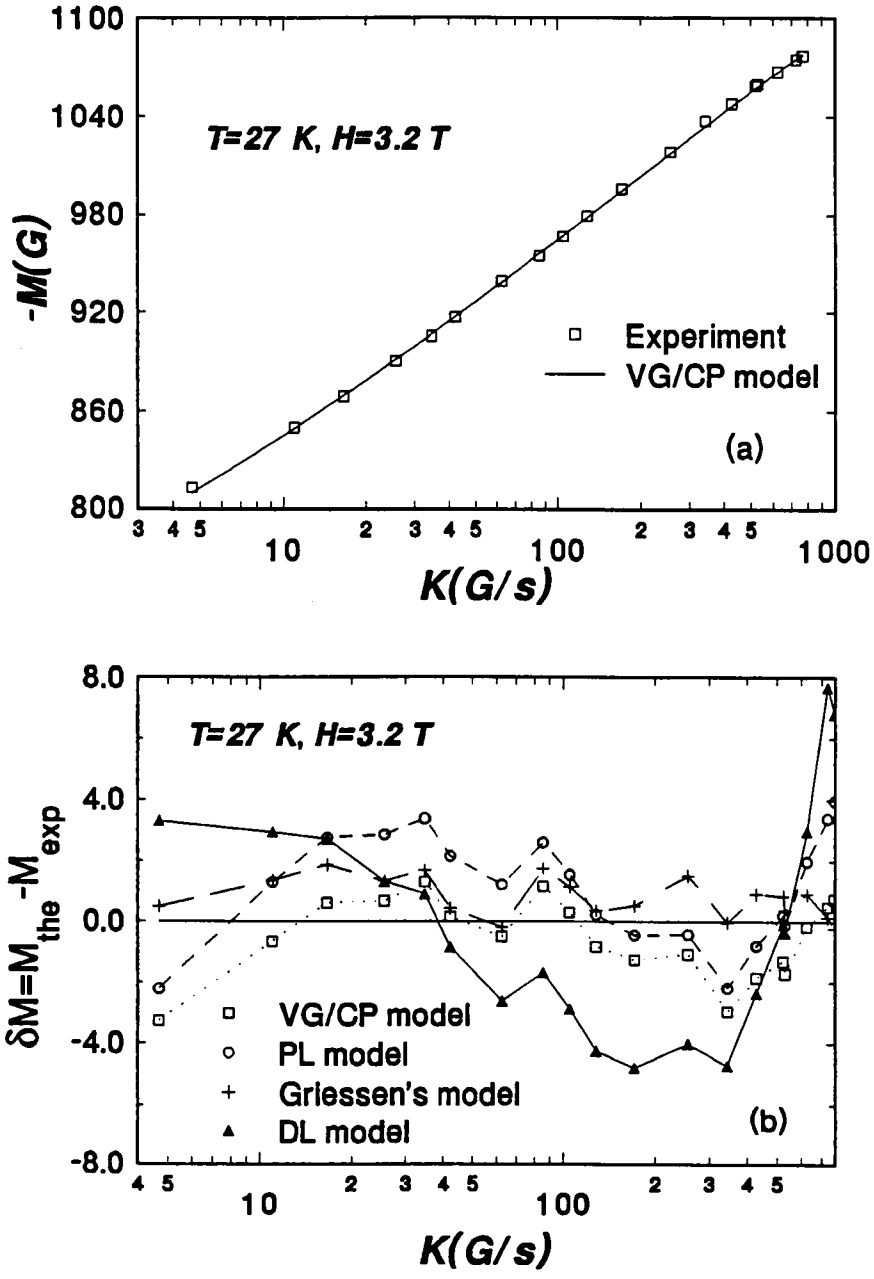

Analysis of magnetization versus field sweep rate (MFSR) data at T=27 K, H=3.2 T. (a) −M versus field sweep rate K, where the line is fitted to VG/CP theory. (b) Deviations between experimental and fitted theoretical values for magnetization, plotted versus K, for each of several theoretical and empirical models.

TABLE 1. MAGNETIC RELAXATION PARAMETERS FOR EACH MODEL ACQUIRED BY FITTING FC & MFSR EXPERIMENTS (with $H_{app} \| C$)

VG/CP Model				
	T=27 K, H=3.2 T		T=49 K, H=1.8 T	
	FC (R^2=0.999994)	MFSR (R^2=0.99971)	FC (R^2=0.999993)	MFSR (R^2=0.99947)
μ	0.482	0.483	0.273	0.273
M_{c0}(G)		1138		428
$(M')^{-\mu}$	0.03475	0.03475	0.204	0.198
C	0.00115	0.00115	0.0041	0.0042
PL Model				
	T=27 K, H=3.2 T		T=49 K, H=1.8 T	
	FC (R^2=0.999954)	MFSR (R^2=0.99931)	FC (R^2=0.99994)	MFSR (R^2=0.99937)
M_{c0}(G)		1204		439
U_0/k_BT	20.94	17.41	17.32	14.54
t_{eff}(s)	0.01	0.09	0.004	0.15
Griessen Model				
	T=27 K, H=3.2 T		T=49 K, H=1.8 T	
	FC (R^2=0.9983)	MFSR (R^2=0.99984)	FC (R^2=0.99962)	MFSR (R^2=0.99943)
β	2.16	1.51	2.13	1.35
M_{c0}(G)	1100	1094	460	429
U_0/k_BT	44.20	34.06	36.49	24.08
const.	1.9	4.3	4.0	4.6
DL Model				
	T=27 K, H=3.2 T		T=49 K, H=1.8 T	
	FC (R^2=0.999995)	MFSR (R^2=0.9980)	FC (R^2=0.999993)	MFSR (R^2=0.9906)
M_{c0}(G)	1607	2058	536	581
$\tilde{c}$	396	512	141	136
t_{eff}	0.122	0.002	0.082	0.027

This model[16] provides that $U(J) = U_0 ln(-J_{c0}/J)$, which corresponds to a power-law time dependence for M(t):

$$(-M/M_{c0})^{1-n} - 1 = t/t_{eff} \tag{62}$$

where $n = U_0/k_BT$. Since the first term on the left side of the equation is much larger than one, we rewrite it as

$$\ln(-M) = \frac{1}{1-n}[\ln(t) + \frac{\ln(M_{c0}^{1-n})}{t_{eff}}] \tag{63}$$

Following this expression, Figure 30 presents ln(−M) vs. ln(t), where $1/(1-n)$ and $ln(M_{c0}^{1-n}/t_{eff})/(1-n)$ are recognized as the slope and intercept of the linear regression line. To fit the complementary MFSR data by numerical calculations of Eqs. (56) and (57), we tried to use the values from FC analysis and to separate t_{eff} by adjusting M_{c0}. Unfortunately, simple substitution of these parameters gave poor results. By varying all three parameters, we finally found a plausible result. The results are not as good as those for VG/CP model, especially in the high K region, where the PL model does not provide much flattening. Deviations δM for this model are plotted versus K in Figure 29 b. It is superior to the A−K model, however, which varies as $ln(K)$ in the low K region. Both sets of parameter values from fitting FC and MFSR data are given in the table for comparison. Note that for a fixed field and temperature, *different* values are required to fit the two experiments. This unsatisfactory feature is characteristic of the following two models as well.

Figure 30

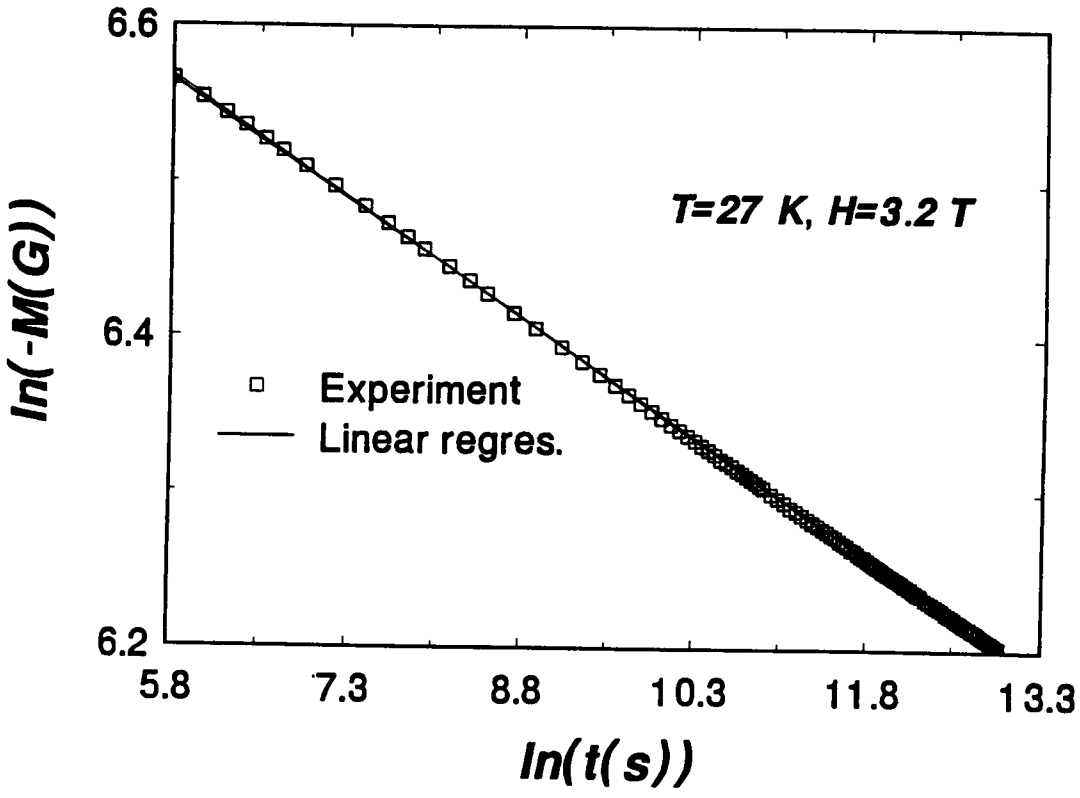

Power law (PL) relaxation or "Zeldov" model: ln(−M) versus ln(t).

(3) Griessen's model.

The model is based on Griessen's argument[19] that for any continuously differential potential, the activation energy can be written as $U(J) = U_0(1 + J/J_{c0})^{3/2}$ for $J \leq J_{c0}$. In our treatment, we left the exponent as an adjustable parameter rather than fixing it at 3/2. As noted,[19] there is no simple analytical relation between M and t. Consequently, we analyzed the FC data using the Arrenhius relation $\partial J/\partial t \propto e^{-U(J)/kT}$, so that $ln(\partial M/\partial t) = const. - (U_0/k_BT)(1 + M/M_{c0})^{\beta}$. Fitting the experimental data to this equation then gave all required parameters. Figure 31 shows the resulting relation between $ln(\partial M/\partial t)$ and $(1 + M/M_{c0})^{\beta}$. To analyze the MFSR experiments, we use Eq. (56) in the following form, obtained by changing the integration variable from t' to J:

$$m(t_H) = \frac{\pi}{3}[-J_{c0}a^3 - \int_{J(t_H,t^*)}^{J_{c0}} r^3(t_H,t')dJ] \qquad (64)$$

With numerical values for the parameters, the calculation was straightforward. Simply substituting the parameter values from the FC analysis gave poor results, a situation similar to that found with the PL model. However, freely adjusting the parameters for an optimum fit to the MFSR data gave rather good results with small deviations, as seen in Figure 29 (b). Unfortunately, comparison of the values for the FC versus MFSR studies shows them to differ significantly as seen in Table I.

(4) Double logarithmic model.

Figure 31

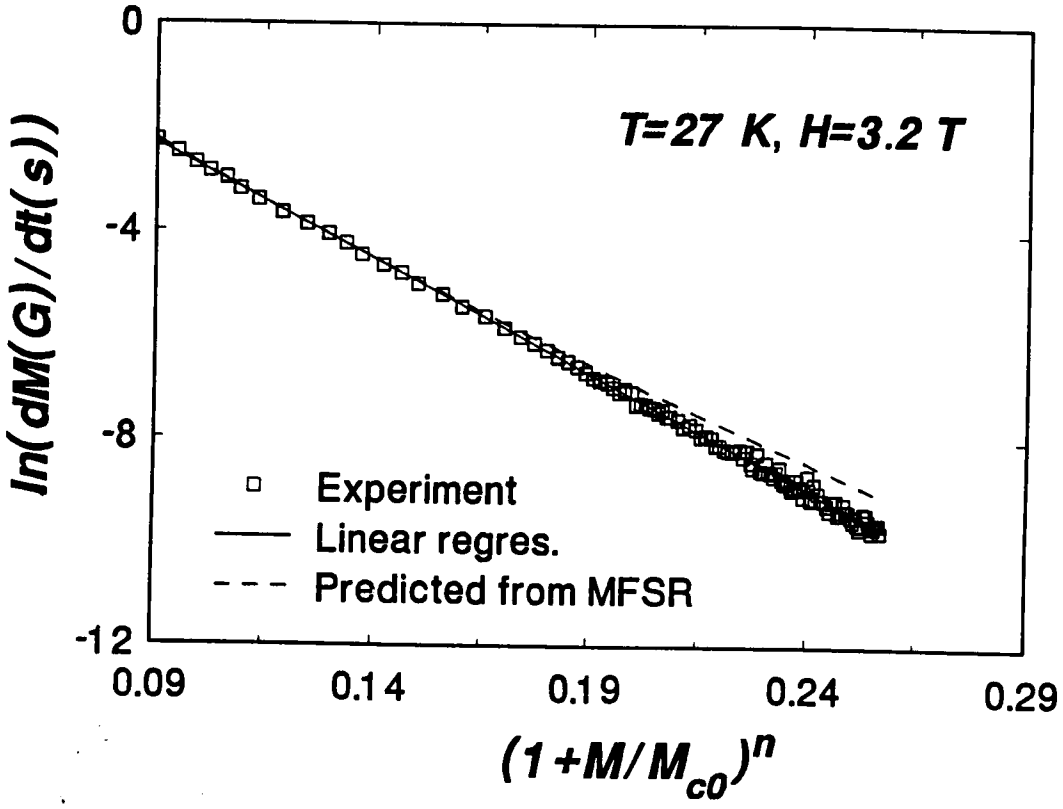

Analysis of Griessen's model: $\ln(\partial M/\partial t)$ versus $(1+M/M_{c0})^n$ with $n=2.16$: The dashed line was calculated using parameters obtained by fitting this model to the MFSR data; values are given in Table I.

Figure 32

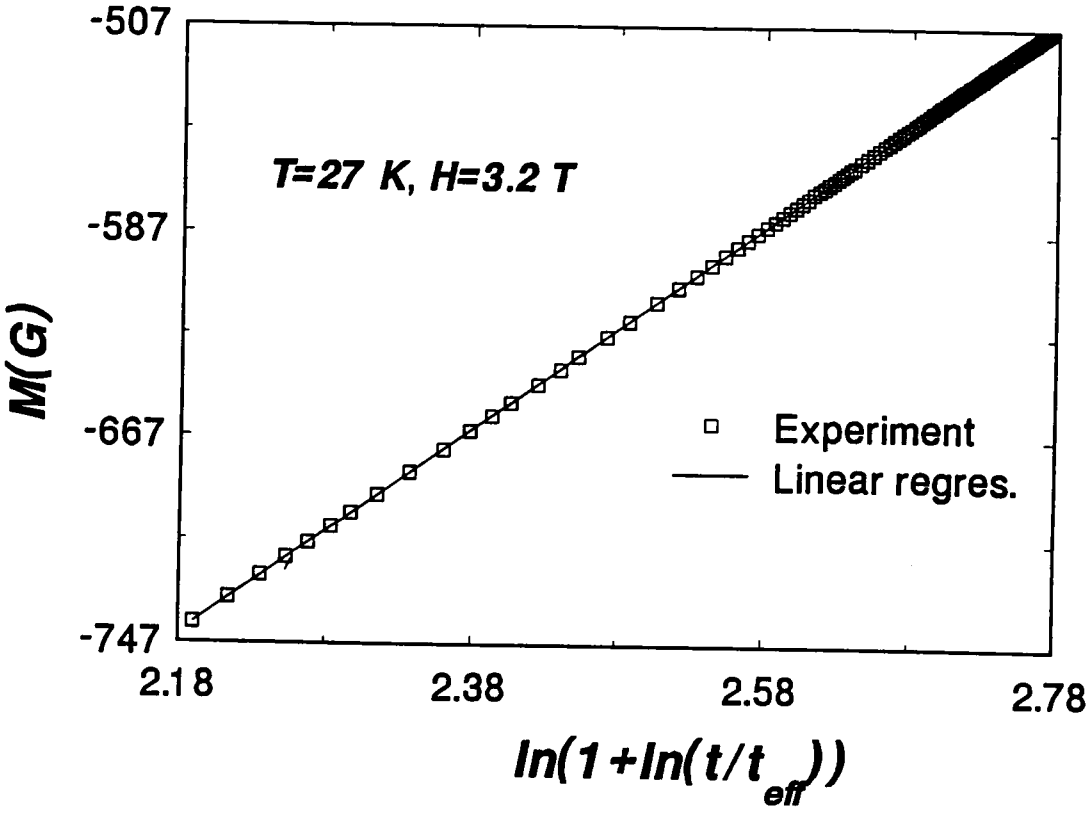

Double logarithmic "DL" model: Time dependent M versus $\ln(1+\ln(t/t_{eff}))$.

The DL model comes from an empirical expression (IV.1) that we devised for describing M(t):

$$M(t) = M_{c0} + c \ln[1 + \ln(t/t_{eff})] \qquad (t/t_{eff} > 1) \qquad (65)$$

This relation leads to an exponential dependence for U(J). While it is quite effective in fitting FC data with $t >> t_{eff}$, as shown in Figure 32, it among the four recent models provides the poorest description of the MFSR data, even when allowing all parameters M_{c0}, $\tilde{c}$ and t_{eff} to vary freely. One sees in Figure 29 (b) that $\delta M(K)$ is too large in the high K region. Expressed differently, the model overestimates the magnetic decay at short times. Analogous results were obtained at T=49 K and H=1.8 T.

IV.3.3 Discussion

In Table I are tabulated sets of best values for the various parameters, for each experiment and each model. For all recent models, we obtained good fits to the FC data, using 4 parameters in Griessen's model, 3 in the VG/CP or DL models, and 2 in the PL model. The quality of each fit, as given by the "goodness of fit" R^2 from linear regressions, is listed in Table I. (For Griessen's model, the lower value for R^2 comes in part from differentiating the data to get dM/dt, which accentuates noise in the data). In analyzing the MFSR experiments, both the VG/CP and Griessen models gave quite good descriptions of the experimental results (with the PL model less satisfactory), *provided* that the physical parameters were adjusted to these data. *Only the VG/CP*

model gives a consistent description of both the FC and MFSR experiments with one set of parameters. The other three models were incapable of a consistent description over such a large window of time. One might question this result, reasoning that the models use different numbers of parameter; consequently, incorporating more parameters might improve the fitting quality for any model. However, we stress that this brute force approach may make it even more difficult to obtain consistent parameters for the independent experiments, unless the model is correct.

One legitimate concern is the uniqueness of the fits. Since we find that only VG/CP relations give a consistent description of the experiments, one should ask, do there exist other sets of reasonable parameters that satisfy these VG/CP relations *and* give equally good fits to the data? Let us first consider the FC data for M(t) and assume for the moment that the time origin t_0 is known. Then the interpolation formula Eq. (59) has 3 parameters, but the exponent μ is the only *non*linear parameter. For a given trial value of μ (manually selected), the two *linear* coefficients, namely the intercept $(M')^{-\mu}$ and the slope C, are uniquely and unambiguously defined by standard linear least squares regression methods. Then we manually vary μ to obtain the best value of R^2. To illustrate, the inset of Figure 28 plots as a function of μ the quantity $1\text{-}R^2$, which is ideally zero. Its absolute minimum corresponds to the value $\mu = 0.482$, as given by the middle curve in the inset, Figure 28. The trends in the inset continue to much larger or much smaller trial values of μ. So we see that there is a unique value of μ for a fixed

time origin t_0. In the case just considered, we made the physically reasonable assignment $t_0 \approx t_H$, where t_H is the "clock time" at which the magnetic field reaches the desired value. We adjusted this time origin slightly to include the effects of magnetic relaxation during application of the field: with our field sweep rate of $\sim$500 G/s, the calculated difference between t_H and t_0 is only $\sim$3 seconds. With this time base, the SQUID magnetometer makes its initial measurement at time t = 86 s. (To avoid slight transients in the magnetometer after the large field change, we exclude the first 1-2 measurements and analyze data for times $t \geq$ 300 s.) To illustrate the effect of a different origin for the time base, we offset the time origin by $\pm$30 s and again minimized (1-R^2). The outer two curves in Figure 28 (inset) show the results versus trial values for μ. Clearly the quality of the fit deteriorates, with the minimum value of (1-R^2) becoming worse. This analysis demonstrates that the time base in the flux creep (FC) experiment is well defined and physically consistent, and that the resulting value for the exponent μ is unique. For FC studies at other temperatures and magnetic fields, the results are similar. In the MFSR analysis that involves four nonlinear parameters, it is much more difficult to find the best fit. As discussed in the previous section, a numerical fit to the data requires that one find the root of a nonlinear equation. A root *existed* only in a very narrow range of parameter space, covering $\Delta\mu \sim 0.02$, for example. In this region where a solution was possible, nonlinear least squares regression led to the values in Table I. The fact that no solution exists over a substantial range of parameter space gives strong evidence that the values obtained for the MFSR analysis are unique. These

detailed considerations confirm that, among the models considered, only the VG/CP theory gives a consistent description of the flux creep and sweep rate experiments.

Let us now consider the results of this analysis. The effective time scale t_{eff} is the least well defined quantity, since it is obtained only to logarithmic accuracy. We view the value $t_{eff} \approx 0.2$ s as more reliable, since it is determined mostly by MFSR data at high K, where the VG/CP model works quite well. As explained by Feigel'man et *al.*,[15] the time t_{eff} is a macroscopic time that depends both on sample dimensions and the details of the vortex pinning-hopping process. Their explicit relation (Eq. 14 in ref. 15) is $t_{eff} = \pi d^2 T/(u\omega_m cB)|\partial J/\partial U(J)|$. Here d is the sample dimension, u is the vortex hopping distance, ω_m is the elementary attempt frequency for hopping, c is the speed of light, and U is the effective pinning energy expressed in units of Kelvin. Solving this expression gives $u\omega_m \sim 0.1$ cm/s for the elementary hopping velocity of vortices. This result compares reasonably with the earlier value[58] ~ 25 cm/s for $Y_1Ba_2Cu_3O_7$, particularly when one considers the logarithmic accuracy of both values.

It is now clear that several different analytical expressions can describe well the experimental data over a sufficiently limited time window. Studies over a wider window impose a much more stringent test of the theories. To illustrate this point, we plot in Figure 33 the relative quantity *-M/M(t=400 s) versus ln(t)*. The discrete symbols are the experimental FC data and the various lines show model results, calculated using parameters from the short time MFSR experiments. Clearly the PL and DL models

Figure 33

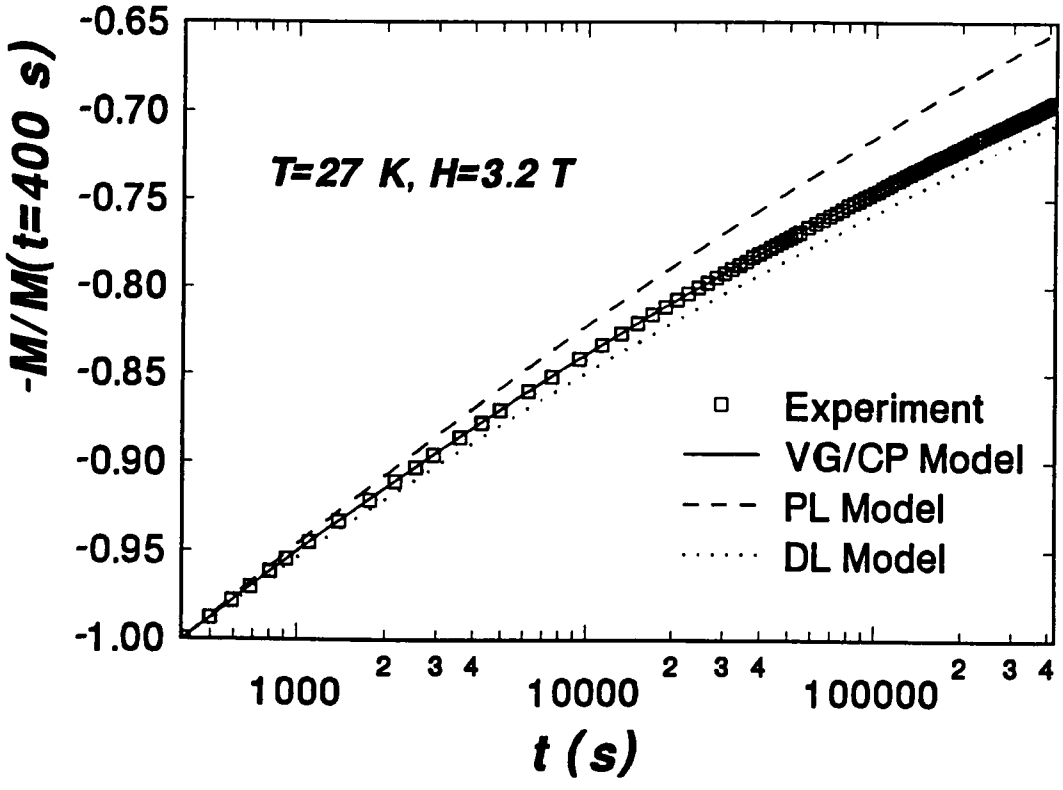

Magnetization versus log(t). Symbols are experimental points; lines show the time dependence for M as predicted by the VG/CP, PL, and DL models, using the parameters from analysis of the sweep rate study. The values of M are normalized to unity at t=400 s.

provide a good fit only over a relatively short time interval, while the VG/CP description is excellent over the entire range. An analogous presentation for the Griessen model is shown in Figure 31, where the dashed line corresponds to the parameters from the MFSR experiments. Substantial deviations are evident, showing graphically that the model describes these studies over a limited time domain only. Of the several models tested, only the VG/CP model provides an excellent description over the entire range of effective time.

We now estimate the range of time that the MFSR studies probe. As shown in section IV.2, a MFSR experiment probes the decay of currents at a time $\Delta t = t_H - t^*$, where t^* is a model dependent, effective origin of time that depends on sweep rate. For an estimate, one can use the relation for the A-K case, $t^* = aC_{A\text{-}K}/[K(0.79+a\alpha)]$ where a is a radius of the sample, $C_{A\text{-}K} = \partial J/\partial ln(t)$ and $\alpha = \partial J/\partial H$. An accurate calculation for the VG/CP model shows that at T=27 K and H=3.2 T, we have Δt = 2.4 s to 287 s for sweep rates K of 800 to 4.7 G/s, respectively. For T=49 K and H=1.8 T, Δt ranges from 0.3 s to 30 s for K in the range from 1076 to 4.7 G/s. Thus, the dependence of M on sweep rate K provides information on flux creep in time windows of (2.7 - 287) s for the study at 27 K and (0.3 - 30) s for the study at 49 K, respectively. The success of the VG/FC model demonstrates that it is correct over at least 5−6 decades of time. This wide window of effective time refers to studies under any one set of experimental conditions, i.e., fixed temperature and magnetic field.

IV.3.4 The value of μ

Given the success of the VG/CP model in describing magnetic relaxation experiments, it is interesting to compare the resulting values of the characteristic exponent μ with what we have found in IV.1 for sample 1 as well as with the theoretical predictions. Since both MFSR and FC measurements have given very consistent values for μ, the following discussion uses results from FC measurements, as the MFSR experiments are more difficult and tedious. The temperature dependence of μ for T = (10 - 60) K with H=2 T is shown in Figure 34. With increasing temperature, μ increases steadily from ~ 0.5 at 10 K, passes through a maximum ~ 1.3 near 23 K, and then decreases sharply at higher temperatures. The inset of Figure 34 depicts the field dependence of μ at T=30 K: μ first increases as a function of field from 0.75, reaches a maximum value of 1.5 (at H=1.3 T), then decreases at still higher fields. These features are quite consistent with those observed for a high J_c, proton irradiated $Y_1Ba_2Cu_3O_{7-\delta}$ single crystal.

To date, vortex glass theory[14] has no prediction for the temperature and field dependence of μ. Rather, it is regarded as a universal exponent with value $\mu \leq 1$, at least near the vortex glass transition temperature. Nattermann and Fischer[34] derived μ from two other exponents $\mu = \psi/(d+\varsigma-\psi)$, where d=3 is dimensionality. For geometry corresponding to $\psi \sim 1$ and $\varsigma \sim 0$, they estimated that $\mu \sim 0.5$. Neither of these cases describes the current experiments. In a theoretical treatment of collective pinning,

Figure 34

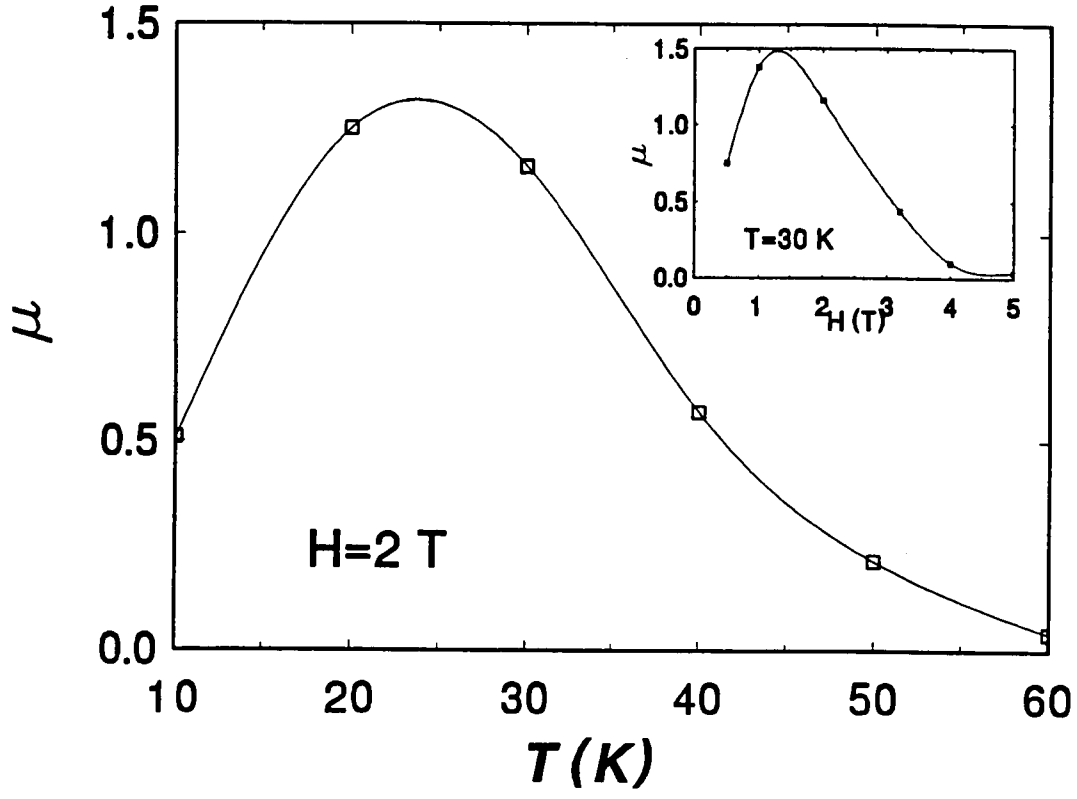

Temperature dependence of VG/CP exponent μ at H=2 T. Inset: Field dependence of μ at T=30 K.

Feigel'man *et* al.[15,45] predicted in the 3-D case the existence of three different regimes of current density J. In the highest current region with $J_{co}>J>J_1$, they have $\mu=1/7$, where J_{co} is the critical current density in the absence of flux creep, $J_1=J_{co}(L_c/a)^{7/5}$, a is the flux line lattice constant, and L_c is a longitudinal correlation length satisfying the relation $\xi<L_c<a$ in this regime. A second region with lower J has $\mu=3/2$, and a third region with still lower J has $\mu=7/9$. In our combined experiments where M (or J) decreased by about 44% of M_{c0} (J_{c0}) at T=27 K and 66% of J_{c0} at T=49 K, we observed only a single value of μ. These results suggested that the system in both cases should be in the first region with $\mu=1/7$, for the MFSR magnetization with high K is already close to M_{c0}. However, the experimental values of μ are larger than 1/7. Since L_c/a is related to the magnetic field, the three regions of current density (and values of μ) should be observable by varying the applied field. Our data in the inset of Figure 34, μ versus H at 30 K, schematically follows the theoretical predictions, particularly a peaked variation with a maximum near 3/2; however, the values at high field are quite small ($\sim$0.04), much smaller than 7/9, and may well reflect the initiation of other processes[15] not explicitly considered in the theory. Also, experimental observation of the predicted value $\mu=1/7$ in the high-J limit has remained elusive to date. Further understanding of the behavior of this characteristic exponent will require additional theoretical and experimental work.

IV.4 The Temperature-and Field- Dependent Activation Energy of a Proton Irradiated YBCO Single Crystal

In studies of the dynamics of flux motion in (HTSC), the anomalous temperature and field dependence of the activation energy observed in many magnetic relaxation measurements[42,49,59,60,61] as well as the difference of its magnitude found in comparing magnetic relaxation[7,39,62] and resistivity measurements[16,63,64] are quite controversial issues. Hagen and Griessen[49] first indicated U_0 rises with temperature T. They explained this T dependence via a distribution of pinning energies U_0 in any sample. Maley *et al*[13] argued that the nonlinear dependence of the activation energy U(J) on current density J, as first discussed by Beasley *et al*,[20] is the major reason for the anomalous rise of U_0 values with increasing temperature. They add that since magnetic relaxation studies are generally performed under conditions with J close to J_c while resistive measurements have $J << J_c$, the values extracted for U under different experimental conditions vary greatly. Recently Chaddah and Bhagwat pointed out[65] that, by employing the Bean model[29] and incorporating a field dependence of J, the quantity extracted from a magnetic relaxation measurement, $-kTM_0/(dM/dlnt)$, was not the activation energy but a scaled quantity $U^*=U_0/A(H,H^*,H_0)$, where $H^*=J_c(T)d/2$, d is the transverse dimension of the sample, and H_0 is another characteristic field. Assuming that U_0 is constant and that J_c decays exponentially with H, they calculated $A(H,H^*,H_0)$ and found that U^* would exhibit the anomalies with T and H. Thus they argued that the apparent unphysical increase of U_0 with T and H may be attributed to not

distinguishing between U_0 and U^* correctly. On the other hand, Gurevich[66] claimed that it is essential that U(T) should increase with T at low T. Incorporating a distribution of pinning energies into both current-voltage relationship and magnetic flux creep, he argued that $\varrho \sim \varrho_f n_f \Phi_0/B$, which is analogous to the flux flow resistivity $\varrho_f \sim \varrho_n B/H_{c2}$ in the Bardeen-Stephen model[67]. Here ϱ_f is flux flow resistivity, n_f is the mean areal density of free vortices and Φ_0 is the magnetic flux quantum. He pointed out that when $B < H_p \sim n_p \Phi_0$, where n_p is the density of the pinning centers per unit area, each pinning position can be occupied by only one vortex, since the interaction energy of two nearly coincident vortices is much larger than the pinning energy even in the strongest pinning case. Thus in a statistical sense, pinned vortices behave as fermions, while free vortices act as bosons. Furthermore, the activation energy is similar to the chemical potential which is determined by the density of vortices B/Φ_0, and by the distribution of pinning barriers. According to this definition he predicted that the activation energy at low T should increase with T when $B < H_p$ and furthermore, because of non-linearity of U(j), non-logarithmic magnetic time decay occurs in the flux creep regime.

Experimental efforts to extract values for U typically have entailed simultaneous changes in current J, temperature T, and perhaps field B. Consequently it has been difficult to determine the individual dependencies on these variables. In Chaddah and Bhagwat's argument, the quantities U_0 and U^* should be distinguished. However, in this study, we investigate the separate temperature and field dependencies of the activation energy U(T, H, J) for pinning of magnetic flux in the high-J_c, proton irradiated YBCO

single crystal (sample 1). We extract from magnetic relaxation investigations the variation of activation energy U on J, T, and H. In particular, we separate the influence of J by extrapolating U(J), which is measured in the range of J near J_c, to a lower-J region for study of U(T,H). Some features reported by Gurevich et al.[68] are found to agree with our experimental results.

IV.4.1 Principle

As we discussed in section III.2, according the BLW paper[20], the magnetic relaxation in a long cylindrical sample of radius ρ can be described by the Eq. (17)

$$\frac{\partial \Phi}{\partial t} = -2\pi \rho D(\rho, t) \tag{66}$$

with

$$D(r) = -hdv_0 e^{-U(h,J,T)/k_B T}$$

$$and \tag{67}$$

$$U = U_0 - hJvx \qquad (for\ t>t'\ \ or\ \ J<J')$$

where h(r) is the local field, t' is a crossover time and J'=kT/hvx. Here inverse hopping is neglected as it is not important when J is large, as in these magnetization measurements. Note that in Eq. (67), the quantity U_0 itself can be a complicated function of H, T, and J; the expression only separates out the Lorentz term. Experimentally we measure the magnetic moment m due to a distributed current density J(r). Starting from

its definition and using the Maxwell equation $(4\pi/c)J_{\varphi}(r)=-\partial h/\partial r$, we have (per unit length):

$$m=(1/2c)\int_0^a r\times J\,dv$$
$$=-(1/8\pi)\int_0^a r^2(\partial h/\partial r)\,dr\,d\varphi \qquad (68)$$

$$4\pi m=\phi(\rho)-\pi\rho^2 h(\rho) \qquad (69)$$

By assuming $h(\rho)=H=$the applied field, and substituting Eq. (69) into Eq. (66) we obtain:

$$4\pi\frac{\partial M}{\partial t}=-2\frac{D(\rho,t)}{\rho} \qquad (70)$$

where $M=m/V$ is the magnitude of the magnetization. Thus $\ln(\partial M/\partial t)$ is proportional to $U(h(\rho),J(\rho,t))$.

In the previous sections, we indicated the non-logarithmic time decay of magnetization and the data could be fitted by several models. Among them, the VG/CP model gives the best consistent description of our data up to 6 decades, whose activation energy is provided by

$$U(J)=U_0[J_{c0}/J)^{\mu}-1]/\mu \qquad (71)$$

In our experiments the exponent μ varies with T and H. If we were able to analyze U_0 and J_{co} as functions of T and H, we could eventually find the T and H dependence of U experimentally. Unfortunately, as we indicated early, in the analysis of FC

measurements, these two parameters are always mixed with the attempt time t_{eff}, which makes it difficult to extract U(T,H). In principal, we could solve this problem with the MFSR experiments, but the measurements are much more difficult and take much more time. On the other hand, an analysis employing the empirical expression, Eq. (34), makes it easier to separate these parameters. In particular, the double logarithmic model leads to an exponential dependence (IV.1) of U on J. From either Eq. (70) or Gurevich's theory[66], the resulting U is (see IV.1):

$$U/k_BT = -1 + (J_0 - J)/J_s + \exp[(J_0 - J)/J_s] \tag{72}$$

Eq. (71) and Eq. (72) appear very different, but in a certain regime of J, the actual values of U are quite similar. This is because Eq. (31) and Eq. (34) give very similar evolutions for M(t) within a limited experimental time window (though we have demonstrated that with a large time window, the interpolation formula is better than the empirical one, especially if the initial stage of flux creep is included). See Figure 35 for a comparison. Even when extrapolated a million years forward in time, these expressions differ only slightly, e.g. by $\sim 5\%$ for data at 30 K, 1 T. Furthermore, since dM/dt enters logarithmically in the calculation of U, some possible difference in dM/dt will not have a significant effect. Therefore, values of U with $J \sim J_c$ should be very similar whether we employ Eq. (71) or Eq. (72). However, the empirical Eq. (34) has been tested only in the $J \sim J_c$ window where inverse flux hopping is neglected as we indicated before. Consequently, Eq. (72) should not be extrapolated to very much lower J-values. Later in this section, we will compare values of U(J) from Eq. (71) and Eq. (72). With these considerations, we use Eq. (72) for studying both the T and H

Figure 35

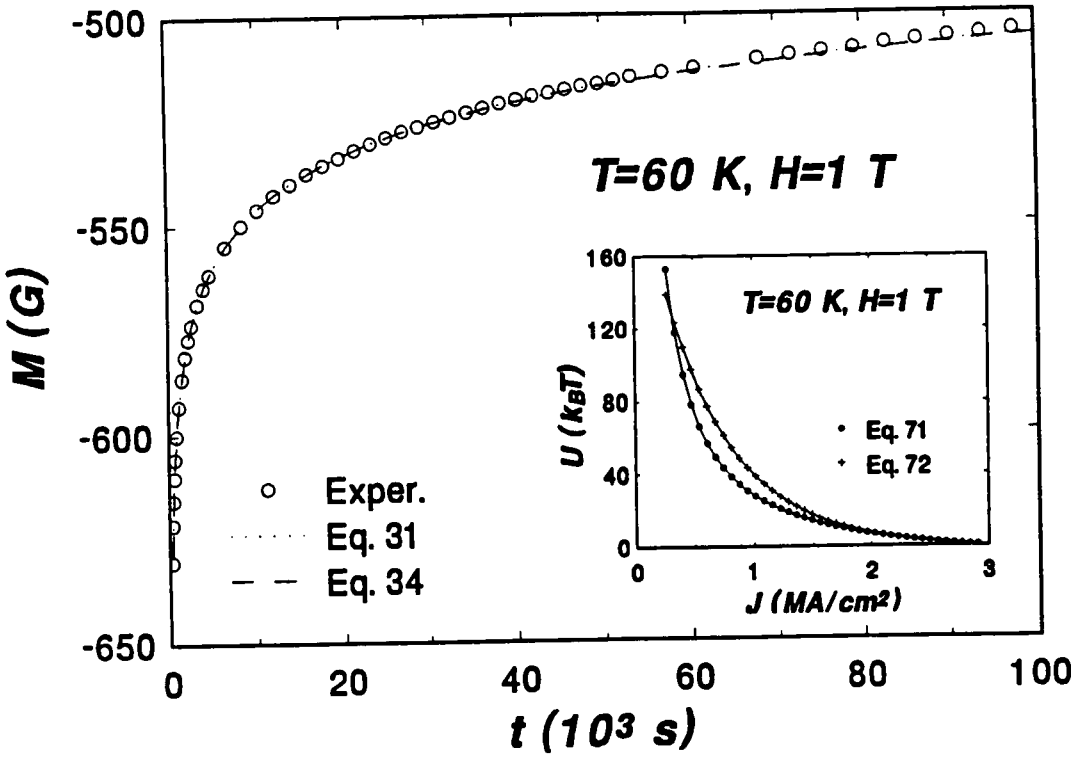

The magnetization M vs. time t at T=60 K, H=1 T. lines are fits of experimental data to Eqs (31) and (34), respectively. Inset: U vs. J from Eqs. (71) and (72), respectively.

dependencies of U, and require that J be larger than some minimum value $\approx 2.5\times10^5$ A/cm^2.

To make sure that the assumption of uniform J flowing through the sample is acceptable, we show that even if an explicit dependence of J on h is included (which introduces the factor[65] $A(H,H^*,H_0)$ into $U^*=U_0/A(H,H^*,H_0)$), Eq. (72) remains unchanged. The proof is the following:

$$M=\frac{1}{2cv}\int rxJdv=\frac{\pi}{cv}\int J_\varphi r^2dr \tag{73}$$

After integrating by parts, we have for a fully penetrated sample:

$$M=\frac{2\rho J_\varphi(\rho)}{3!c}-\frac{2\rho^2}{4!c}\frac{\partial J_\varphi(\rho)}{\partial r}+\frac{2r^3}{5!c}\frac{\partial^2 J_\varphi(\rho)}{\partial^2 r}-\frac{2\pi}{5!vc}\int r^5\frac{\partial^3 J_\varphi}{\partial r^3}dr \tag{74}$$

Taking $h(\rho)=H$ and keeping only linear terms of J gives

$$M=\frac{2\rho J(H)}{c}\left(\frac{1}{3!}+\frac{\rho}{4!}\frac{\partial J_\varphi(H)}{\partial h}+\frac{\rho^2}{5!}\left(\frac{\partial J_\varphi(H)}{\partial h}\right)^2+\ldots\right) \tag{75}$$

or (in practical units):

$$J(H)=(30M/\rho)A(H)$$

with

$$A(H) \equiv (1 + \frac{\rho}{4}\frac{\partial J_\varphi(H)}{\partial h} + \frac{\rho^2}{4 \cdot 5}(\frac{\partial J_\varphi(H)}{\partial h})^2 + \ldots)^{-1} \qquad (76)$$

Thus incorporating the field dependence on J introduces a correction factor A(H) into the relation between J(H) and M. But, as we see from Eq. (72), it affects the values of J, J_0, and J_s but not U, where the factors A(H) cancel.

Determining the parameters J_0 and J_s at various temperatures and magnetic fields allows us to find the T and H dependence of the activation energy experimentally. Here we assume (without proof) that the formula (72) can be extrapolated to lower current, but not beyond the stated assumption given in Eq. (67). In the following we will compare the resulting values for U at low J with those reported in literature.

IV.4.2 Results and analysis:

The FC experiments were performed on sample 1 in a SQUID magnetometer (Quantum Design MPMS) with field applied parallel to the c-axis. The temperature ranges from 7 K to 70 K with field from 0.5 T to 5 T in the experiments. During the observational time window, J varied from 10% of J_c (7 K, 1 T) to 40% of J_c (60 K, 5 T). Here J_c is calculated from M-H hysteresis loop measurements made with 15 second pauses after field changes to allow the magnetometer to settle.

To illustrate the results, Figure 36 shows a set of flux creep data at 30 K for applied fields of 0.3-5 Tesla. The measured magnetization M(t) is plotted versus the "double logarithm" $\ln[\ln(t/t_{eff})+1]$. In analyzing these data, the macroscopic time t_{eff} was used as a non-linear fitting parameter whose value was adjusted to give a precisely linear representation of the data. Both M_0 and the slope *a* monotonically decrease with field. Data at other temperatures and fields behave similarly. For the data in Figure 36 with H=0.3 T, the horizontal shift is caused by the smaller t_{eff} in this low field. To compare the quality of fits obtainable with Eq. (31) and Eq. (34), we show in Figure 35 the quantity M vs t at T=60 K and H=1 T. The open symbols are experimental data, while the nearly coincident lines are fits the two expressions. While the maximum difference between the measured data and either one of the fitting curves is about 2 G, the two fitting curve themselves are almost identical with differences smaller than 0.5 G. The inset of Figure 35 shows U vs J calculated from Eq. (71) and Eq. (72). As expected, the two curves are close for J in the range from J_{c0} ($\sim$3 MA/cm^2) to $\sim$ 0.5 J_{c0}; the difference grows as J decreases. At 0.08 J_{c0}, the relative difference in U is about 12 %, but it increases quickly at still lower J-values. Figure 37 plots J_0 and J_s as a function of T for fields of 1-5 T. An important feature is that J_0 and J_s have very similar curvature as a function of T and H. For instance, in 2 T field, J_0 and J_s decrease by a factor of 15 in going from 10 K to 70 K, but the ratio of J_0/J_s changes by only $\sim$ 35%. The inset of Figure 37 shows the ratio J_0/J_s as a function of T for H=2 Tesla. The other noteworthy feature is that J_0/J_s has a low field peak. This peak matches the peak in J_c extracted from the M-H hysteresis loop measurements. The attempt time t_{eff}

Figure 36

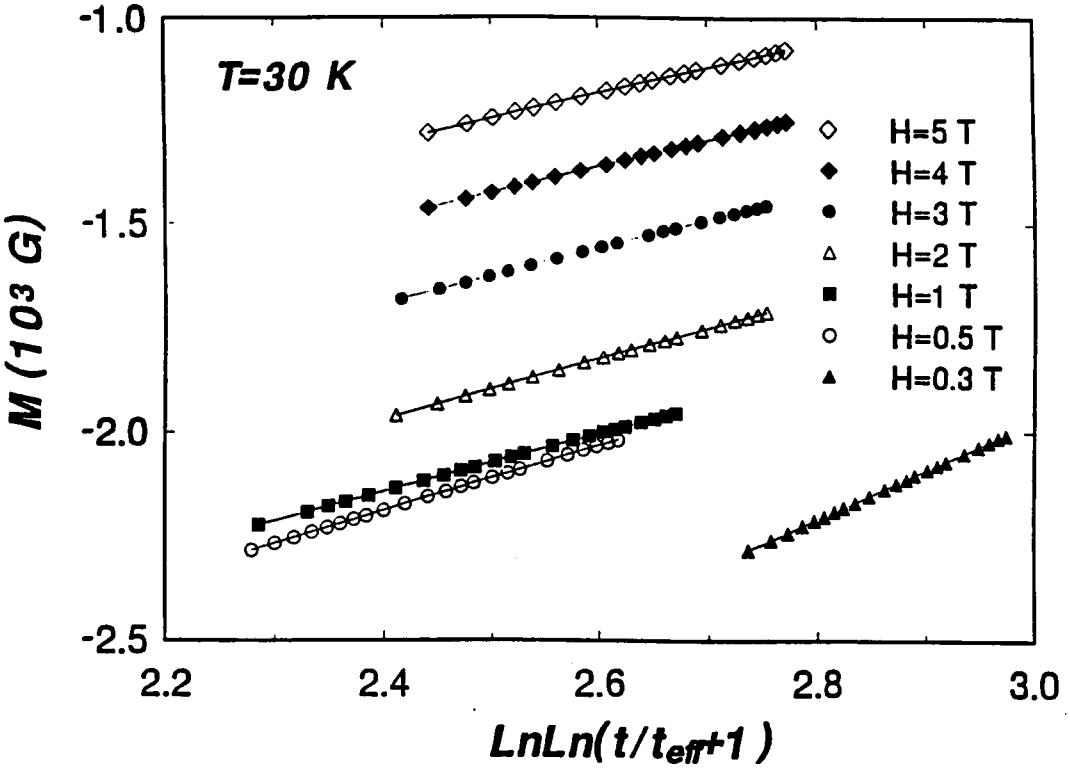

Magnetization M vs double-logarithm of time for single crystal $Y_1Ba_2Cu_3O_7$ at T=30 K, with applied field H $\|$ c from 0.3 to 5 Tesla. The horizontal shift of the data at H=0.3 T results from the small value of t_{eff} at this field. Overall results at other fields are very similar.

Figure 37

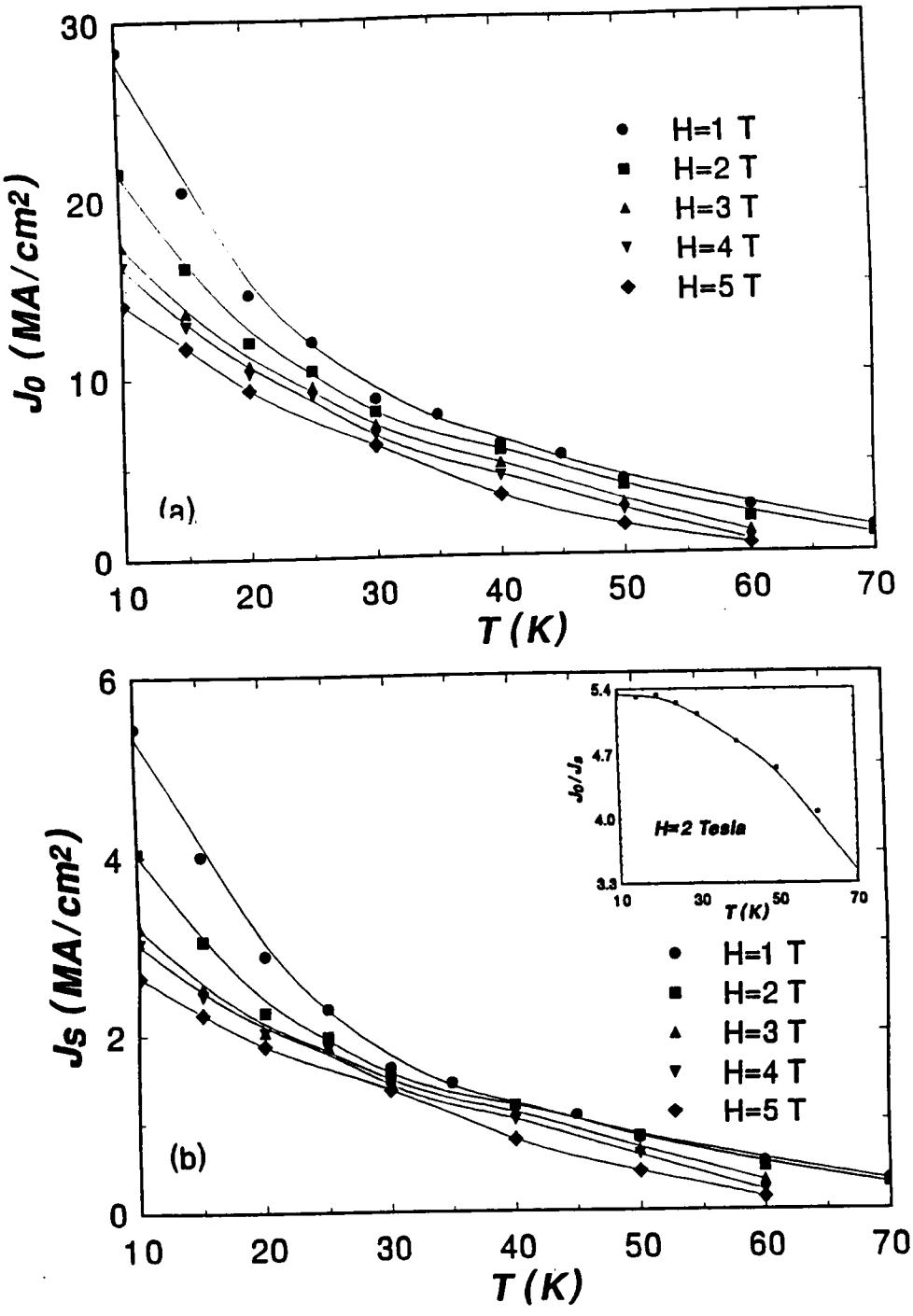

The material parameters (a) J_0 and (b) J_s vs T, as extracted from magnetic relaxation measurements with H||c. The two have similar temperature dependencies. Inset on (b): J_0/J_s vs T at H=2 Tesla.

depends on T and H also. Some results for t_{eff} are shown in Figure 38. In general, the values lie near $10^{-3} \sim 10^{-2}$ s, except at low field and low temperature where t_{eff} is relatively small. At 60 K and 4 Tesla, t_{eff} is of order one second. This agrees with the our studies in IV.3 and recent argument that t_{eff} is a macroscopic quantity related to sample geometry and flux flow resistivities[34,45,69].

Having $1/J_s$ and J_0/J_s data from experiments we are able to calculate U(T,H,J) using Eq. (72). The temperature dependencies of U for several fixed J values, with H=2 T and 5 T, are shown in Figure 39 (a) and Figure 39 (b), respectively. The field dependence at T=30 K and 60 K is plotted in Figure 40 (a) and Figure 40 (b). The characteristic features are summarized as follows:

1. U(T) for fixed H and J increases with increasing T and reaches a peak $U_m(H, J)$ at some $T_m(H, J)$ (see Figure 39 (a) and Figure 39 (b)).
2. The peak values $U_m(H, J)$ and $T_m(H, J)$ decrease with current density J (see Figure 39 (a) and Figure 39 (b)). They also decrease with H (compare Figure 39 (a) with Figure 39 (b)).
3. For fixed T and J, U(H) increases with field H and has a maximum between H=0.4 T and 1 T (see Figure 40 (a) and Figure 40 (b)). The maximum is not sensitive to the temperature; however when J approaches J_c, it moves towards lower field which matches the peak seen in J_c measurements.
4. For H>2 T, we have $U(H) \sim H^{-\alpha}$, where α decreases with decreasing J and T. At T=30 K, α is 1.08 at $J=4\times10^6$ A/cm^2 but it decreases to 0.73 at $J=2.5\times10^5$

Figure 38

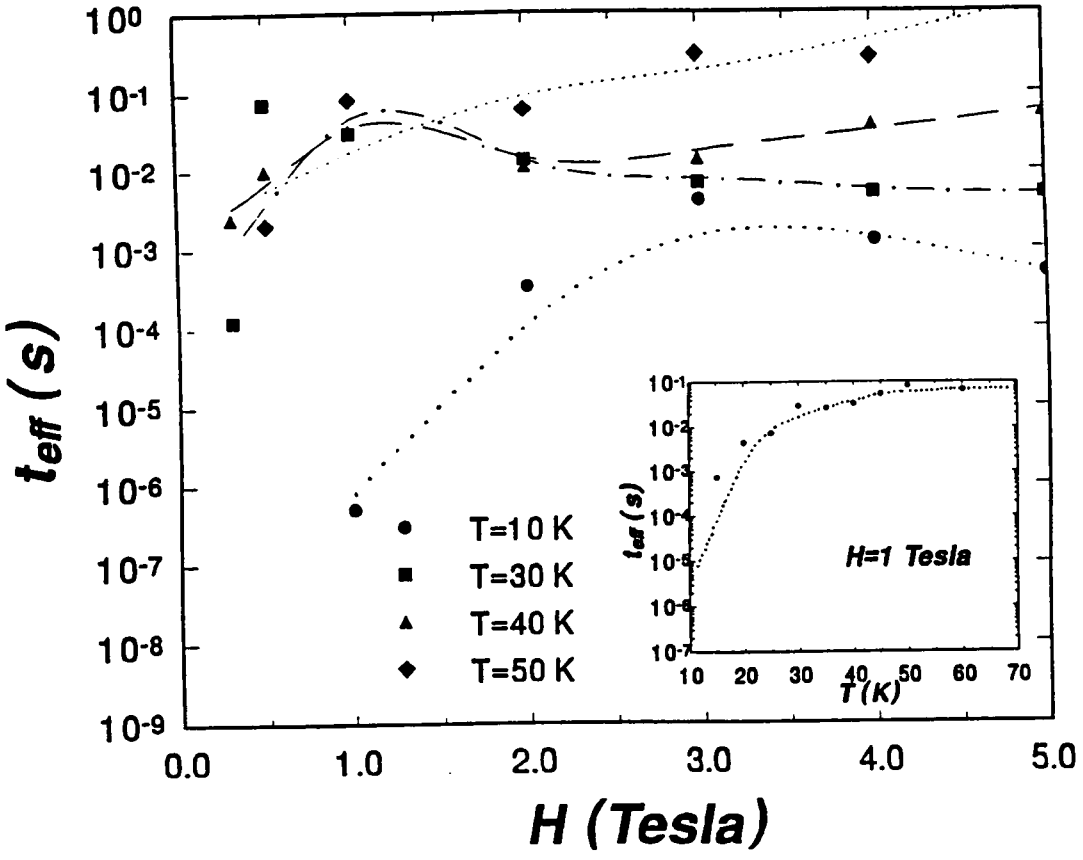

The attempt time t_{eff}, obtained as a fitting parameter, vs H with H||c. Inset: t_{eff} vs T at H=1 Tesla. In Figs 39-41, the lines are guides to the eye.

Figure 39

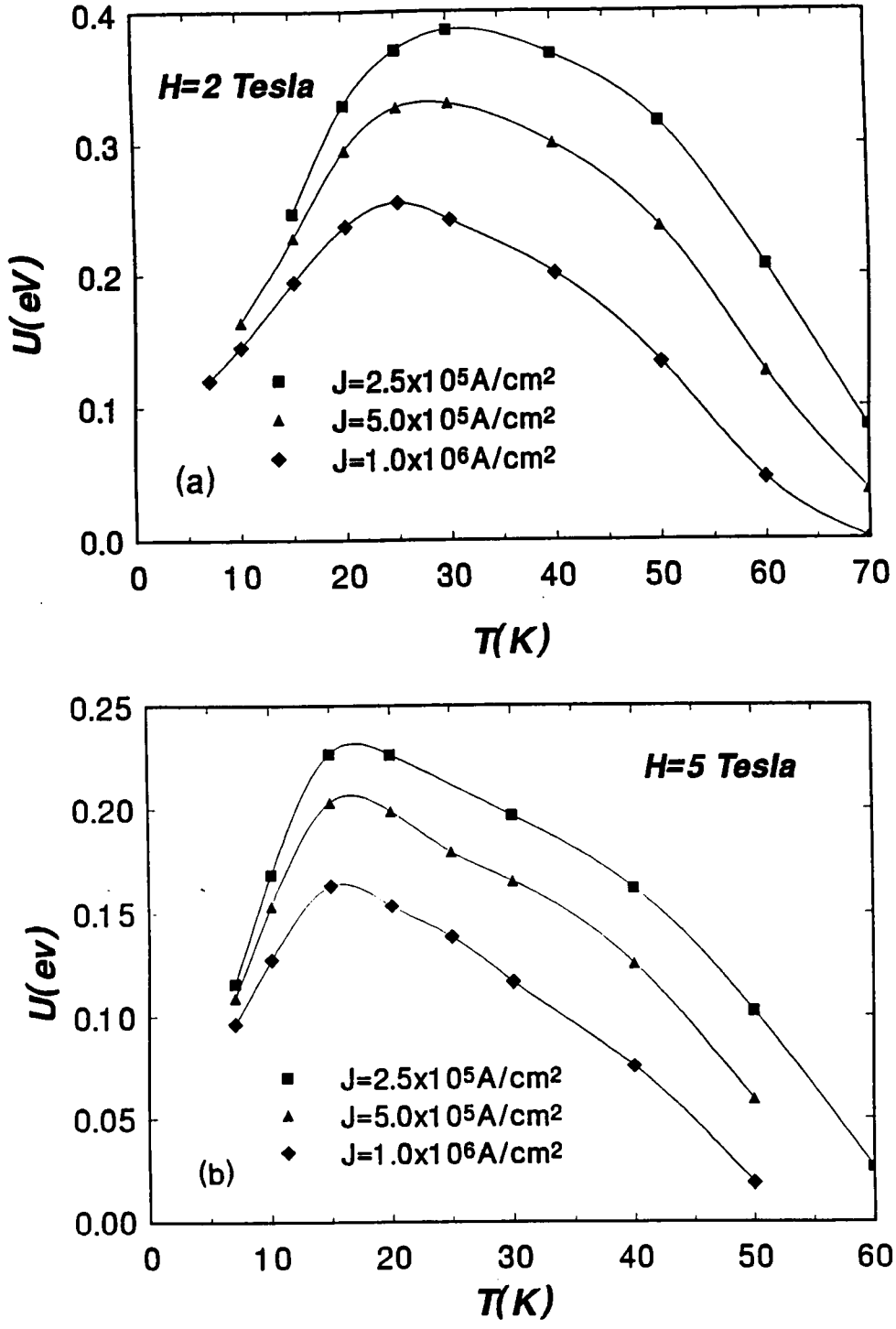

The activation energy vs T, (a) at H=2 T, and (b) at H=5 T. Current density J is fixed at the values shown.

Figure 40

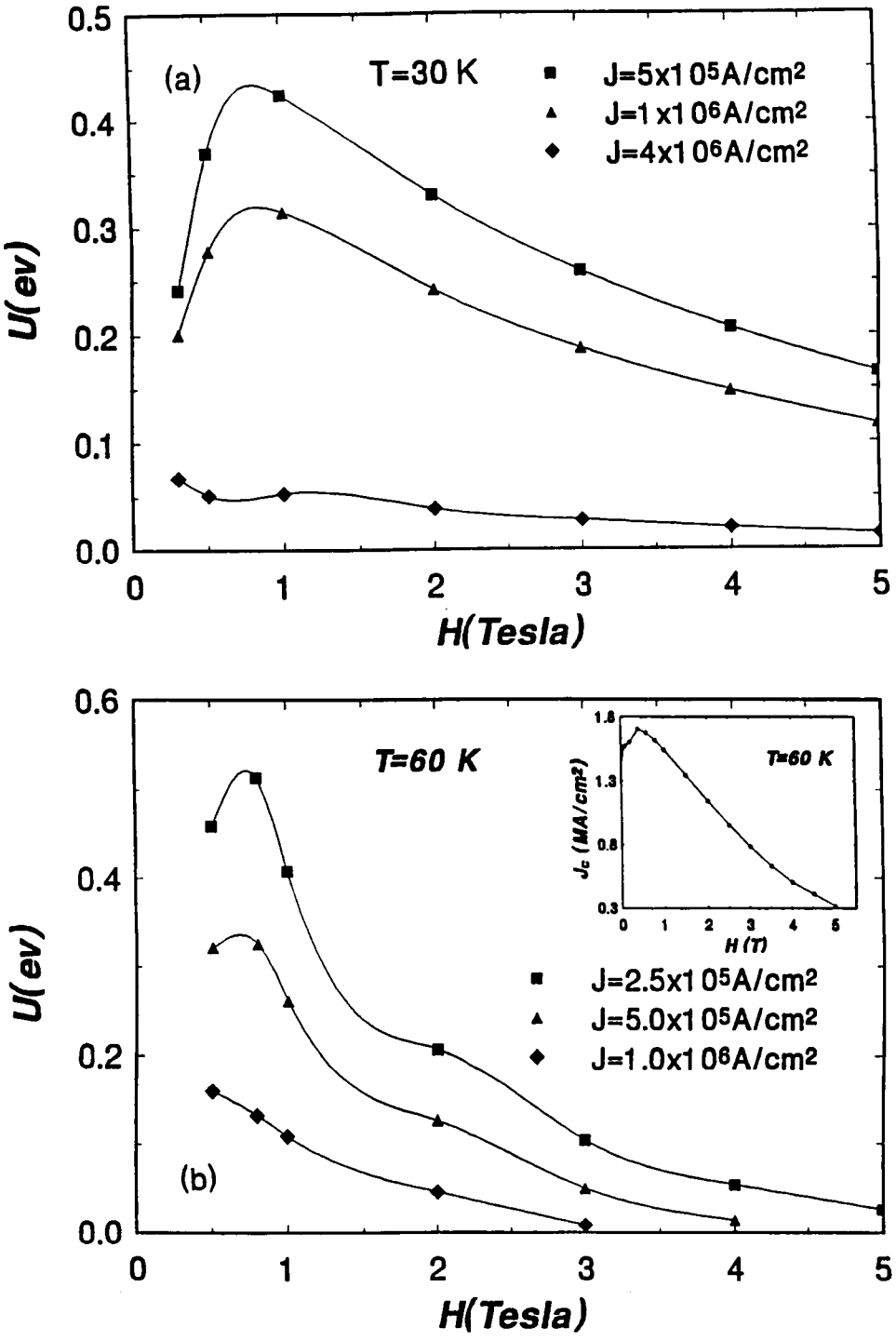

The activation energy vs H, (a) at T=30 K, and (b) at T=60 K. The inset on (b) shows the J_c at T=60 K extracted from hysteresis loop measurements.

A/cm^2. For the latter J value, α increases with T and becomes to 1.2 at T=50 K. For T=60 K with high J-values the fitting to $H^{-\alpha}$ becomes poor.

The results indicate that the thermal anomalies of U cannot be interpreted solely in terms of a nonlinear dependence of U on J. As also shown above, the field dependence of J does not affect the values of U extracted using BLW theory. Hence it is unlikely that the explanation posed by Chaddah and Bhagwat[65] is appropriate here. In addition, Jones et al[70] observed an anomalous temperature dependence for U in transport measurement on c-oriented $YBa_2Cu_3O_7$ granular films grown on polycrystalline YSZ. Thus it seems that the apparent physical behavior is real.

Features 1 and 2 are consistent with the depiction by Gurevich et al.[68]. The activation energy at low temperature in that model can be written as:

$$U(T, B, J) = U_0 y(J) - \pi^2 k^2 T^2 F'(U_0)/[6F(U_0)y(J)] \qquad (77)$$

where U_0 is the minimum depinning energy at T=0, F(E) is the distribution function of pinning potentials, $F'(U_0)$ is the derivative of F at U_0, y is a function with y(0)=1 and $y(J_0)=0$. If $F'(U_0)<0$, as is possible for a nonsymmetrical function F(E) with a pronounced high energy tail[49,62], then U increases with T for $B<B_m$ and decreases with T for $B>B_m$. In interpreting this behavior, we should realize that the activation energy in this model is not an individual depinning energy. The pinning potential is analogous to the chemical potential for a Fermi electron gas. At T=0, all barriers with depinning energy $E>U_0$ are occupied by flux lines. When T is not zero, some vortices having E-

$U_0 \leq kT$ are able to move to lower energy barriers, which decreases the activation energy.

It is difficult to understand the low field anomalies. According to Eq. (77), U decreases with H at T=0. Though at finite T, the second term might be positive in some cases, usually it is considered a smaller one. As we mentioned above, when J is close to J_c the peak of U at low field matches the peak in magnetization measurement, for which several possible explanations have been proposed[71,72,73]. Daumling and Larbalestier[74] indicated, that for disk-shaped samples with thickness of d, there exists a radial field $h_r \sim d \cdot J_c/2$ in addition to the axial field h_z. Conner et al[73] showed that anisotropy of the critical current produces a peak in M(H) that rides on top of M(H) from an isotropic current density. It is reasonable to think, according to this model, the shielding current from dh_r/dz decays more slowly than that from dh_z/dr because of an anisotropic activation energy. However, questions remain; for example, the maximum h_r at 77 K is about 0.1 T while $h_r \sim 3T$ at 15 K, but the peaks of M(H) occur at the same position of H=0.4 T at both temperatures. Besides that, Figure 40 shows that the field corresponding to the peak even increases for the smaller J. According the above explanation, we would expect to see it decreases since small J means a smaller effect from h_r. It is possible that several different mechanisms contribute to this anomaly; the peak move to lower field at large J may be due to the increasing h_r. To clarify this point requires further work.

Finally we compare the magnitude of the activation energy to those from resistivity measurements. At T=70 K and H=2 T, the present values of U are 0.08 eV and 0.04 ev for J=2.5x10^5 A/cm_2 and 5x10^5 A/cm^2 respectively Figure 39 (a)). From transport studies of epitaxial $YBa_2Cu_3O_{7-\delta}$ thin films by Zhu *et al.*[75], values of 0.18 and 0.08 were obtained for the same conditions. In order to compare more easily with values reported in the literature, we now use $U_{eff}=U-T(\partial U/\partial T)$ which corresponds directly to the experimental quantity $-\partial \ln \varrho/\partial(1/T)$, the slope of an Arrhenius plot. For comparison with results of Hettinger[64] and Zeldov[16], Figure 41 plots our calculated U_{eff} versus T in the range 60-70 K with H=2 T. Though the reported results of Hettinger et al. are at H=12 T, values at other fields can be calculated by employing their relation $U \sim H^{-\alpha}$ with $\alpha=1$. In the same way, we are able to scale Zeldov's values of U_{eff} at 6 T to 2 T, using their result of $\alpha=1.28$. For example, our average U_{eff} values for T=60-70 K in Figure 41 are 0.96, 0.75 and 0.58 eV with current density of 2.5×10^5, 4.5×10^5, and 6×10^5 A/cm^2 respectively; by comparison, studies from Hettinger et al. yield U_{eff}=0.72, 0.62, and 0.58 eV for epitaxial thin films with the same conditions. These values are quite comparable. Experiments on epitaxial thin films by Zeldov et al. give respective values near 1.9, 1.4 and 1.36 eV, which are larger by a factor of 2. Considering the expected differences from sample-to-sample, we judge all these results to be comparable. This also substantiates the validity of extrapolating Eq. (72) to somewhat lower current densities.

Figure 41

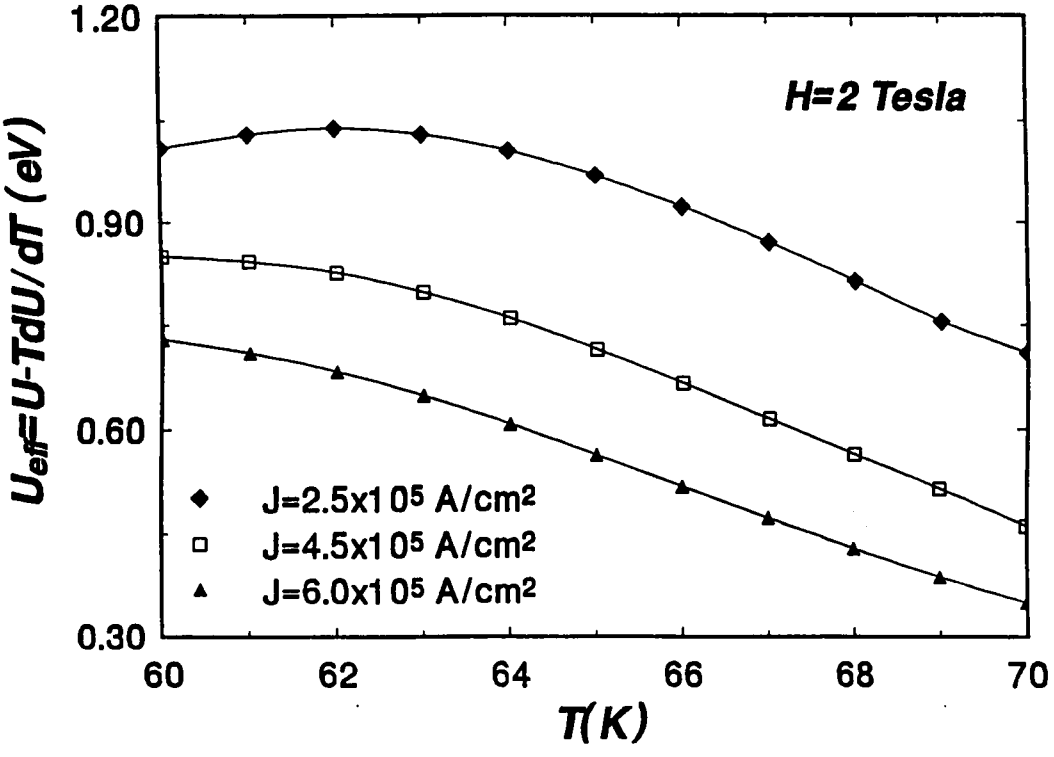

U_{eff}=U-T(dU/dT) vs T with H$\|$c=2 Tesla. This quantity can be compared to the slope of Arrhenius plot from resistivity measurements.

To conclude this section, the activation energy U for flux creep in a high J_c, proton irradiated YBCO single crystal was studied experimentally. The temperature and field dependence at fixed current was obtained by extrapolating the current dependence found in magnetic relaxation measurements with J close to J_c. Peaks in U were found both at low temperature and low field. The former one can be understood by Gurevich's model. The attempt time t_{eff}, used as fitting parameter, lies near $10^{-2} \sim 10^{-3}$ second in most cases. The resulting magnitude of U_{eff} is quite comparable to those obtained in high J_c epitaxial films from resistivity measurements, which supports the correctness of the present analysis.

Chapter V

SUMMARY AND CONCLUSION

The time dependence of the irreversible superconductive magnetization has been studied in a high J_c, proton-irradiated $Y_1Ba_2Cu_3O_{7-\delta}$ single crystal and a melt-textured-growth sample for long periods, up to $3.5x10^5$ s. A nonlogarithmic decay of magnetization M with time was observed for a wide range of temperatures and magnetic fields. This deviation from a conventional Anderson-Kim logarithmic time dependence is not due to the approach of the system to the equilibrium state; in contrast, it fits the predictions of several recent models with comparable accuracies.

In complementary investigations of the early stages of magnetic relaxation, the effects of field sweep rate $K=\partial H/\partial t$ on magnetization hysteresis loops M(H) and on flux creep studies M(t) have been studied using the Bean critical state model and TAFC model. To first order, a logarithmic dependence of magnetization M on field sweep rate K is found, with a slope dM/dln(K) equal to the flux creep rate dM/dln(t). However, at both high K and low K region, deviations from linear dependence of M on ln(K) are apparent. The agreement with other flux creep models is much better than with the Anderson-Kim form $M \propto \ln(t)$.

The effects of field sweep rate on the magnetization provide information of magnetic relaxation in time window $\Delta t = t^* - t_H$, where t^* is considered as the true time origin and t_H is the time when field reaches the target value. The exact values of Δt depends on the field sweep rate; however, it is easy to access the range from ~ 0.01 s to ~ 100 s in the experiments. Hence, with combining MFSR experiments with flux creep experiments, the time window can be extended up to 6 decades. The parameters used for fitting MFSR experiments should be able to fit the FC measurements, if the model is correct. Among four models selected, only VG/CP model provided this consistency. Consequently, the experimental studies favor this controversial theory.

BIBLIOGRAPHY AND REFERENCES

A. General Background Literature

[1] Tinkham, M.: *Introduction to Superconductivity*, McGraw Hill, N. Y., 1975.

[2] De Gennes, P. G., *Superconductivity in Metals and Alloys*, Benjamin, N.Y., 1966.

[3] Rose-Innes, A. C. and F. H. Rhoderick, *Introduction to Superconductivity*, Pergamon Press, N. Y., 1969.

[4] Vladimir Z. Kresin and Stuart A. Wolf, *Fundamentals of Superconductivity* Plenum Press, N. Y. and London, 1990.

[5] D. Schoenburg, *Superconductivity*, Cambridge University Press, Cambridge, 1960.

[6] London, Fritz, *Superfluids*, Dover Publications Inc. N. Y., 1960.

[7] Jeffrey W. Lynn (Editor.-in-Chief), *High Temperature Superconductivity*, Springer-Verlag, N. Y., Berlin, Heidelberg, London, Paris, Tokyo, and Hong Kong, 1990.

B. Notes and References

1 J. G. Bednorz and K. A. Muller, Z. Phys. B **64**, 189 (1996).

2 M. K. Wu, J. R. Ashbum, C. J. Torng, P. H. Hor, R. L. Meng, L. Gao, Z. J. Huang, Y. Q. Wang, and C. W. Chu, Phys. Rev. Lett. **58**, 908 (1987).

3 H. Maeda, Y. Tanaka, M. Fukutomi, and T. Asano, Jpn. J. Appl. Phys. Lett. **27**, 209 (1988).

4 Z. Sheng and A. Hermann, Nature **332**, 55 (1988).

5 K. A. Muller, M. Takashige and J. G. Bednorz, Phys. Rev. Lett. **58**, 408 (1987).

6 Y. Yeshurun and A. P. Malozemoff, Phys. Rev. Lett. **60**, 2202 (1988).

7 M. Tuominen, A.M. Goldman, and M.L. Mecartney, Phys. Rev. B **37**, 548 (1988).

8 A. C. Mota, A. Pollini, P. Visani, K. A. Muller and J. G. Bednortz, Phys. Rev. B **36**, 829 (1987).

9 A. C. Mota, A. Pollini, P. Visani, K. A. Muller and J. G. Bednorz, Physica C **153-155**, 67 (1988).

10. P. W. Anderson, Phys. Rev. Lett. **9**, 309 (1962).

11. P. W. Anderson and Y. B. Kim, Rev. Mod. Phys. **36**, 39 (1964).

12 J. Z. Sun, B. Lairson, C. B. Eom, J. Bravman, and T. H. Geballe, Science **247**, 307 (1990).

13 M. P. Maley and J. O. Willis, Phys. Rev. Lett. **42**, 2639 (1990).

14 M. P. A. Fisher, Phys. Rev. Lett. **62**, 1415 (1989).

15 M. V. Feigel'man, V. B. Geshkenbein, A. I. Larkin, and V. M. Vinokur, Phys. Rev. Lett. **63**, 2303 (1989).

16 E. Zeldov, N. M. Amer, G. Koren, A. Gupta, M. W. McElfresh, and R. J. Gambino, Appl. Phys. Lett. **56**, 680 (1990).

17 V. M. Vinokur, M. V. Feigel'man, V. B. Geshkenbein, and A. I. Larkin, Phys. Rev. Lett. **65**, 259 (1990).

18 J. Z. Sun, C. B. Eom, B. Lairson, J. C. Bravman, and T. H. Geballe, Phys. B **43**, 3002 (1991).

19. R. Griessen, Physica C **172**, 441 (1991).

20 M.R. Beasley, R. Labusch and W.W. Webb, Phys. Rev. **181**, 682 (1969).

21. L. Civale, A. D. Marwick, T. K. Worthington, M. A. Kirk, J. R. Thompson, L. Krusin-Elbaum, Y. R. Sun, J. R. Clem, and F. Holtzberg, Phys. Rev. Lett. **67**, 648 (1991).

22 J.R. Thompson, Y.R. Sun, and F. Holtzberg, Phys. Rev. B, **44**, 458 (1991).

23 D. L. Kaiser, F. Holtzberg, M. F. Chisholm, and T. K. Worthington, J. Crystal Growth **85**, 593 (1987).

24 A. Goyal, P. D. Funkenbusch, D. M. Kroeger, and S. J. Burns, Physica C **182**, 203 (1991).

25 K. B. Alexander, A. Goyal, D. M. Kroeger, V. Selvamanicam, and K. Salama, manuscript in preparation.

26 A. Goyal, K. B. Alexander, D. M. Kroeger, P. D. Funkenbusch, and S. J. Burns, manuscript in preparation.

27 Quantum Design Inc., Magnetic Property Measurements System Operating Manual, Quantum Design, San Diego (1989).

28 Young Cheol Kim, "*Anisotropies in the Magnetic Properties of Aligned High-T_c Superconducting $Y_1Ba_2(Cu_{1-x}Fe_x)_3O_z$ Powder Composites*", Ph. D. Thesis, (May 1989).

29 C. P. Bean, Phys. Rev. Lett. **8**, 250 (1962); C. P. Bean, Rev. Mod. Phys. **36**, 31 (1964).

30 J. R. Thompson, Y. R. Sun, L. Civale, A. P. Malozemoff, M. W. McElfresh, A. D. Marwick, and F. Holtzberg Phys. Rev. B (in press, June 1993).

31 A. I. Larkin, Zh. Eksp. Teor. Fiz. **58**, 1466 (1970) [Sov. Phys. JEPT **31**, 784 (1970)].

32 A. I. Larkin and Yu. N. Ovchinnikov, J. Low Temp. Phys. **34**, 409 (1979).

33 K. H. Fischer and T. Nattermann, Phys. Rev. Lett. **43**, 10372 (1991).

34 G. Blatter, M. V. Feigel'man, V. B. Geshkenbein, A. I. Larkin, and V. M. Vinokur, (to be published).

35 H. G. Schnack, R. Griessen, J. G. Lensink, C. J. van der Beek, and P. H. Kes, Physica C, **197**, 337 (1992).

36 See M. Kardar, Nucl. Phys. **B290 [FS20]**, 582 (1987).

37 K. A. Muller, M. Takashige, and J. G. Bednorz, Phys. Rev. Lett. **58**, 1143 (1987).

38 A. C. Mota, A. Pollini, P. Visani, K. A. Muller, and J. G. Bednorz, Phys. Rev. B **36**, 4011 (1987).

39 Y. Yeshurun, A. P. Malozemoff, and F. Holtzberg, J. Appl. Phys. **64**, No. 10, 5797 (1988).

40 E. L. Ventureini *et* al., Appl. Phys. Lett. **56**, 2456 (1990).

41 Shigemi Kohiki, Shin-ichiro Hatta, Kentaro Setsune, Kogotaka Wasa, Yasa, Yasuhiro Higashi, Sei Fukushima, and Yohichi Gohshi, Appl. Phys. Lett. **56**, No. 3, 298 (1990).

42 A. P. Malozemoff and Matthew P. A. Fisher, Phys. Rev. B **42**, 6784 (1900).

43 Y. Xu, M. Suenaga, A. R. Moodenbaugh, and D. O. Welch, Phys. Rev. B **40**, 10882 (1989).

44 A. P. Malozemoff, in Physical Properties of High Temperature Superconductors I, edited by D. M. Ginsberg (World Scientific, Singapore, 1989), P. 71ff.

45 M. V. Feigel'man, V. B. Geshkenbein, and V. M. Vinokur, Phys. Rev. B **43**, 6263 (1991).

46 L. Civale, J. R. Thompson, D. K. Christen, M. McElfresh, unpublished.

47 A. P. Malozemoff, in Superconductivity and its Applications, AIP Conference Proceedings 219, ed. Y. H. Kao et al. (AIP, New York, 1991), p. 84. also A. P. Malozemoff, Physica C **185-189**, 264 (1991).

48 C. W. Hagen and R. Griessen, in Studies of High Temperature Superconductors, Vol. 3, ed. A. V. Narlikar (Nova Science Publishers Inc., Commack NY, 1990), p. 159.

49 C. W. Hagen and R. Griessen, Phys. Rev. Lett. **62**, 2857 (1989).

50 L. Pust, J. Kadlecova, M. Jirsa, and S. Durcok, J. Low Temp. Phys. **78**, 179 (1990).

51 A. Gurevich, H. Kupfer, B. Runtsch, R. Meier-Hirmer, D. Lee, and K. Salama, Phys. Rev. B, **44**, 12090 (1991).

52 B. M. Lairson, J. Z. Sun, J. C. Bravman, and T. H. Geballe, Phys. Rev. B **42**, 1008 (1990).

53 Y. R. Sun, J. R. Thompson, D. K. Christen, F. Holtzberg, and J. G. Ossandon, Physica C **194**, 403 (1992).

54 D.J. Bishop, P.L. Gammel, D.A. Huse, and C.A. Murray, Science, **255**, 165 (1992).

55 L. Gao, Y.Y. Xue, P.H. Tor, and C.W. Chu, Physica C **177**, 438 (1991).

56 D.A. Brawner, N.P. Ong, and Z.Z. Wang, Phys. B. (submitted).

57 B.M. Lairson, J.Z. Sun, T.H. Geballe, M.R. Beasley, and J.C. Bravman, Phys. B, **43**, 10405 (1991).

58 M. P. Maley, J. O. Wills, H. Lessure, and M. E. McHenry, Phys. Rev. B **42**, 2639 (1990).

59 J.Z. Sun, C.B. Eom, B. Lairson, J.C. Bravman and A. Kapitulnik, Physica C **162-164**, 687 (1989).

60 C. Keller, H.Kupfer, R. Meier-Hirmer, U. Wiech, S. Selvamanickam and K. Salama, Cryogenics **30**, 401 (1990) and also Cryogenics **30**, 411 (1990).

61 I. A. Campbell, L. Fruchter, and R. Cabanel, Phys. Rev Lett. **64**, (1990) 1561.

62 M.J. Ferrari, M. Johnson, F.C. Wellstood, and J. Clarke, Phys. Rev. Lett. **64**, 72 (1990).

63 T.M. Palstra, B. Batlogg, L.F. Schneemeyer, and J.V. Waszczak, Phys. Rev. Lett. **61**, 1662 (1988).

64 J. D. Hettinger, A. G. Swanson, W. J. Skocpol, J. S. Brooks, J. M. Graybeal, P. M. Mankiewich, R. E. Howard, B. L. Straughn, and E. G. Burkhardt. Phys. Rev. Lett. **62**, 2044 (1989).

65 P. Chaddah and K. V. Bhagwat, Phys. Rev. B **43**, 6239 (1991).

66 A. Gurevich, Phys. Rev. B **42**, 4857 (1991).

67 J. Bardeen and M. J. Stephen, Phys. Rev. **141** 1197 (1965).

68 A. Gurevich, H. Kupfer and C. Keller, Supercond. Sci. Technol. **4**, S91 (1991).

69 P. H. Kes and J. van den Berg, in Studies of High Temperature Superconductors, edited by A. V. Narlikar (Nova Science, New York), Vol. 5.

70 E.C. Jones, D.K. Christen, C.E. Klabunde, J.R. Thompson, D.P. Norton, R. Feenstra, D.H. Lowndes, and J. D. Budai, Appl. Phys. Lett. **59**, (1991) 24.

71 S. Senoussi, M. Oussena, G. Collin and I.A. Campbell, Phys. Rev. B**37**, 9792 (1988).

72 G. Ravi-Kumar and P. Chaddah, Phys. Rev B **39**, 4704 (1989).

73 L. W. Conner, A. P. Malozemoff, and I. A. Campbell, Phys. B **44**, 403 (1991).

74 M. Daumling and D.C. Larbalestier, Phys. Rev. B **40**, 9350 (1989).

75 S. Zhu., D. K. Christen, C. E. Klabunde, J. R. Thompson, E. Jones, R. Feenstra, D. H. Lowndes, and D. P. Norton, Phys. Rev. B **46** 5576 (1992).

APPENDICES

APPENDIX A

SQUID detector

Presented here is a short discussion of the principle of the SQUID detector for better understanding of the SQUID magnetometer.

The Josephson Junction, which can be formed by two superconducting films separated by a very thin insulating layer, has remarkable transport properties. The current-voltage characteristics for such a weakly coupled junction are shown in Fig. 1.

The junction has no resistance if the applied current is smaller than a certain value, the Josephsen critical current. When the current I reaches the critical current, the voltage V across the junction jumps from zero to 2Δ, where Δ is the energy gap of the superconducting film used in the junction. For still higher current, the junction exhibits a highly non-linear characteristic. The other feature is that this current-voltage characteristic is very hysteretic. As shown in the Fig. 1, when the current reduces to a value smaller than the critical current, the voltage remains at 2Δ until I approaches zero. In some cases, the hysteresis in the I-V curve needs to be suppressed. To do that, one can deposit a paralled resistor across the junction with a value slightly less than the normal-state resistance of the junction. When the voltage is reduced below 2Δ, the shunt

Figure 1

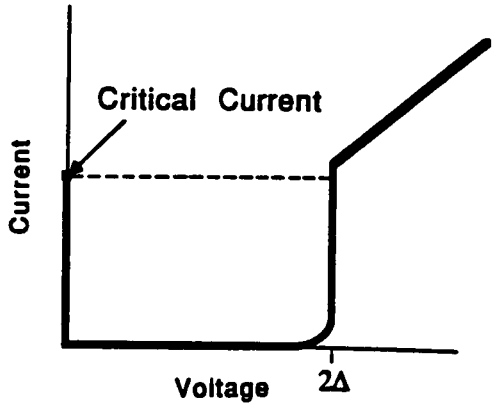

The current-voltage characteristic of a Josephson junction.

makes the current decrease linearly.

The Josephson critical current is extremely sensitive to magnetic field and magnetic flux. When exposed to an applied field, the critical current obeys the following equation:

$$I_c(\Phi) = I_c(0)\left|\frac{\sin(\pi\Phi/\Phi_0)}{\pi\Phi/\Phi_0}\right|$$

where $I_c(0)$ is the zero flux critical current, Φ is the magnetic flux within the junction and Φ_0 is the flux quantum. The modulation in the current is analogous to Fraunhofer pattern in optical diffraction.

This dependence of the critical current on magnetic field allows us to build a highly sensitive magnetometer. Fig. 2 (a) shows schematically a dc SQUID made of two Josephson junctions placed in parallel. The Josephson critical current for this two junction circuit is the following:

$$I_c(\Phi) = I_c(0)\left|\cos(\pi\Phi/\Phi_0)\right|$$

The advantage of this two Josephson junction device is that the area for counting the flux is that of the loop, not that of an individual junction. This greatly increases the sensitivity to the magnetic field.

Another SQUID device, called an RF SQUID, is the one actually used in the Quantum Design magnetometer. The RF SQUID uses only one Josephson junction in

Figure. 2

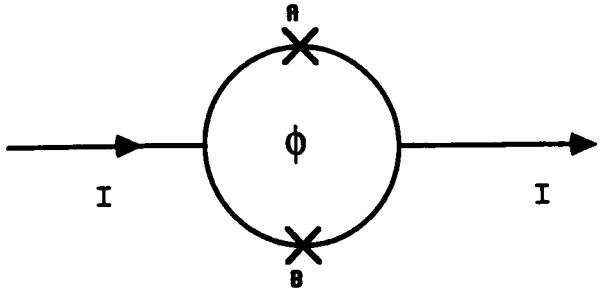

(a)

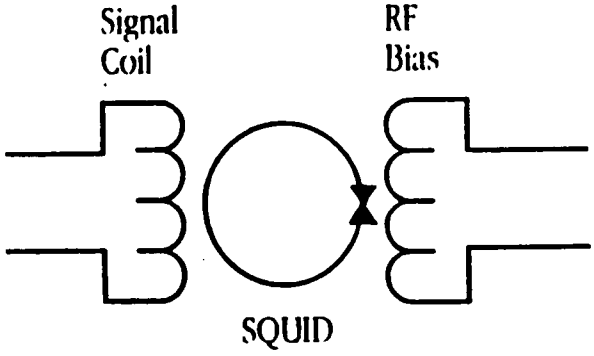

(b)

Schematic of SQUID: (a) a DC SQUID, (b) a RF SQUID.

a loop (Fig. 2 b). The loop is then inductively coupled to an LC circuit with a resonant frequency in the radio frequency range of one megahertz or higher. For the Quantum Design unit, the frequency is 200 MHz. The quality factor of this LC circuit must be at least 100. When the instantaneous current in the inductor increases, a current is induced in the SQUID loop so as to cancel the flux produced by the current in the inductor. If this shielding current reaches the Josephson critical current, the loop can no longer shield the flux and one quantum of the flux enters the loop. The shielding current then decreases by amount of Φ_0/L, where L is the inductance of the SQUID loop. This reduces the shielding current to a value less than the critical current, so that the loop can shield again. By allowing flux to enter one quantum at a time, the loop works like a flux turnstile. The entry of flux into the loop is a dissipative process that diminishes the quality factor of the RF circuit and can be measured. In practice, the SQUID is used as a very sensitive nulling element in a feedback circuit, so that the SQUID remains "locked onto" a fixed number of quanta in the loop. Like the dc SQUID, the appropriate area for the RF SQUID is the area of the loop.

1. B. D. Josephson, Phys. Lett. **1**, 251 (1962).
2. Richard A. Ferrell, in *High Temperature Superconductivity* (Jeffrey W. Lynn, ed.), p. 60, Springer-Verlag, New York, 1990.
3. Vladimir Z. Kresin and Stuart A. Wolf, *Fundamentals of Superconductivity*, p. 155, Plenum Press, New York, 1990.

VITA

Yang Ren Sun was born in Shanghai, China, on November 23, 1948. He received his basic education in Shanghai. In 1966, when he was about to finish his high school education, the Cultural Revolution in China suspended all educational systems in the country. In the following four years he worked at a farm and came back to Shanghai later to teach at a high school until the recovery of the university educational system in 1978. He entered the East China Normal University in February 1978 and received a Bachelor of Science degree in Physics in 1982. In February 1982, he entered the graduate school of Tongji University in China. Two and half years later he was awarded a Master degree in Physics and took the position of Lecturer at the Department of Physics, the East China University of Chemical Technology.

In January of 1989, he came to the United States to resume his graduate study towards a Doctor of Philosophy degree at the University of Tennessee, Knoxville. He received a research assistantship in August 1989 and has performed research on the magnetic properties of high temperature superconductors at the Solid State Division, Oak Ridge National Laboratory since April of 1990. He expects to receive the Doctor of Philosophy degree with a major in Physics in May, 1993.

The author is a member of Sigma Xi Scientific Society and a member of the American Physical Society, with membership in the Division of Condensed Matter Physics. In 1992, the faculty designated him "Outstanding Graduate Student in Physics" at the University of Tennessee. In 1993 he received "The first place award in the

graduate student paper competition" sponsored by the Sigma Xi Chapter of the University of Tennessee.